AN ABSTRACT OF THE THESIS OF

Jie Zhao for the degree of Doctor of Philosophy in Physics
presented on May 18, 1994.

Title: Measurement of Spin Observables for Proton-Deuteron Elastic Scattering

Abstract approved: ___

Albert W. Stetz

The spin transfer coefficients D_{NN}, D_{SS}, D_{LL}, D_{SL}, D_{LS}, the analyzing power A_N, and the induced polarization P_N for proton-deuteron elastic scattering have been measured at TRIUMF, using the 290 and 400 MeV polarized proton beams and a solid CD_2 target. This work represents the first measurement of the p-d spin observables in this proton energy region. The results of the measurement are consistent with time-reversal invariance within the experimental uncertainties. The comparison of the experimental data with the results of a multiple scattering based calculation limited to single and double scatterings using T.-S. H. Lee's Nucleon-Nucleon interaction model with the A and C Wolfenstein coefficients has revealed a generally better agreement between the spin observable data and the calculation results with the input of off-shell N-N amplitude and both the singe and double scattering terms. Calculations with higher order multiple scattering terms and more spin dependent forces are desired for further investigation with the data.

Measurement of Spin Observables for Proton-Deuteron Elastic Scattering

by

Jie Zhao

A Thesis submitted to

Oregon State University

in partial fulfillment of the

requirements for the degree of

Doctor of Philosophy

Completed May 18, 1994

Commencement June 1995

APPROVED:

Redacted for Privacy

Professor of Physics in charge of major

Redacted for Privacy

Head of Department of Physics

Redacted for Privacy

Dean of Graduate School

Date thesis presented May 18, 1994

Typed by Jie Zhao for Jie Zhao

For her grace,

love,

encouragement,

and support in everyday of the past years ....

— this thesis is dedicated to my wife, Qing.

ACKNOWLEDGEMENTS

The rewarding period of my graduate study and the success of this thesis project have been the result of the invaluable support from many people, to whom I wish to express my sincere gratitude.

I am particularly thankful to my thesis advisor, Dr. Albert W. Stetz, for providing the opportunity and guidance for my graduate study, without which the success of this thesis program would have not been possible. His advise and support have been most helpful and are highly appreciated.

I wish to express my sincere gratitude to Dr. Rudy Abegg and Dr. Dave Hutcheon at TRIUMF for the opportunity working on this project, whose experience and insights have been invaluable to the completion of this work. Their critical comments on this thesis are greatly appreciated. I am sincerely thankful to Dr. Bradly Keister at Carnegie Mellon University for his generous and timely contribution in providing the calculation necessary for the completion of this thesis.

I owe many thanks to Dr. Andy Miller and Dr. Stanley Yen at TRIUMF not only for the opportunities to be part of a number of challenging projects, which has become an important part of my graduate training experience but also for their friendliest and always dependable support.

My deep gratitude is due to Dr. George Chang at University of Maryland whose encouragement, firm help and friendship have been most precious.

I sincerely thank Dr. Victor A. Madsen, Dr. Wayne L. Swenson, Dr. Clifford E. Fairchild, Dr. William Hetherington, Dr. Carl A. Kocher, and Dr. John R. Arthur for being my committee and for the careful comments on this thesis. I am also grateful to Dr. Dave Mack at CEBAF, Dr. Pat Walden at TRIUMF and

Dr. Pat Welch for their friendly help. Dr. Rubin H. Landau's generous effort in making available to me his LaTeX environment is highly appreciated. I sincerely thank Ms. Wanda M. Moeller, Ms. Laurel K. Busse, Ms. Verna Paullin-Babcock and Mr. Keith Goodman for their friendly help.

My deepest thank and appreciation are due to my wife and our parents to whom I have been deeply indebted, for their unconditional love, encouragement, understanding and patience.

Table of Contents

List of Figures

List of Tables

Measurement of Spin Observables for Proton-Deuteron Elastic Scattering

Chapter 1

Introduction

One of the most fundamental problems of nuclear physics is the investigation of the nature of the nucleon-nucleon (N-N) interaction. Proton-deuteron (p-d) elastic scattering, as the simplest few body system, is expected to provide useful information in the aspects of spin dependence and off-(energy)-shell components of the N-N interaction. Compared with two nucleon systems, the p-d system has the following characteristics:

- In three body systems, the spin dependent forces are strong and manifest themselves mainly through spin observables. As a consequence the three body system is highly sensitive to spin effects (at least an order of magnitude higher than two nucleon systems). This suggests that p-d elastic scattering is sensitive to many aspects of the spin structure of the three-body processes. Some of the amplitudes are found to be very sensitive to these processes while others have little or no sensitivity.

- The interaction between any two nucleons is off-shell due to the presence of the third nucleon. The on-(energy)-shell part of the N-N scattering amplitude, which can be determined from N-N scattering, is no longer sufficient for the description of proton-nucleus scattering. The p-d elastic scattering provides opportunity for studying off-shell behavior of the N-N interaction, which is not possible with two nucleon systems.

- Easier and more detailed theoretical analysis of the problem than that of the heavier nucleus is possible due to the comparably simpler deuteron structure.

The increasing availability of polarized proton and deuteron beams, targets and the development of polarization measurement facilities at a number of experimental laboratories make it possible to measure a large number of spin observables. The reactions with polarized beams, targets and the analysis of the polarization of the final reaction products offer much more detailed information on the dynamical properties of the system under study in terms of spin observables. For a reaction $a + b \rightarrow c + d$, the initial and final states can be characterized by the spins s_a, s_b and s_c, s_d of the participating particles and their projections m_a, m_b and m_c, m_d on some arbitrary axis. The T-matrix of this reaction may be labeled by these projections $T_{m_a m_b m_c m_d}$. The number of independent matrix elements is $N = (2s_a + 1)(2s_b + 1)(2s_c + 1)(2s_d + 1)/2$ if parity is conserved. For massless particles the spin multiplicity is just 2.

Since the matrix elements are complex quantities, one has in principle to measure $2N - 1$ real observables for a complete determination of all matrix elements because one phase remains free. The unpolarized differential cross section is the sum of the squared absolute values of the T-matrix elements

$$\frac{d\sigma_0}{d\Omega} = \sum_{m_a m_b m_c m_d} |T_{m_a m_b m_c m_d}|^2 \tag{1.1}$$

Thus small amplitudes may be completely buried by the big ones. On the other hand, the general structure of a polarization observables is given by a bilinear Hermitian form

$$\begin{aligned} C(a^{(i)}, a^{(f)}) &= Tr(Ta^{(i)}T^{\dagger}a^{(f)}) \\ &= \sum_{\mathbf{all}m,m',n,n'} T_{m'_c m'_d m_a m_b} a^{i}_{m_a m_b n_a n_b} T^{*}_{n'_c n'_d n_a n_b} a^{f}_{n'_c n'_d m'_c m'_d} \end{aligned} \tag{1.2}$$

with appropriate initial and final state spin operators $a^{(i)}$ and $a^{(f)}$, respectively. Since a spin-s constitutes $(2s+1)^2$ independent spin operators, one obtains a large number of linearly independent observables. These observables contain interference terms of the T-matrix elements in different combinations. Therefore, they can be more sensitive to small amplitudes and/or to small contributions of interesting dynamical effects which may be amplified this way. This is the reason for the increased interest in polarization observables.

Previous measurements of p-d elastic scattering spin observables in various energy regions have indicated some connections between certain observables and several dynamical aspects [1] [2] [3] [4], such as: (i), the deuteron vector analyzing power seems sensitive to the p-wave N-N interaction; (ii), the tensor analyzing power has a dominant contribution from the tensor force; (iii), information on the Coulomb interaction could be obtained by studying the proton analyzing power; (iv), the spin rotation parameters provide an additional test for non-eikonal multiple scattering theories apart from the deuteron asymmetries which detect any deviations from the eikonal approximation; (v), spin correlation parameters have helped in the understanding of off-shell effects.

Compared with other reactions for off-shell behavior study, such as N-N bremsstrahlung, the p-d elastic system has a much larger cross section and most importantly a much higher off-shell component (as shown in Table 1), which makes p-d interaction an excellent choice to investigate off-shell dependence of N-N interac-

Table 1. Comparison of p-d elastic scattering with N-N bremsstrahlung

Reaction	Cross-section	Off-shell component
p-d elastic [5]	$\sim$ mb	$\sim$ 10%
N-N bremsstrahlung [6]	$\sim \mu$b	$< 0.1\%$

tion from the experiment point of view.

The extraction of N-N amplitudes from the scattering observables has been one of the basic motivations for a number of experiments. Because of the spin $\frac{1}{2}$ - 1 structure of the p-d scattering there are 12 independent complex amplitudes that govern the reaction for a given incident energy and momentum transfer. To reconstruct the collision matrix to within an arbitrary phase term, it is necessary to measure a minimum set of 23 independent spin observables.

For proton-nucleus elastic scattering a light nucleus like the deuteron clearly possesses advantages. For heavier nuclei, it is exceedingly difficult to isolate elastic scattering at intermediate and high incident energies due to the low first excited state energies (at most a few MeV); while for the deuteron it can be easily realized by detecting the recoiling deuteron. Furthermore, the sensitivity to such effects like nucleon-nucleon correlation, Δ intermediate states or non-eikonal propagation are enhanced for light nuclear targets.

In the low incident proton energy region ($T_p < 50$ MeV) the experimental data are usually explained by solving Faddeév equations [7] for the scattering amplitudes. However, at higher energies, in particular above 200 MeV, this method becomes impractical due to the large number of partial waves. The theoretical cal-

culations at high energies therefore depend on the multiple-scattering approaches. Glauber multiple scattering theory [8] [9] [10] has been proven to be a good first order approximation. The theory assumes high incident particle energy and geometrical optical propagation of the projectile wave between its consecutive scatterings from the target nucleons (i.e. the eikonal approximation) and describes the proton-deuteron scattering amplitudes as a sum of two terms, single and double scatterings, whose ingredients depend solely on the deuteron wave function and the on-shell nucleon-nucleon scattering matrix elements. The Glauber theory has been successful in explaining a great deal of the experimental data on high-energy small-momentum-transfer scattering processes. For example, it is successful in explaining the prominent features such as (i), the steeply peaked forward p-d elastic scattering cross section and its flatter part in the large momentum transfer regions using the concept of single and double scatterings between the projectile nucleon and those in deuteron nucleus; (ii), the D-state (spin flip) effects in filling up the break up region in the cross section where single and double scattering interfere destructively.

There have been many corrections examined to the Glauber theory [11] [12] [13] [14] [15] [16] [17]. Among them are the effects of off-shell N-N scatterings, higher order multiple scattering, the relativistic effects, spin dependent, and non-eikonal propagation between the successive scatterings from the nucleons. Generally, the different effects of the corrections have been discussed separately, and they have only been estimated when combined.

Another approach based on multiple scattering, is the so called "Light-Front Hamiltonian Dynamics" calculation which treats N-N interaction within the framework of relativistic Hamiltonian particle dynamics implemented with light-front Poincaré generators [18]. In this approach, the Hamiltonian describes the interac-

tion of a fixed number (in this case, three) of nucleons. The small number of degrees of freedom eliminates the need for perturbative expansion involving strong interactions. One of the evident advantages of this approach, compared with Glauber theory, is it allows the freedom of off-shell description of N-N interactions.

The calculation used to compare the data of this experiment is based upon multiple scattering expansion of the Faddeév equations, using relativistic kinematics and non-relativistic dynamics (See Section 6.3). In principle, the multiple-scattering approaches work well at high incident proton energy ($\sim$ GeV). At lower energies, particularly below 500 MeV, the convergence of the multiple expansion of the N-N t matrix series becomes slower. However, it is interesting to study the performance of the multiple scattering approaches in the energy range from 200 to 500 MeV.

In the past two decades data at proton energy >1 GeV have been accumulated, and recently excellent data sets [19] have become available at 500 and 800 MeV. At the low energy region, extensive data sets exist in the energy region <50 MeV. However few investigations of the intermediate energy region between 200 and 500 MeV can be found, where the Δ plays a dominant role.

The TRIUMF experiment E482, "Measurement of spin observables for proton-deuteron elastic scattering at 290 and 400 MeV" was proposed to measure the five spin transfer coefficients (D_{SL}, D_{LS}, D_{LL}, D_{SS} and D_{NN}), analyzing power (A_N) and induced polarization (P_N) with polarized proton beams of incident energy 290 and 400 MeV. The proton scattering angles range from 20 to 80° in the lab system, which corresponds to the momentum transfer squared (-t) ranging from 0.07 to 0.96 $(\mathrm{GeV/c})^2$.

The experiment was performed on beam line 4B at TRIUMF. The scattered protons were detected by the Medium Resolution Spectrometer (MRS), their polar-

ization was measured with a focal plane polarimeter (FPP) mounted down stream of the MRS focal plane. The recoiling deuterons were detected with a scintillator detector located near the target and inside (or outside in some cases) of the target chamber to eliminate as much as possible the carbon background.

Chapter 2

Nucleon-Nucleus Scattering

Because of the difficulties in solving Faddeév equations for exact solution at incident proton energies >100 MeV for p-d elastic scattering system, the theoretical efforts based on multiple-scattering approaches have been employed for the explanation of the experiment data with intermediate and high incident proton energies. This Chapter outlines two different multiple scattering approaches in dealing with p-d elastic scattering. They are the Glauber model and the approach with Faddeév equations with which we compare our data. The first section introduces the "bare" nucleon-nucleon (NN) force and Lee's NN interaction model which is the input for theoretical calculations. In the second section the formal scattering theory is recalled. The Faddeév equations for the scattering T-matrix and the Glauber multiple scattering model are described in the final two sections.

2.1 Nucleon-Nucleon interaction

One of the most fundamental problems in Nuclear Physics is to investigate the nature of nucleon-nucleon interaction. Calculations of different types for the interaction of nucleon-nucleus, nucleus-nucleus are all based on the basic interaction

between nucleons. which can be sensitive to spin dependent forces and off-shell effects.

2.1.1 The Nucleon-Nucleon Force

The first thing that must be done if one wishes to obtain a reasonable description of the NN potential is to determine the most general operator structure that it may have. This, of course, will answer the question, "What other types of possible forces are there besides the well known central, spin-orbit, and spin-spin forces?".

A completely general and commonly used form for the space-spin part of the non-relativistic NN potential built from invariance principles with the conservation of parity, momentum, angular momentum, and rotational invariance constraints is

$$V = V_c + V_{ss}(\vec{\sigma_1} \cdot \vec{\sigma_2}) + V_{LS}(\vec{L} \cdot \vec{S}) + V_T S_{12}(\vec{r}) + V_{LS^2}(\vec{L} \cdot \vec{S})^2. \tag{2.1}$$

However this is not a unique expression. It is truncated to the following form in all the models that will be discussed,

$$V = V_c + V_{ss}(\vec{\sigma_1} \cdot \vec{\sigma_2}) + V_{LS}(\vec{L} \cdot \vec{S}) + V_T S_{12}(\vec{r}) \tag{2.2}$$

where the tensor operator S_{12} is defined as

$$S_{12}(\vec{r}) = \frac{3(\vec{\sigma_1} \cdot \vec{r})(\vec{\sigma_2} \cdot \vec{r})}{r^2} - \vec{\sigma_1} \cdot \vec{\sigma_2} \tag{2.3}$$

and each of V_C, V_{LS} and V_T are complex amplitudes. So in general, the NN force contains a central piece, a spin-spin piece, a spin-orbit piece and a tensor piece. If we further consider conservation of isospin and spin we can write the total potential as

$$V^{tot} = V + V^{\tau} \tau_1 \cdot \tau_2 \tag{2.4}$$

where V^{τ} simply implies that the amplitudes for the isovector channel can be different than those for the isoscalar channel V. A common approach is to parameterize

each of the amplitudes in terms of Yukawa functions. This is done to provide a convenient calculational form for the interaction and to embody the idea of meson exchanges.

The meson exchange theory of nuclear forces began when Yukawa (1935) showed that the exchange of a single pion reproduces the long range part of the force extremely well. For a long while after this (in the 1950's) theorists struggled in an attempt to derive the nuclear force from a field theoretical approach but were thwarted by the inability to evaluate two-pion exchange (TPE) contributions to the potential. The discovery of heavier mesons ended this pursuit and spawned the One Boson Exchange (OBE) model of the NN force. The OBE potential arose because the exchange of a single boson is easily calculated and it seemed that there were, at least qualitatively, enough mesons existing below the nucleon mass to describe all parts of the force at the proper ranges. The pion, for instance, is a pseudoscaler meson and provides the long range attraction and most of the tensor force. Table 2 contains a summary of the character of each of the mesons [20] which form a minimal complement of mesons for a OBE potential. This is intended to illustrate the role played by the various types of mesons in transmitting the nuclear force in relation to how they couple to the nucleon. In typical models the η, and δ (M_η = 549 MeV and M_δ = 983 MeV) mesons are sometimes included in this list but they couple only weakly and are not as important. The most important features are as follows,

- The pion provides most of the long range tensor force which is cut off at short ranges by a strong short range component of opposite sign coming from the ρ.

- All mesons save the pion contribute coherently to the strongly attractive spin-orbital potential.

Table 2. Summary of the Primary Meson Contributions to the NN Force

Coupling	Bosons (Strength of coupling)		Characteristics of Force			
	T=0 (1)	T=1 ($\tau_1 \cdot \tau_2$)	Central (1)	Spin-Spin ($\sigma_1 \cdot \sigma_2$)	Tensor (S_{12})	Spin-Orbit (L·S)
Pseudo-scalar	–	π (strong)	–	weak coherent with v,t	strong	–
scalar	σ (strong)	–	strong attract.	–	–	coherent with v
vector	ω (strong)	ρ (weak)	strong repuls.	weak coherent with ps	opposite to ps	strong coherent with s
tensor	ω (weak)	ρ (strong)	–	weak coherent with ps	opposite	–

- The hypothetical σ exchange provides the majority of the intermediate range attraction with a small amount added by the ρ exchange.

The particle referred to as the σ in the table does not actually exist. One may argue however that this simple approximation of two pion exchange (TPE) should be reasonable because two pions in a relative s-wave interact strongly. The mass and coupling constant of the σ particle are usually left as free parameters in fits of NN data. In any case, more advanced meson exchange models actually treat two pion exchange as such. There are presently two methods by which this is done: (1), with Dispersion theory (the Paris potential) and (2), via field theory (the Bonn potential). The two approaches are discussed in the next two sections.

The Paris Potential

One may expand the NN potential in the following way,

$$V = V_\pi + V_{2\pi} + V_{3\pi} + \cdots \tag{2.5}$$

Since the ω meson is a 3π resonance and the short range part of the force is not well known, it would seem reasonable to truncate this expansion in the following way,

$$V = V_\pi + V_{2\pi} + V_\omega. \tag{2.6}$$

This is the approach taken by the Paris group in constructing a NN potential. As mentioned before the one boson exchange terms $(1\pi, 1\omega)$ are relatively easy to calculate, but the two pion exchange terms are difficult. To aid in this, the Paris group employed dispersion theory to generate an NN scattering amplitude from which a potential was subsequently derived. Dispersion theory is used in the calculation of the 2π contribution [20]. Empirical $\pi\pi$ and πN scattering information is used as input and dispersion relations are subsequently used to generate the assumption of some form for the potential. As with all NN potentials, theoretically based or otherwise, there is a phenomenological repulsive core included. This is typically represented by a constant soft core which is cut off at around r $\sim$ 0.8 fm.

The Bonn Potential

A field theoretical potential developed by the Bonn group [20][21] marks the culmination of almost a decade of work and is the most complete attempt to describe the NN potential within a meson field theoretical framework. The Bonn potential includes multiple pion exchanges up to the 4π level and also accounts for meson-nucleon resonances. All of the relevant diagrams for 2π, 3π exchanges, etc. are evaluated analytically; There are about a dozen adjustable parameters in the

model which are fit to data. These are all either coupling constants or form factors and hence have physical meaning. All other parameters are either theoretically predicted or are taken from experiment.

2.1.2 Off-shell Aspects

In the case of elastic two-nucleon scattering, the total energy of the two nucleons in the initial and final states of the reaction is the same, which is the case of "On-(energy)-shell". On the other hand, in the case, for instance, bremsstrahlung and many-body problem, the nucleons in virtual intermediate states violate energy conservation, and the nucleon-nucleon interaction is referred to as "Off-(energy)-shell".

A knowledge of the off-shell behavior of the nucleon-nucleon interaction is basic to nuclear physics. The on-shell information, however complete, is not adequate to permit unambiguous calculations of the properties of systems of more than two nucleons. Any reasonable agreement with nuclear binding energy and other properties obtained by using different potential models without knowing the correct off-shell behavior of the interaction is probably fortuitous and therefore not very meaningful. Even if the fits to data on the two-body problem (on-shell data) were identical, the different models can still disagree when compared in many-body calculations.

Because of the differences in the derivation of models for the nuclear force, there are indeed different off-shell effects. Dispersion relations yield a scattering amplitude on-shell, however, by defining a potential some kind of off-shell prescription enters the derivation silently. The Paris potential is parameterized in terms of static Yukawa functions which define the potential on- and off-shell. In the field-theoretical approach, the set of irreducible diagrams defining a quasipotential is

given a priori on- and off-shell. Therefore differences in the calculations with different origins of the off-shell potentials indicate the degree of off-shell dependence of a reaction.

2.1.3 Lee's NN interaction model

Lee's NN interaction model [22][23][24] is based on the assumptions of (i), the NN force at the long and intermediate ranges (roughly $r \geq 1$ fm) can be described by the exchange of mesons, and (ii), the short range part can be treated phenomenologically by fitting the NN data, it follows the unitary formulation and uses a meson theory of nuclear force which is closely related to the Paris potential, and describes NN scattering up to 2 GeV.

The model describes NN scattering by constructing a many-body one meson exchange Hamiltonian for π, N, Δ and N*. It consists of a πN$\leftrightarrow$ Δ or N* vertex interactions and baryon-baryon transition interactions from NN to NΔ, $\Delta\Delta$, NN* and N*N*. The πN$\leftrightarrow$ Δ and N* excitation effect on NN scattering is treated in a dynamical three-body approach with a simple isobar model; the NN$\rightarrow$NN interaction is directly derived from the Paris potential by using a momentum-dependent procedure to subtract the contribution from intermediate states involving Δ or N*; and the transition interactions NN$\leftrightarrow$NΔ, $\Delta\Delta$, NN* and N*N* are determined by one-pion and one-rho exchange.

2.2 Formal Scattering

2.2.1 Description of Scattering Processes

The ideal picture of a scattering process can be described as a plane wave $\phi_k(\vec{r})$ ($\sim e^{ikz}$) representing the incident particle beam continuously passing a target scatterer. Some of the incident wave is then scattered and becomes the secondary wave $\psi_{ksc}(\vec{r})$. The wave function for the scattering system is then the sum of the primary plane wave and the scattered secondary wave [25],

$$\psi_k(\vec{r}) = \phi_k(\vec{r}) + \psi_{ksc}(\vec{r}). \tag{2.7}$$

Assuming the scattered wave radiates as an outgoing spherical wave asymptotically with a strength factor, or scattering amplitude $f_k(\theta, \phi)$,

$$\psi_{ksc}(\vec{r}) \sim \frac{e^{ikr}}{r} f_k(\theta, \phi), \tag{2.8}$$

then the full wave function has the asymptotic form

$$\psi_k(\vec{r}) \sim \frac{1}{(2\pi)^{\frac{3}{2}}}[e^{ikz} + \frac{e^{ikr}}{r} f_k(\theta, \phi)], \tag{2.9}$$

which satisfies the three dimensional Schrödinger wave equation

$$[-\frac{\hbar^2\nabla^2}{2\mu} + V(\vec{r})]\psi(\vec{r}) = E\psi(\vec{r}). \tag{2.10}$$

Using the definition of the differential cross section

$$\frac{d\sigma}{d\Omega} = \frac{N/\Delta t/\Delta\Omega}{Flux_{inc}} = \frac{j_{scatt}\Delta A}{j_{inc}(\Delta A/r^2)}, \tag{2.11}$$

where N is the number of particles scattered into solid angle $\Delta\Omega$ ($=\Delta A/r^2$) in the time interval Δt; j_{inc} and j_{scatt} are the incident and scattered particle current density, respectively. It is straightforward to show that the differential cross section of the scattering process is related to the scattering amplitude by

$$\frac{d\sigma}{d\Omega} = \frac{v_{out}}{v_{in}}|f_k(\theta, \phi)|^2, \tag{2.12}$$

provided that particle velocity $v = \frac{p}{m} = \frac{\hbar k}{m}$.

Introducing the Green's function $G_E^{(+)}(\vec{r}, \vec{r}')$ (+ for outgoing wave) which is the solution of the Schrödinger equation with a point source,

$$[\frac{\hbar^2 \nabla^2}{2\mu} + E]\psi(\vec{r}) = \delta(\vec{r} - \vec{r}'). \tag{2.13}$$

It is straightforward to work out the general solution of the Schrödinger equation 2.10 with potential $V(\vec{r})$:

$$\psi_k^{(+)}(\vec{r}) = \phi(\vec{r}) + \int d^3r' G_E^{(+)}(\vec{r}, \vec{r}') V(\vec{r}') \psi_k^{(+)}(\vec{r}'). \tag{2.14}$$

With the outgoing wave boundary conditions, the Green's function has the form

$$G_E^{(+)}(\vec{r}, \vec{r}') = -\frac{\mu}{2\pi\hbar^2} \frac{e^{ik|\vec{r} - \vec{r}'|}}{|\vec{r} - \vec{r}'|}. \tag{2.15}$$

Asymptotically, $|\vec{r} - \vec{r}'| \xrightarrow{r \gg r'} r - \frac{\vec{r} \cdot \vec{r}'}{r}$ and $G_E^{(+)}(\vec{r}, \vec{r}') \xrightarrow{r \gg r'} -\frac{\mu}{2\pi\hbar^2} \frac{e^{ikr} e^{-i\vec{k} \cdot \vec{r}'}}{r}$. Together with the asymptotic form of the full wave function 2.9 and the solution of Schrödinger equation 2.14, the scattering amplitude can be expressed in terms of interaction potential,

$$f(\vec{k} \to \vec{k}') = -\frac{4\pi^2 \mu}{\hbar^2} \langle \phi_{k'} | V | \psi_k^{(+)} \rangle. \tag{2.16}$$

Introducing the definition of the T matrix,

$$T_{k_0}(\vec{k}, \vec{k}') \equiv \langle \phi_{k'} | T | \phi_k \rangle = \langle \phi_{k'} | V | \psi_k^{(+)} \rangle = \int d^3r' \frac{e^{i\vec{k}' \cdot \vec{r}'}}{(2\pi)^{3/2}} V(\vec{r}') \psi_k^{(+)}(\vec{r}'), \tag{2.17}$$

where k' is arbitrary. When $k' = k$, from equation 2.16, the T matrix is related to the scattering amplitude by

$$f_k(\theta, \phi) = -\frac{4\pi^2 \mu}{\hbar^2} T_{k_0}(\vec{k}, \vec{k}')|_{k'=k}. \tag{2.18}$$

It can be shown, with the scattering wave function 2.14, the equation that the T matrix operator has to satisfy is

$$T_{k_0}(\vec{k}', \vec{k}) = V(\vec{k}', \vec{k}) + \int d^3p V(\vec{k}', \vec{p}) G_{k^0}^{(+)}(p) T_{k_0}(\vec{p}, \vec{k}), \tag{2.19}$$

which is also called the Lippmann-Schwinger equation, where $G_k^{(+)}$ is the Green's function in its momentum space representation,

$$G_k^{(+)}(p) = \frac{1}{E - E(p) + i\epsilon}. \tag{2.20}$$

Even though the physical scattering amplitude is related to the T matrix element only if the kinetic energy is conserved during the scattering process, i.e. $k' = k = E$ which is the condition of on-the-energy-shell, this equation can be used to determine T_{k_0} for all values of $\vec{k}$ and $\vec{k}'$, independent of each other and of E, in which case the kinetic energy is not conserved, i.e. the off-energy-shell scattering. The knowledge of $T_k(\vec{p}, \vec{k})$ for all values of $\vec{p}$ permits the immediate calculation of the wave function $\psi_k^{(+)}(\vec{r})$ for all values of $\vec{r}$, while knowledge at the on-shell point $T_k(\vec{k}, \vec{k})$ determines the scattering amplitude and thus the asymptotic wave function only.

2.2.2 Multiple Scattering by Bound Particle Systems

We consider an incident particle of rest mass m and spin S_i to interact with a scatterer of N bound particles of respective masses $M_1, \ldots, M_N$ and spins $s_1, \ldots, s_N$. The total mass and spin of the scatterer are M_t and S_t. The Hamiltonian for the scattering system is of the form [26]

$$h \equiv \sum_{\alpha=1}^{N} K_\alpha + U, \tag{2.21}$$

where K_α is the kinetic energy operator for particle α, and U is the interaction energy of the N scattering particles. Suppose the scatterers have nonrelativistic

energies, so

$$K_a = -\frac{1}{2M_a}\nabla_{z_a}{}^2. \tag{2.22}$$

The initial state eigenfunction for the scatterer, moving with a momentum $\mathbf{P}$ and having a spin orientation ν_t is

$$\chi_{t;0(\nu_t),\mathbf{P}} = (2\pi)^{-3/2} e^{i\mathbf{P}\cdot\mathbf{C}} g_0(\mathbf{z}_1, s_1, \ldots, \mathbf{z}_N, s_N), \tag{2.23}$$

where $\mathbf{C}$ is the coordinate of the center of mass of the scatterer, g_0 is the initial wave function describing the internal state of the scatterer, and $g_\gamma^\pm$ is a general state of the scatterer. An arbitrary state of scatterer, corresponding to internal state γ, momentum $\mathbf{Q}$ and spin orientation ν_t' is

$$\chi^\pm_{t;\gamma(\nu_t'),\mathbf{Q}} = (2\pi)^{-3/2} e^{i\mathbf{P}\cdot\mathbf{C}} g_\gamma(\mathbf{z}_1, s_1, \ldots, \mathbf{z}_N, s_N), \tag{2.24}$$

and the wave functions 2.23 and 2.24 satisfy the equations

$$h\chi_{t;0(\nu_t),\mathbf{P}} = W_0 \chi_{t;0(\nu_t),\mathbf{P}} \tag{2.25}$$

$$h\chi^\pm_{t;\gamma(\nu_t'),\mathbf{Q}} = W_\gamma \chi^\pm_{t;\gamma(\nu_t'),\mathbf{Q}}, \tag{2.26}$$

where $W_0 = w_0 + P^2/2M_t$ and $W_\gamma = w_\gamma + Q^2/2M_t$. The quantities w_0 and w_γ represent the internal energies of the composite system.

The initial state prior to the scattering, χ_a and possible final states $\chi_b^\pm$ are

$$\chi_a = \chi_{i;p,\nu}\chi_{t;0(\nu_t),\mathbf{P}} \tag{2.27}$$

$$\chi_b^\pm = \chi_{i;k,\nu'}\chi^\pm_{t;\gamma(\nu_t'),\mathbf{Q}}. \tag{2.28}$$

which satisfy the respective equations

$$K\chi_a = E_a\chi_a = (\epsilon_p + W_0)\chi_a \tag{2.29}$$

$$K\chi_b^\pm = E_a\chi_b^\pm = (\epsilon_k + W_\gamma)\chi_b^\pm, \tag{2.30}$$

where

$$K = K_i + h. \tag{2.31}$$

The Hamiltonian for the interacting system is

$$H = K + V, \tag{2.32}$$

where

$$V = \sum_{\alpha=1}^{N} V_\alpha \tag{2.33}$$

is the interacting potential. Here V_α represents the interaction between the incident particle i and the target particle α. Then the Schrödinger wave function describing the entire event is obtained from the Lippmann-Schwinger Equation as

$$\psi_\alpha^+ = \chi_\alpha + \frac{1}{d} V \psi_\alpha^+, \tag{2.34}$$

where

$$d \equiv E_\alpha + i\eta - K. \tag{2.35}$$

We next define a scattering matrix t_α for scattering i on a bound particle α,

$$t_\alpha = V_\alpha + V_\alpha \frac{1}{E_\alpha + i\eta - K - V_\alpha} V_\alpha. \tag{2.36}$$

We now assert that a formally exact solution of equation 2.34 is provided by the set of coupled equations

$$\psi_\alpha^+ = \chi_\alpha + \sum_{\alpha=1}^{N} \frac{1}{d} t_\alpha \psi_\alpha \tag{2.37}$$

$$\psi_\alpha = \chi_\alpha + \sum_{\beta(\neq\alpha)=1}^{N} \frac{1}{d} t_\beta \psi_\beta. \tag{2.38}$$

The exact scattered wave

$$\psi_{sc} = \sum_{\alpha=1}^{N} \frac{1}{d} t_\alpha \psi_\alpha \tag{2.39}$$

is the sum of waves scattered from all N scatterers. The wave incident on scatterer α is now not χ_α but an "effective wave" ψ_α. The effective wave ψ_α is the sum of the incident wave χ_α plus the waves scattered from all scatterers other than α.

The structure of equation 2.37 is seen more easily if we generate a multiple scattering series by successively substituting into the right-hand side of the equations,

$$\psi_\alpha = \chi_\alpha + \sum_{\beta(\neq\alpha)=1}^{N} \frac{1}{d} t_\beta \chi_\alpha + \sum_{\beta(\neq\alpha)=1}^{N} \frac{1}{d} t_\beta \frac{1}{d} \sum_{\lambda(\neq\beta)=1}^{N} t_\lambda \chi_\alpha + \cdots . \tag{2.40}$$

It is evident that the incident particle undergoes a sequence of scattering from one target particle to another, making any number of such scattering before emerging from the target.

The multiple scattering wave function 2.40, while appealing to the intuition, are, of course, difficult to solve in general. Most applications have consequently been made in the weak binding limit where all target particle energies are small compared to the projectile energy, in which case they simplify considerably.

2.3 Faddeév Equations

For a equal mass three-body system, its scattering amplitudes are solutions of Faddeév equations [27][28]:

$$T(W) = T^1(W) + T^2(W) + T^3(W) \tag{2.41}$$

where

$$T^1(W) = \tilde{t}_{23}(E23) + \tilde{t}_{23}(E23) \frac{1}{W - M^{(0)} + i0} [T^2(W) + T^3(W)], \tag{2.42}$$

plus cyclic permutations, and $\tilde{t}_{ij}(E_{ij})$ is the interaction t matrix between particle i and j $(i,j=1,2,3)$, and satisfies the Lippmann-Schwinger equation:

$$\tilde{t}_{ij}(E_{ij}) = \tilde{V}_{ij} + \tilde{V}_{ij}\frac{1}{E_{ij} - H_{ij}^{(0)} + i0}\tilde{t}_{ij}(E_{ij}). \tag{2.43}$$

The solutions of Fadeév equations are exact. However, large load of calculation is usually involved, especially when using phenomenological nuclear forces and relatively high nucleon energies (> 100 MeV).

2.4 Glauber Multiple Scattering Model

There are two basic assumptions of the nuclear diffraction theory:

- The momentum $\hbar k$ of the incident particle is high enough so that the wavelength k^{-1} is much smaller than R, the range of the interaction between the particle and the nucleon, i.e. $kR \gg 1$.
- The target nucleon stands still during collision due to the high velocity of the incident proton. The forward angular distribution of the scattering implies that the partial waves corresponding to a great many values of the orbital angular momentum contribution is coherent to the scattering.

Define the profile function for the collision [9],

$$\Gamma(\vec{b}) \equiv 1 - e^{i2\delta_l} = 1 - e^{\chi(\vec{b})}, \tag{2.44}$$

where δ_l is the complex phase shift parameter, $\vec{b}$ is the impact vector of the incident particle in the plane perpendicular to $\vec{k}$, and $\chi(\vec{b})$ is the phase shift function.

Recall the partial wave expansion of the amplitude for scattering by a fixed scatterer in the diffraction theory,

$$f(\vec{q}) = \frac{ik}{2\pi}\int e^{i\vec{q}\cdot\vec{b}}\Gamma(\vec{b})d^2b, \tag{2.45}$$

where the $\vec{q}$ is the momentum transfer and it is small compared with the momentum $\hbar k$ where the amplitude is large.

It is clear that $f(\vec{q})$ and $\Gamma(\vec{b})$ are related to each other by Fourier transformation, i.e.

$$\Gamma(\vec{b}) = \frac{1}{2\pi ik}\int e^{-i\vec{q}\cdot\vec{b}} f(\vec{q}) d^2q, \tag{2.46}$$

where d^2q is in a plane perpendicular to $\vec{k}$.

We now generalize equation 2.46 to the case of the collision of a high-energy incident particle with a nucleus that has A nucleons. The positions of the A nucleons are $\vec{r}_1, \cdots, \vec{r}_A$, and the projections of these vectors on the plane perpendicular to $\vec{k}$ are $\vec{s}_1, \cdots, \vec{s}_A$. If the assumptions still hold and the nucleus goes from an initial state $|i\rangle$ to a final state $|f\rangle$ in the collision processes, then the diffraction amplitude of such collision is

$$F_{fi}(\vec{q}) = \frac{ik}{2\pi}\int e^{i\vec{q}\cdot\vec{b}} \langle f|\Gamma(\vec{b}, \vec{s}_1, \cdots, \vec{s}_A)|i\rangle d^2b. \tag{2.47}$$

To evaluate the profile function Γ, we think of the nucleus as a collection of refractive and absorptive objects whose refractive indices are not very different from unity. Then the incident wave is not greatly distorted when passing through the nucleus, and the phase shifts χ_j produced by individual nucleons combine additively[1]. The total nucleon phase shift function is

$$\chi(\vec{b}, \vec{s}_1, \cdots, \vec{s}_A) = \sum_{j=1}^{A} \chi_j(\vec{b} - \vec{s}_j). \tag{2.48}$$

Then the nuclear profile function is

$$\begin{aligned} \Gamma(\vec{b}, \vec{s}_1, \cdots, \vec{s}_A) &= 1 - e^{i\chi(\vec{b}, \vec{s}_1, \cdots, \vec{s}_A)} \\ &= 1 - \prod_{j=1}^{A} e^{i\chi_j(\vec{b} - \vec{s}_j)} \end{aligned}$$

[1]Omitting the internal degrees of freedom — charge, spin and isospin

$$
\begin{aligned}
&= 1 - \prod_{j=1}^{A}[1 - \Gamma_j(\vec{b} - \vec{s}_j)] \\
&= \sum_{j=1}^{A}\Gamma_j(\vec{b} - \vec{s}_j) - \\
&\quad \sum_{j<m}\Gamma_j(\vec{b} - \vec{s}_j)\Gamma_m(\vec{b} - \vec{s}_m) + \\
&\quad \cdots - (-1)^A \prod_j \Gamma_j(\vec{b} - \vec{s}_j). \qquad (2.49)
\end{aligned}
$$

The first term of the equation 2.49 is simply the sum of all individual nucleon profile functions of a nucleus. The higher order terms are corrections to the first term. For instance, the 2nd term represents the correction of the double counting of the double scattering processes.

Now, with the expression $\Gamma(\vec{b}, \vec{s}_1, \cdots, \vec{s}_A)$ and F_{fi}, we are able to construct the overall nuclear scattering amplitudes from the knowledge of the profile function Γ_j of the individual nucleons. Because many of the properties of the individual amplitude $f_j(\vec{q})$ can be known directly through experimental measurements, it is practical to obtain Γ using equation 2.49.

In the case of proton elastic scattering from deuterons, define the form factor

$$S(\vec{q}) = \int e^{i\vec{q}\cdot\vec{r}}|\phi(\vec{r})|^2 d\vec{r}, \qquad (2.50)$$

where $\phi(\vec{r})$ is the ground state wave function of the target nucleus. Then, apply the general expression for overall diffraction theoretical scattering amplitude F_{fi}

$$
\begin{aligned}
F_{fi} &= f_n(\vec{q})S(\frac{1}{2}\vec{q}) + f_p(\vec{q})S(\frac{1}{2}\vec{q}) + \\
&\quad \frac{i}{2\pi k}\int S(\vec{q}')f_n(\frac{1}{2}\vec{q} + \vec{q}')f_p(\frac{1}{2}\vec{q} - \vec{q}')d^2q', \qquad (2.51)
\end{aligned}
$$

where f_n and f_p are the spin independent scattering amplitudes of neutron and proton, respectively. The meaning of the above expression is clear. The first two

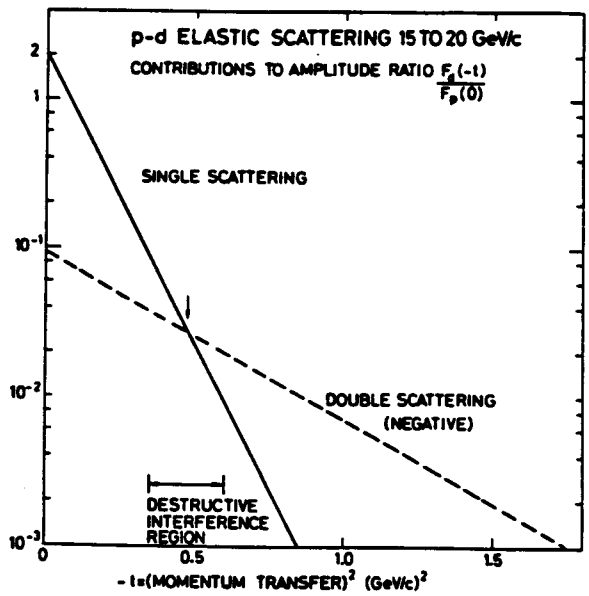

Figure 1. Contributions of single and double scatterings to the p-d elastic scattering amplitudes.

terms represent single scattering by neutron and by proton respectively, and the third term represents the double scattering by both of the proton and the neutron in the target deuteron nucleus.

Assuming f_n equals f_p and they are purely imaginary, then the single and double scattering amplitudes are shown in Figure 1 [9]. The small angle and larger angle scattering is dominated by single and double scattering processes, respectively. In a single scattering process, the momentum transfer is given to a single nucleon, and this tends to quite effectively break up the loosely bound deuteron nucleus. Understandably, the corresponding elastic scattering amplitude must decrease rapidly with increasing momentum transfer. On the other hand, the double scattering process in which the neutron and proton receive impulses of comparable magnitude has a much smaller chance to break up the deuteron

nucleus, and it is relatively insensitive to the deuteron structure. Note that the amplitudes of the two scattering processes are opposite in sign, so they interfere destructively and thus form a minimum of the scattering cross section in the region where these two processes having comparable strength. Because there is a small real part in both f_n and f_p, the minimum should not vanish.

The fact that the theory worked well in predicting the minimum in differential cross sections for spin 0 nuclei, such as ^{4}He and ^{16}O and not very well in the case of deuteron nucleus which has spin 1 (the experimental measurements have shown no appreciable minimum in deuteron cross sections) inspired the study of d-state effects on deuteron scattering. As a spin 1 nucleus, the ground state of the deuteron possesses a small d-state admixture (6$\sim$7 %). This small amount of d-state is determined in the integral by the squared amplitude, while the effect of the d-state on the differential cross section is linearly proportional to its amplitude. Therefore, the effect of d-state on the scattering is not necessarily small. Because of the ellipsoidal shape of the deuteron, its from factor must depend on the direction in which the deuteron spin is polarized,

$$S(\vec{q},\vec{J}) = S_0(\vec{q}) - \frac{1}{\sqrt{2}} S_2(\vec{q})[3(\vec{J}\cdot\hat{q}) - 2], \tag{2.52}$$

where $\vec{J}$ is the spin orientation of deuteron and $\hat{q}$ is the unit vector pointing to the direction of momentum transfer $\hbar\vec{q} = \hbar(\vec{k} - \vec{k}')$. S_0 is the isotropic component of the form factor,

$$S_0 = \int_0^\infty j_0(q,r)[\mu^2(r) + \omega^2(r)]dr, \tag{2.53}$$

and S_2 is the quadrupole form factor

$$S_2(q) = 2^{\frac{1}{2}} \int_0^\infty j_2(q,r)\omega(r)[\mu(r) - 8^{-\frac{1}{2}}\omega(r)]dr. \tag{2.54}$$

The internal wave function of a deuteron of magnetic sub-state m (m=±1, 0) relative to an axis $\hat{p}$ is

$$\Psi_{\hat{p},m}(\vec{r}) = \frac{1}{(2\pi)^{\frac{1}{2}}r}[\mu(r) + 8^{-\frac{1}{2}}\omega(r)]|\hat{p},m\rangle, \tag{2.55}$$

where $|\hat{p},m\rangle$ is the spin 1 spinor, μ and ω are the s and d state radial wavefunctions respectively.

The quadrupole form factor S_2 vanishes at small angles where S_0 dominates but rises rapidly while S_0 falls, and dominates the region where single and double scattering amplitudes interfere.

To calculate the quadrupole moment effect on the differential cross section, define scattering amplitude for a collision as

$$F(\vec{q},s) = F_1(\vec{q},s) + F_2(\vec{q},s), \tag{2.56}$$

where

$$F_1(\vec{q},s) = f_1(\vec{q})S(\frac{1}{2}\vec{q}) + f_2(\vec{q})S(-\frac{1}{2}\vec{q}) \tag{2.57}$$

$$F_2(\vec{q},s) = \frac{i}{4\pi k}\int S(\vec{q})[f_1(\frac{1}{2}\vec{q}+\vec{q}')f_2(\frac{1}{2}\vec{q}-\vec{q}') + \cdots \tag{2.58}$$

Then, the amplitude for a collision in which the deuteron has initial and final states m and m′ can be expressed as:

$$F_{m',m}(\vec{q}) = \langle\hat{p},m'|F(\vec{q},s)|\hat{p},m\rangle. \tag{2.59}$$

Chapter 3

Descriptions of Observables

In this Chapter, we introduce the concept of ensemble polarizations for spin-$\frac{1}{2}$ particle systems, and derive the formalism for the spin observables for the elastic scattering of spin-$\frac{1}{2}$ particles with arbitrary spin targets.

3.1 Spin-$\frac{1}{2}$ ensemble Polarizations

A single spin-$\frac{1}{2}$ particle can be represented by a Pauli spinor

$$\chi = \begin{pmatrix} a_1 \\ \\ a_2 \end{pmatrix}. \tag{3.1}$$

Such a spinor represents a spin state of the particle described by a complete state basis of two orthogonal states. Define the density matrix related to this spinor as

$$\rho = \chi\chi^{\dagger} = \begin{pmatrix} a_1 \\ \\ a_2 \end{pmatrix} \begin{pmatrix} a_1{}^* & a_2{}^* \end{pmatrix} = \begin{pmatrix} |a_1|^2 & a_1 a_2{}^* \\ \\ a_2 a_1{}^* & |a_2|^2 \end{pmatrix}. \tag{3.2}$$

The expectation value of an observable corresponding to a particular hermitian operator Ω can be expressed as

$$\begin{aligned}\langle\Omega\rangle &= \chi^{\dagger}\Omega\chi \\ &= \begin{pmatrix} a_1^* & a_2^* \end{pmatrix} \begin{pmatrix} \Omega_{11} & \Omega_{12} \\ \Omega_{21} & \Omega_{22} \end{pmatrix} \begin{pmatrix} a_1 \\ a_2 \end{pmatrix} \\ &= |a_1|^2\Omega_{11} + |a_2|^2\Omega_{22} + 2Re\Omega_{12}a_1a_2^* \\ &= Tr\rho\Omega. \end{aligned} \tag{3.3}$$

For an ensemble of N particles with $\chi^{(n)} = \begin{pmatrix} a_1^{(n)} \\ a_2^{(n)} \end{pmatrix}$ as the spinor of the nth particle, the ensemble average of the expectation of the operator Ω denoted by $\overline{\langle\Omega\rangle}$ is evidently given as

$$\overline{\langle\Omega\rangle} = \sum_{n=1}^{N} x^{(n)\dagger}\Omega x^{(n)}. \tag{3.4}$$

Define the ensemble density matrix ρ as the average of the densities of all the particles $\rho_{(n)}$:

$$\rho = \frac{1}{N}\sum_{n=1}^{N}\rho_{(n)} = \frac{1}{N}\begin{pmatrix} \sum_{n=1}^{N}|a_1{}^n|^2 & \sum_{n=1}^{N}a_1{}^n a_2{}^{n*} \\ \sum_{n=1}^{N}a_2{}^n a_1{}^{n*} & \sum_{n=1}^{N}|a_2{}^n|^2 \end{pmatrix}. \tag{3.5}$$

It can be easily verified that

$$\overline{\langle\Omega\rangle} = Tr\rho\Omega. \tag{3.6}$$

Then, with the Pauli spin operators

$$\begin{aligned}\sigma_x &= 2S_x = \begin{pmatrix} 0 & 1 \\ 1 & 0 \end{pmatrix}, \\ \sigma_y &= 2S_y = \begin{pmatrix} 0 & -i \\ i & 0 \end{pmatrix}, \\ \sigma_z &= 2S_z = \begin{pmatrix} 1 & 0 \\ 0 & -1 \end{pmatrix}, \end{aligned} \tag{3.7}$$

we define the ensemble polarization components p_x, p_y and p_z

$$\begin{aligned} p_x &\equiv \langle \sigma_x \rangle = Tr\rho\sigma_x = \frac{1}{N}\sum_{n=1}^{N} 2Re(a_1{}^{(n)}a_2{}^{(n)*}), \\ p_y &\equiv \langle \sigma_y \rangle = Tr\rho\sigma_y = \frac{1}{N}\sum_{n=1}^{N} 2Im(a_1{}^{(n)}a_2{}^{(n)*}), \\ p_z &\equiv \langle \sigma_z \rangle = Tr\rho\sigma_z = \frac{1}{N}\sum_{n=1}^{N} (|a_1{}^{(n)}|^2 - |a_2{}^{(n)}|^2). \end{aligned} \tag{3.8}$$

The unit matrix $I = \begin{pmatrix} 1 & 0 \\ 0 & 1 \end{pmatrix}$ ensemble expectation value

$$\langle I \rangle = Tr\rho\frac{1}{N} = \sum_{n=1}^{N} (|a_1{}^{(n)}|^2 + |a_2{}^{(n)}|^2) = 1. \tag{3.9}$$

If not normalized against N the $\langle I \rangle$ represents the particle number of the ensemble. The set of operators I, σ_x, σ_y and σ_z form a complete set of hermitian matrices for the 2×2 space so that any operator in this space can be expressed as a linear combination of these operators. Thus, a specification of the quantities p_x, p_y and p_z is a complete description of the polarization of the ensemble.

3.1.1 Analyzing Spin-$\frac{1}{2}$ Polarization

The cross section of the scattering of a spin $\frac{1}{2}$ particle incident beam with transverse polarization $\vec{p}$ off a target nucleus, as a consequence of parity conservation in nuclear reactions can be expressed as

$$I(\theta, \phi) = I_0(\theta)(1 + A(\theta)\vec{p} \cdot \hat{n}), \tag{3.10}$$

where $I_0(\theta)$ is the cross section with unpolarized incident beam, $A(\theta)$ is the analyzing power of the reaction, and $\vec{n}$ is the direction defined by the cross product of the incident and scattered proton wave vectors $\vec{k}_{in} \times \vec{k}_{out}$. Assuming the $\hat{n}$ component of the beam polarization, p_n is positive in the direction of $\hat{n}$ defined by the

$\vec{k}_{in} \times \vec{k}_{out}$ of the particles scattered to the left, then using I_L and I_R for the cross sections for *left* and *right* scatterings, we have

$$\begin{aligned} I_L &= I_0(1 + p_n A) \\ I_R &= I_0(1 - p_n A), \end{aligned} \tag{3.11}$$

so that

$$p_n A = A_{LR} = \frac{I_L - I_R}{I_L + I_R}, \tag{3.12}$$

where A_{LR} is the left-right asymmetry of the scattering.

3.2 Spin Rotation Observables

3.2.1 Coordinate Systems

We will discuss the ensemble polarizations and spin observables throughout this experiment in the most universally used laboratory *Helicity systems.* The incident particles are represented in the *projectile helicity frame* (X, Y, Z) with Z along particle's momentum $\vec{k}_{in}$, Y along the normal to the scattering plane, $\vec{k}_{in} \times \vec{k}_{out}$, and X forming a right-handed coordinate system with Y and Z; The *reactant helicity frame* (X', Y', Z') in which the outgoing particle is described, takes Z' along the reactant momentum $\vec{k}_{out}$, Y' still along the normal of the scattering plane and X' forming a right-handed coordinate system with Y' and Z'.

For later use, the coordinate system at the focal plane of the Medium Resolution Spectrometer (X'', Y'', Z'') in which the polarizations of the reactant of the second scattering (off carbon) is described, is defined similarly as the reactant helicity frame with Z'' along the second scattering outgoing momentum, X'' along X' of the reactant frame and Y'' chosen to form a right-handed coordinate system.

3.2.2 Observables

Because quantum mechanics is a linear theory, for the case of incident particle of spin $\frac{1}{2}$ with spinor χ_i scattered by a target of arbitrary spin, the outgoing spin $\frac{1}{2}$ particle with spinor χ_f is related to the incoming particle linearly[2],

$$\chi_f = M\chi_i, \tag{3.13}$$

where M is a 2×2 matrix whose elements are functions of incoming particle energy and outgoing particle scattering angle. As defined in Equation 3.2, the density matrices of the initial and final states are

$$\rho_i = \sum_{n=1}^{N} \chi_i^{(n)}[\chi_i^{(n)}]^\dagger \qquad \text{and} \tag{3.14}$$

$$\rho_f = \sum_{n=1}^{N} \chi_f^{(n)}[\chi_f^{(n)}]^\dagger, \tag{3.15}$$

respectively for an ensemble of N particles. Thus the density matrices ρ_i and ρ_f are related by the transform matrix M through

$$\rho_f = M\rho_i M^\dagger. \tag{3.16}$$

With ρ_i normalized to unity, the differential cross section for a polarized beam is given by

$$I(\theta,\phi) = Tr\rho_f = TrM\rho_i M^\dagger \tag{3.17}$$

for an unpolarized beam, $\rho_i = \frac{1}{2}\begin{pmatrix} 1 & 0 \\ 0 & 1 \end{pmatrix}$, and the differential cross section is reduced to

$$I_0(\theta) = \frac{1}{2}TrMM^\dagger. \tag{3.18}$$

[2]We use simpler spin 0 targets here for deriving the required density matrix. It can be proved [29] that all the arguments will remain true for spin non-zero targets.

In general, we can write the density matrix ρ in the complete 2×2 space base σ_i

$$\rho = \sum_{j=0}^{3} a_j \sigma_j. \tag{3.19}$$

Using the relation $Tr\sigma_i\sigma_j = 2\delta_{ij}$, $(i,j = 0,1,2,3$ or $0,x,y,z)$ with Equation 3.19, we have

$$2a_j = Tr\rho\sigma_j \equiv \langle\sigma_j\rangle = p_j. \tag{3.20}$$

Thus for an incident particle ensemble, the density matrix is

$$\rho_i = \frac{1}{2}\sum_{j=0}^{3} p_j\sigma_j = \frac{1}{2}(1 + \sum_{j=1}^{3} p_j\sigma_j). \tag{3.21}$$

Substitute Equation 3.21 in the Equation 3.16, we have

$$\rho_f = \frac{1}{2}MM^\dagger + \frac{1}{2}\sum_{j=1}^{3} p_j M\sigma_j M^\dagger. \tag{3.22}$$

Using the Equation 3.17, we obtain the cross section for the polarized beam as

$$I(\theta,\phi) = I_0(\theta)(1 + \sum_{j=1}^{3} p_j A_j(\theta)), \tag{3.23}$$

where

$$A_j(\theta) = \frac{TrM\sigma_j M^\dagger}{TrMM^\dagger} \tag{3.24}$$

is the jth analyzing power component.

To calculate the polarization of the scattered particles, we normalize the matrix density ρ_f as $\frac{\rho_f}{Tr\rho_f}$ so to have trace unity, then

$$p_{k'} \equiv \langle\sigma_{k'}\rangle = \frac{Tr\rho_f\sigma_{k'}}{Tr\rho_f} = Tr\rho_f\sigma_{k'}. \tag{3.25}$$

With Equation 3.22, we have

$$p_{k'}I(\theta,\phi) = I_0(\theta)(P_{k'} + \sum_{j=1}^{3} p_j D_j^{k'}(\theta)), \tag{3.26}$$

where

$$P_{k'} = \frac{TrMM^{\dagger}\sigma_{k'}}{TrMM^{\dagger}} \tag{3.27}$$

and

$$D_j^{k'}(\theta) = \frac{TrM\sigma_j M^{\dagger}\sigma_{k'}}{TrMM^{\dagger}}. \tag{3.28}$$

The cross section (Equation 3.23) and polarization transfer relation (Equation 3.26) can be written in their fully expanded form[3]

$$I(\theta,\phi) = I_0(\theta)(1 + p_X A_X(\theta) + p_Y A_Y(\theta) + p_Z A_Z(\theta)) \tag{3.29}$$

$$p_{X'}I(\theta,\phi) = I_0(\theta)(P_{X'}(\theta) + p_X D_X^{X'}(\theta) + p_Y D_Y^{X'}(\theta) + p_Z D_Z^{X'}(\theta)) \tag{3.30}$$

$$p_{Y'}I(\theta,\phi) = I_0(\theta)(P_{Y'}(\theta) + p_X D_X^{Y'}(\theta) + p_Y D_Y^{Y'}(\theta) + p_Z D_Z^{Y'}(\theta)) \tag{3.31}$$

$$p_{Z'}I(\theta,\phi) = I_0(\theta)(P_{Z'}(\theta) + p_X D_X^{Z'}(\theta) + p_Y D_Y^{Z'}(\theta) + p_Z D_Z^{Z'}(\theta)). \tag{3.32}$$

$P_{k'}$ is the k'th polarization component of the scattered particles from an unpolarized beam induced by the target, and $D_j^{k'}(\theta)$ is the polarization (spin) transfer coefficient that relates the jth initial polarization component to the k'th final polarization component. All of the polarization observables vary between $+1$ and -1 for the spin $\frac{1}{2}$ case. The forms of Equation 3.23 and 3.26 are the most general allowed by the conservation of angular momentum. The conditions imposed by parity conservation and time reversal invariance are discussed next.

Under parity transformation all polar vectors reverse sign, which include $\vec{k}_{in} \rightarrow -\vec{k}_{in}$, $\vec{k}_{out} \rightarrow -\vec{k}_{out}$, $X \rightarrow -X$, $X' \rightarrow -X'$, $Z \rightarrow -Z$ and $Z' \rightarrow -Z'$, but Y and Y' $(= \vec{k}_{in} \times \vec{k}_{out})$ remain unchanged. The spin operators, being pseudovectors, are also unchanged. If parity is conserved, the transformed system must be identical to the initial system. Thus, if N_X, N_Y and N_Z are the number of times X, Y and

[3] X, Y, Z and x, y, z (or equivalently, S, N, L and s, n, l, i.e. *Sideways, Normal, Longitudinal* relative to particle momentum direction) are denoted for Lab system and CM system respectively here and in the following content of this thesis.

Z appear in a particular coefficient respectively, the parity conservation requires the non-vanishing spin observables to have even $N_X + N_Z$ values, therefore, A_Y, $P_{Y'}$, $D_X^{X'}$, $D_Y^{Y'}$, $D_Z^{Z'}$, $D_X^{Z'}$ are $D_Z^{X'}$ non-vanishing.

The time reversal invariance requires that the polarization transfer coefficients of the inverse reaction be $(-1)^{N_Y+N_Z+r+r'}$ times the corresponding coefficients of the forward reaction, provided the CM helicity frames are used. The quantities r and r' are the ranks of the quantities connected by the transfer coefficient being considered; in this case, $r = r' = 1$. If parity conservation also holds, the factor may be written as $(-1)^{N_Z}$. Thus, time reversal invariance implies that $A_Y = \overline{P_{Y'}}$, $P_Y = \overline{A_{Y'}}$, $D_Z^{X'} = -\overline{D_X^{Z'}}$, $-D_X^{Z'} = \overline{D_Z^{X'}}$, $D_X^{X'} = \overline{D_X^{X'}}$ and $D_Z^{Z'} = \overline{D_Z^{Z'}}$. The overlined coefficients are expressed in the CM helicity frame appropriate to the time reversed reaction. For the case of elastic scattering, the forward and inverse reactions are identical, then the above implications reduce to

$$A_Y = P_{Y'} \qquad D_Z^{X'} = -D_X^{Z'}. \tag{3.33}$$

Now the Equation 3.23 and 3.25, under the application of the parity conservation and the time reversal invariance, may be expressed as

$$\begin{pmatrix} p_{X'} \\ p_{Y'} \\ p_{Z'} \end{pmatrix} = \frac{1}{1 + p_Y A_Y} \left[\begin{pmatrix} 0 \\ P_{Y'} \\ 0 \end{pmatrix} + \begin{pmatrix} D_X^{X'} & 0 & D_Z^{X'} \\ 0 & D_Y^{Y'} & 0 \\ D_X^{Z'} & 0 & D_Z^{Z'} \end{pmatrix} \begin{pmatrix} p_X \\ p_Y \\ p_Z \end{pmatrix} \right]. \tag{3.34}$$

It can be shown that the rotation invariance requires an observable to be an odd (even) function of the scattering angle θ if $N_X + N_Y$ is odd (even). Thus, among the non-vanishing spin observables, A_Y, $D_Z^{X'}$, $P_{Y'}$ and $D_X^{Z'}$ are odd while $D_X^{X'}$, $D_Y^{Y'}$, $D_Z^{Z'}$ are even functions of θ.

Chapter 4

Experimental Details

4.1 Experiment E482

TRIUMF experiment E482, the *"Measurement of Spin Observables for Proton-Deuteron Elastic Scattering"* was proposed and executed on the Beam Line 4B of the TRIUMF Cyclotron using the Medium Resolution Spectrometer (MRS), In Beam Polarimeter (IBP) and Focal Plane Polarimeter (FPP) as the main detectors. The experiment was executed with incident proton beam energies of 290 and 400 MeV for each of the three beam polarizations, *sideways, normal* and *longitudinal* (S, N, L). The proton scattering angle at each beam energy ranged from 20 to 80° in the laboratory system. The target was a CD_2 slab of thickness 200 mg/cm^2. Table 3 and 4 indicate the estimates of number of counts entering the MRS (N_{tot}) and those accepted by the FPP (N_{sc}) with the proton scattering angle (θ_{lab}) and kinetic energy ($T_{p'}$) for an statistical error in focal plane polarization of ± 0.02 for the chosen incident proton kinetic energies (T_p). The detector efficiency (ϵ), the average p-C analyzing powers ($\langle A_c \rangle$) and the thickness of the carbon analyzer slab (t_{carbon}) were taken from the FPP handbook at TRIUMF. The differential cross sections ($\frac{d\sigma}{d\Omega}|_{lab}$) were interpolated from tables by Seagrave *et al.* [33] and translated

Table 3. Experiment configurations T_p=290 MeV

θ_{lab} (°)	$T_{p'}$ (MeV)	χ (°)	ϵ (%)	$\langle A_c \rangle$ (%)	t_{carbon} (cm)	N_{sc} ($\times 10^3$)	N_{tot} ($\times 10^6$)	$\frac{d\sigma}{d\Omega}\|_{lab}$ ($\frac{\mu b}{sr}$)
20	270	139	2.0	43	7.5	27	1.4	1300
30	248	136	1.0	48	4.5	22	1.2	360
40	220	133	1.0	52	4.5	18	1.8	150
50	190	129	1.0	52	4.5	18	1.8	85
60	160	126	1.0	48	4.5	22	2.2	60
70	132	123	1.0	37	4.5	37	3.7	50
80	107	120	1.0	26	4.5	74	7.4	70

Table 4. Experiment configurations T_p=400 MeV

θ_{lab} (°)	$T_{p'}$ (MeV)	χ (°)	ϵ (%)	$\langle A_c \rangle$ (%)	t_{carbon} (cm)	N_{sc} ($\times 10^3$)	N_{tot} ($\times 10^6$)	$\frac{d\sigma}{d\Omega}\|_{lab}$ ($\frac{\mu b}{sr}$)
20	372	150	3.2	35	10.5	41	1.3	480
30	339	146	2.0	38	7.5	35	1.7	110
40	300	142	2.0	42	7.5	28	1.4	35
50	258	137	1.0	47	4.5	23	2.3	35
60	217	132	1.0	52	4.5	18	1.8	25
70	178	128	1.0	52	4.5	18	1.8	30
80	144	124	1.0	39	4.5	33	3.3	35

into the lab frame. $\chi = \gamma(\mu - 1)\alpha$ is the MRS dipole precession angle, where α is the bend angle of the dipole, γ is the relativity factor, and μ is the proton magnetic moment.

The heart of this experiment was the measurement of polarizations. The In Beam Polarimeter was used to monitor the transverse (to the beam transport direction) polarization components (P_N, P_S) of the incident proton beam in its projectile-helicity-coordinate system before being scattered by the target. The longitudinal beam polarization component (P_L) was monitored indirectly using the transverse polarization information from the IBP (or using beam line 4A).

The most important and crucial part of the experiment was the measurement of polarization components ($P_{N''}$, $P_{S''}$) of the scattered protons, which was carried out with the focal plane polarimeter (FPP), located above the medium resolution spectrometer (MRS) focal plane. For the analyzing power measurement, the p-d elastic scattering asymmetry was measured with the MRS using incident beams of normal polarization with alternating polarities, i.e. spin "up" and "down". The asymmetry information was used for off-line calculation of the reaction analyzing powers. Figure 2 shows a schematic of the experimental detector system which includes mainly the MRS and the FPP. The information from the Front End Chambers (FECs) and the Vertical Drift Chambers (VDCs) of the MRS were used to reconstruct focal plane position, target position and other secondary coordinates of the scattered protons; The multi-wire chambers (D1 through D4) of the FPP were used to determine proton scattering angles from the carbon scatterer, which are necessary for the determination of the polarization of the protons at the focal plane; Two thin scintillator counters, S1 and S2, provided trigger signals for the detector system.

Figure 3 illustrates the three coordinates systems used for proton polarization representation, in which S, N and L denote the directions of "sideway", "normal" and "longitudinal" polarizations, respectively in the lab system. The non-primed system describes the incident proton beam polarizations; The single-primed system describes the polarizations of the scattered protons, and the double-primed system describes the scattered proton polarizations at the MRS focal plane.

A recoil deuteron scintillator counter was used to exclude the background from proton-carbon and many body inelastic final states, except at 20° where there was not enough space for the recoil counters.

The cross sections of the p-d elastic scattering at the proposed energy and scat-

tering angle ranges were estimated ranging from about 25 to 1300 μb/sr (Table 3 and 4). The detector counting rate was mainly limited by the speed of the data acquisition system. The single event processing time was 0.5 μs, and a good event data transfer and recording time was 3.0 ms. In order to have a less than 10% detector system dead time (taking the typical detector system efficiency of 4%), the event rate was kept bellow 600/sec, which corresponds to the beam current in the range of 0.13 – 18 nA.

4.2 TRIUMF Cyclotron and Beam Line 4B

Figure 4 shows a general layout of the TRIUMF facility. The TRIUMF Cyclotron is a 6-sector isochronous cyclotron accelerating H^- ions to a continuously variable energy ranging between 183 and 507 MeV with a time structure of 3ns beam pulse in every 43ns. Beam extraction is achieved by passing part or all (depending on the desired beam intensity) of the H^- circulating beam through a stripping foil, stripping off the electrons from the H^- ions and producing protons which bend out of the cyclotron into the beam line. The energy of the protons is determined by the distance of the stripping foil from the center of the cyclotron.

An Ehlers type of unpolarized H^- ion source is used for unpolarized beam producing 140 μA of unpolarized beam. For polarized beam, a Lamb-shift polarized H^- ion source was used capable of producing up to 600 nA of extracted polarized beam with polarization of 75 to 80%. The direction of the polarization vector at beam extraction is vertical, i.e. perpendicular to the accelerating plane of the cyclotron. The polarities of the beam polarizations can be switched to positive (or "up"), negative ("down") or off for each beam polarization mode.

The beam line 4B is located in the Proton Hall experimental area. It is cou-

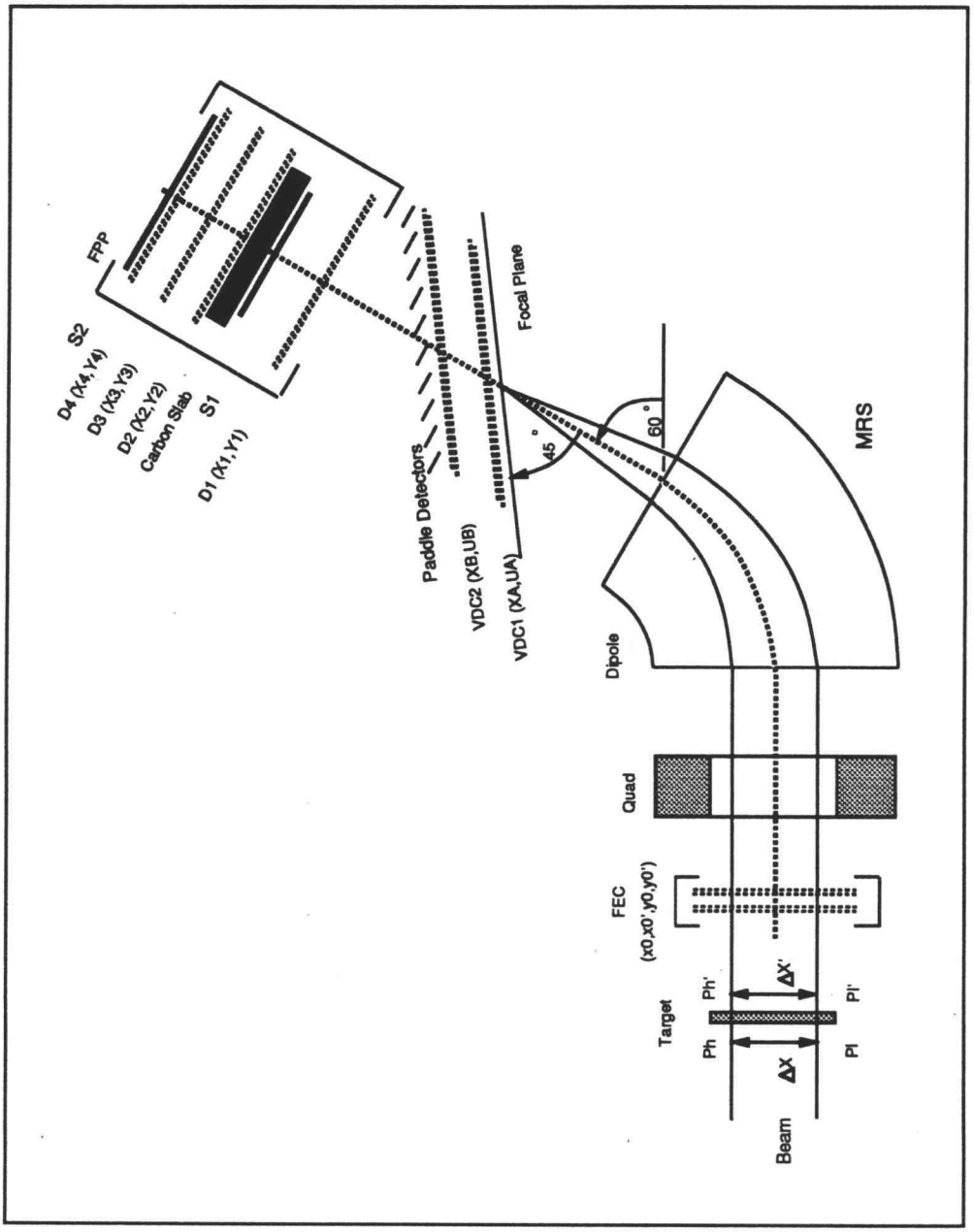

Figure 2. The schematic of experimental detector systems

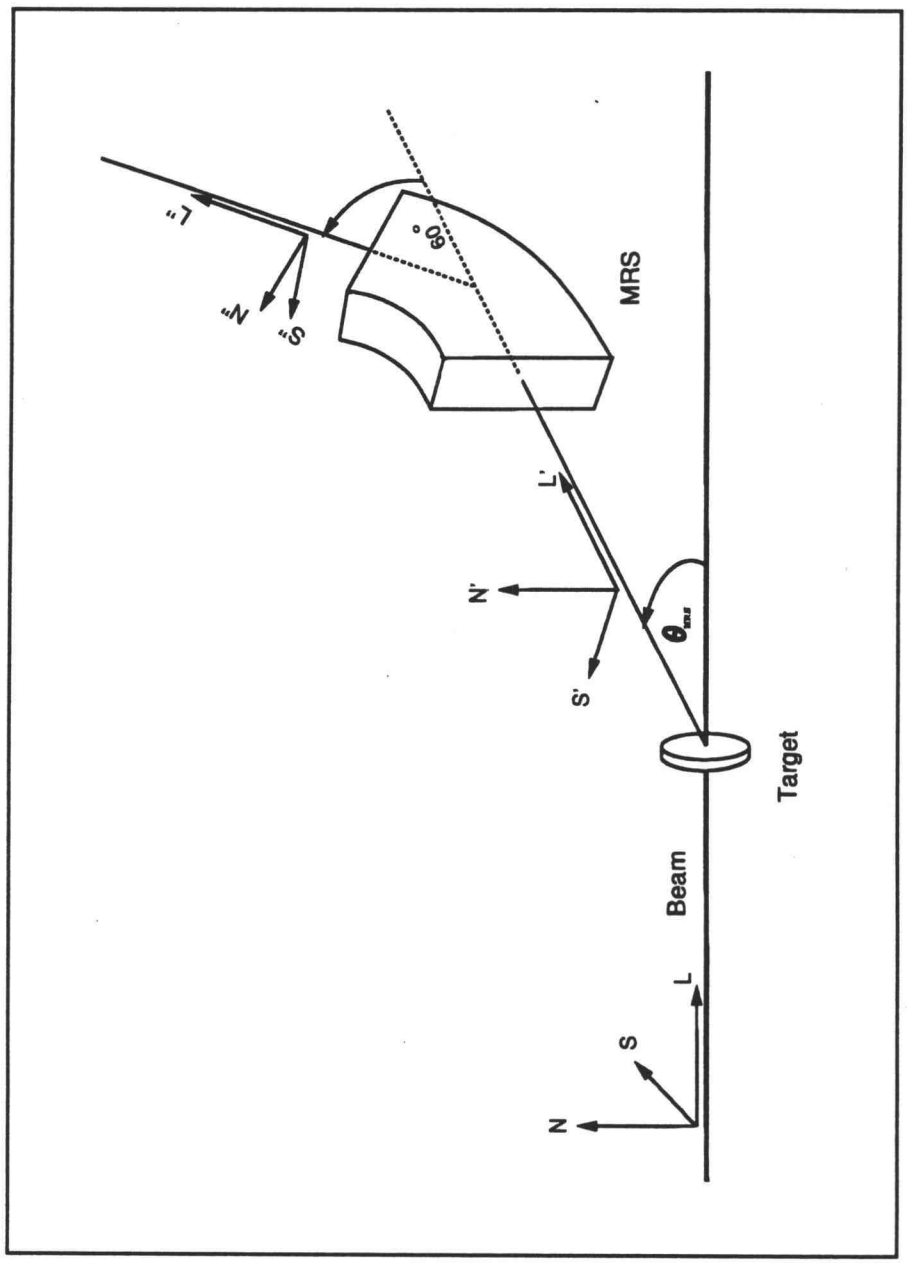

Figure 3. The three coordinate systems for describing the proton polarizations

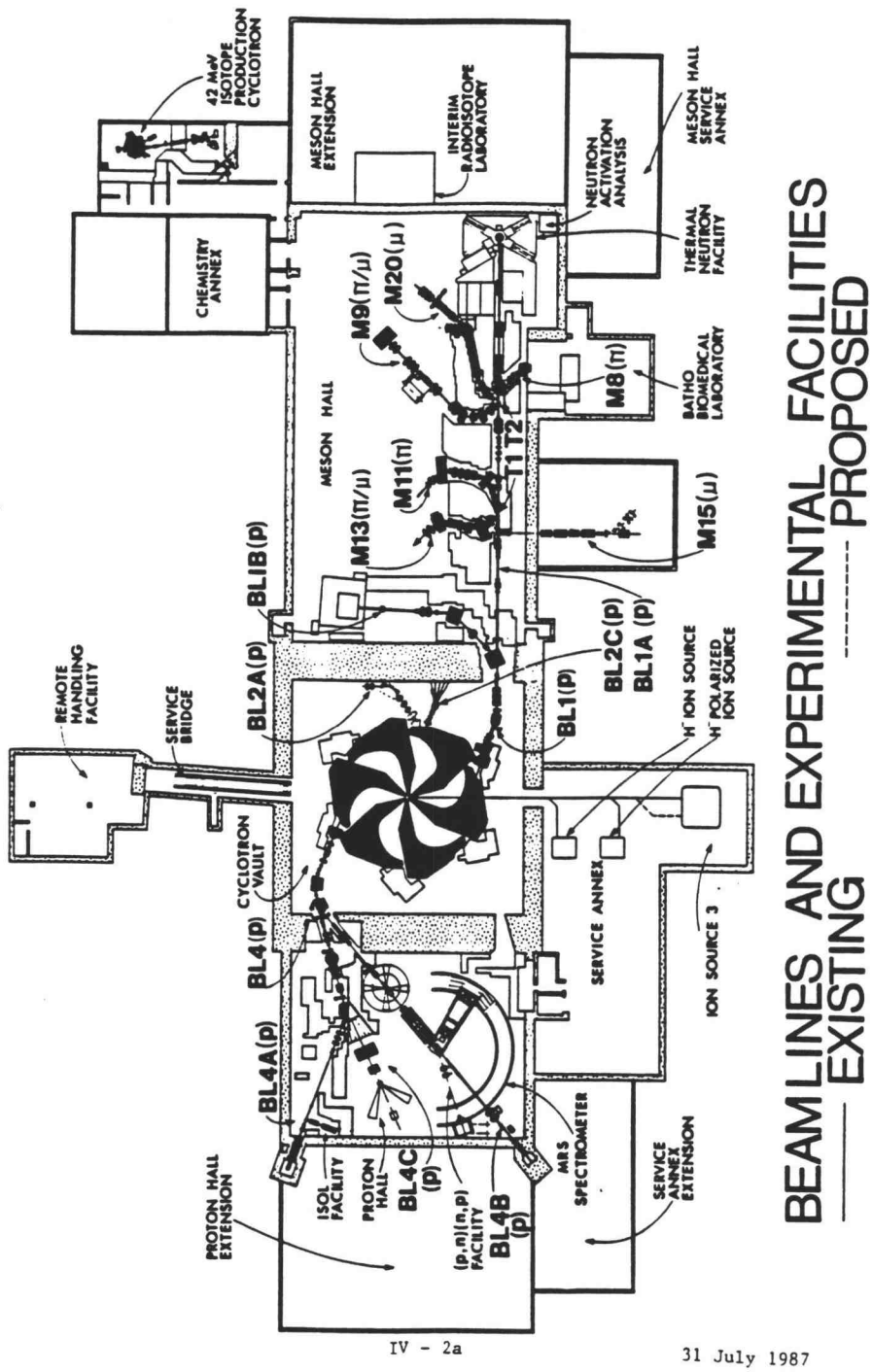

Figure 4. A general layout of the TRIUMF Cyclotron Facility

pled with the medium resolution spectrometer at the target vertex. The proton beam in beam line 4B can be operated either unpolarized or polarized with all three polarizations available from 183 to 507 MeV. Schematically speaking, beam line 4B consists of a combination of bending magnets, solenoids, sets of focusing/defocusing quadrupoles, the in beam polarimeter, the MRS target vertex, and beam dump, which are illustrated in Figure 5

The bending magnets B1 and B2 serve primarily to steer the proton beam into beam line 4B; The combined precession effects of B1, B2 and solenoids S1, S2 is capable of producing longitudinal beam polarization. Besides precessing the transverse polarization, the solenoids also changes the beam property by rotating its dispersion orientation, which may be compensated by adjusting the setting of the "twister" with respect to the beam axis. The twister is a set of six 4-inch quadrupoles mounted in a frame. It has the magnification of $+1$ and -1 in two orthogonal directions transverse to the beam. For instance, when the beam disperses horizontally at the IBP, the ensemble may be rotated about the beam axis to the $0°$ setting [30]; now the opposite signs of the two magnification have the effect of "twisting" the horizontal dispersion at the IBP into a vertical dispersion at MRS target, making possible dispersion matching with the MRS.

4.3 Beam Polarization

When the Lamb-Shift polarized H^- ion source is used the beam polarization at the beam extraction is vertical. So if all the solenoids are left off, i.e. no transverse polarization component precession occurs, then the beam polarization direction is "normal". When placed in a magnetic field, the spin orientation of a particle precesses about the magnetic field direction. Provision of sideways polarized beams was accomplished with a solenoid external to the vault in the beam line 4B

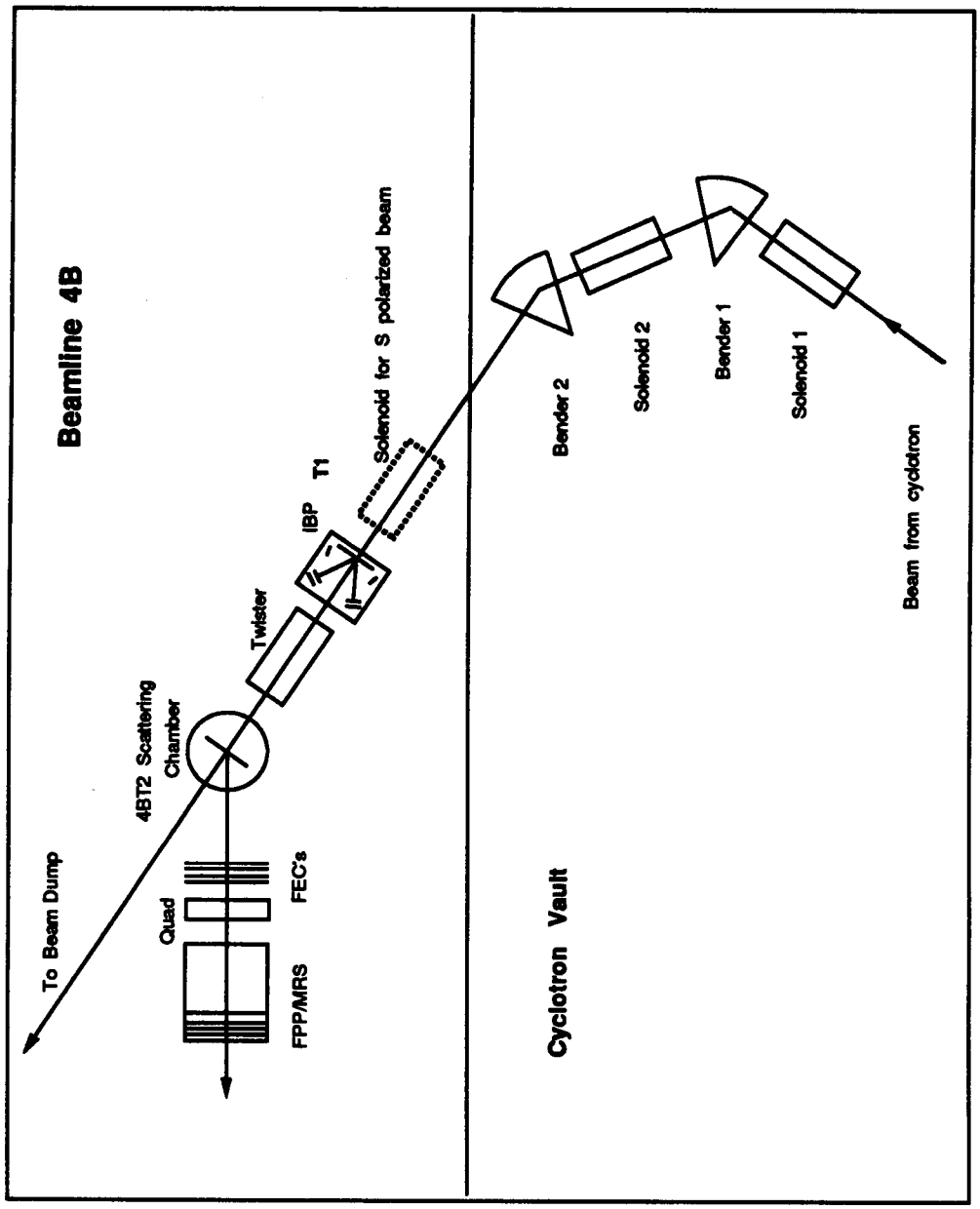

Figure 5. A schematic of the Beam Line 4B

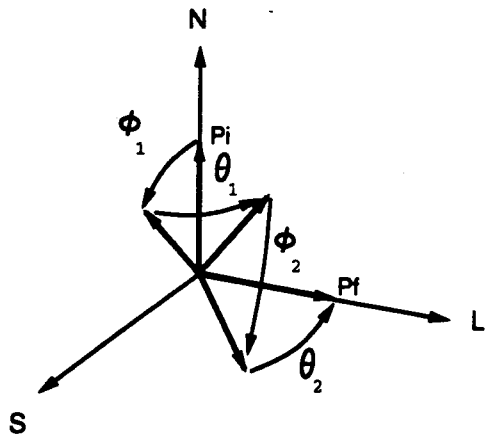

Figure 6. Process involved in the transformation of an initially normal polarization into completely longitudinal polarization

which precesses the beam polarization 90° about the beam axis from "normal" to "sideways". The longitudinal beam polarization was made available utilizing two solenoids (1 and 2 in Figure 5) combined with the two bending dipoles (bender 1 and bender 2). This precession system is able to precess an "normal" polarization into "longitudinal" polarization. The angle of precession in a solenoid (ϕ) and that in a dipole magnet (θ) are related to the solenoid and dipole properties by [31]

$$\phi = \mu[B_0 L/(B\rho)_0], \tag{4.1}$$

$$\theta = \gamma G \alpha, \tag{4.2}$$

in which, μ is the magnetic moment of the particle, B_0 is the axial field of the solenoid, L is the effective length of the solenoid, $(B\rho)_0$ is the magnetic rigidity of the particle, $G = (g/2 - 1) = 1.79285$, and α is the bend angle of the dipole. Figure 6 shows the process involved in the transformation of an initially normal polarization into completely longitudinal polarization.

As the in beam polarimeter monitors only the transverse (normal and sideways) polarization components, there is no direct measurement of the longitudinal beam polarization. The value of the normal polarization component just before switching to longitudinal mode or after switching back from L mode is usually used as the L polarization component in L mode, assuming negligible polarization drifting over a short period of time. Small N and S components, when in L mode (comparable to the S component when in N mode) are indirect indications of correct precession.

4.4 In Beam Polarimeter (IBP)

The beam line 4B in beam polarimeter serves as the primary monitor of the beam intensity and transverse polarizations. It consists of a thin polyethylene (CH_2) target, and a pair of scintillator telescopes one on each side of the beam in both the vertical and horizontal planes. Each telescope (Left, Right, Top and Bottom) is at 17° from beam axis and in coincidence with a recoil scintillator counter. The telescopes count the p-p coincidences from the reaction of proton-proton elastic scattering. The accidental coincidences are formed by coincidence between scattered particles and recoil signals delayed by a beam cycle as shown in the logic diagram, Figure 7.

Take the example of the normal beam polarization component measurement. The asymmetry of the counts taken in the left and right telescopes is defined by

$$A_s = \frac{L - R}{L + R}, \tag{4.3}$$

where the L and R are the left and right telescope real coincidence counts less accidental coincidences. Then the normal polarization component of the beam can be calculated by

$$P_N = \frac{A_s}{A_N(p,p)}, \tag{4.4}$$

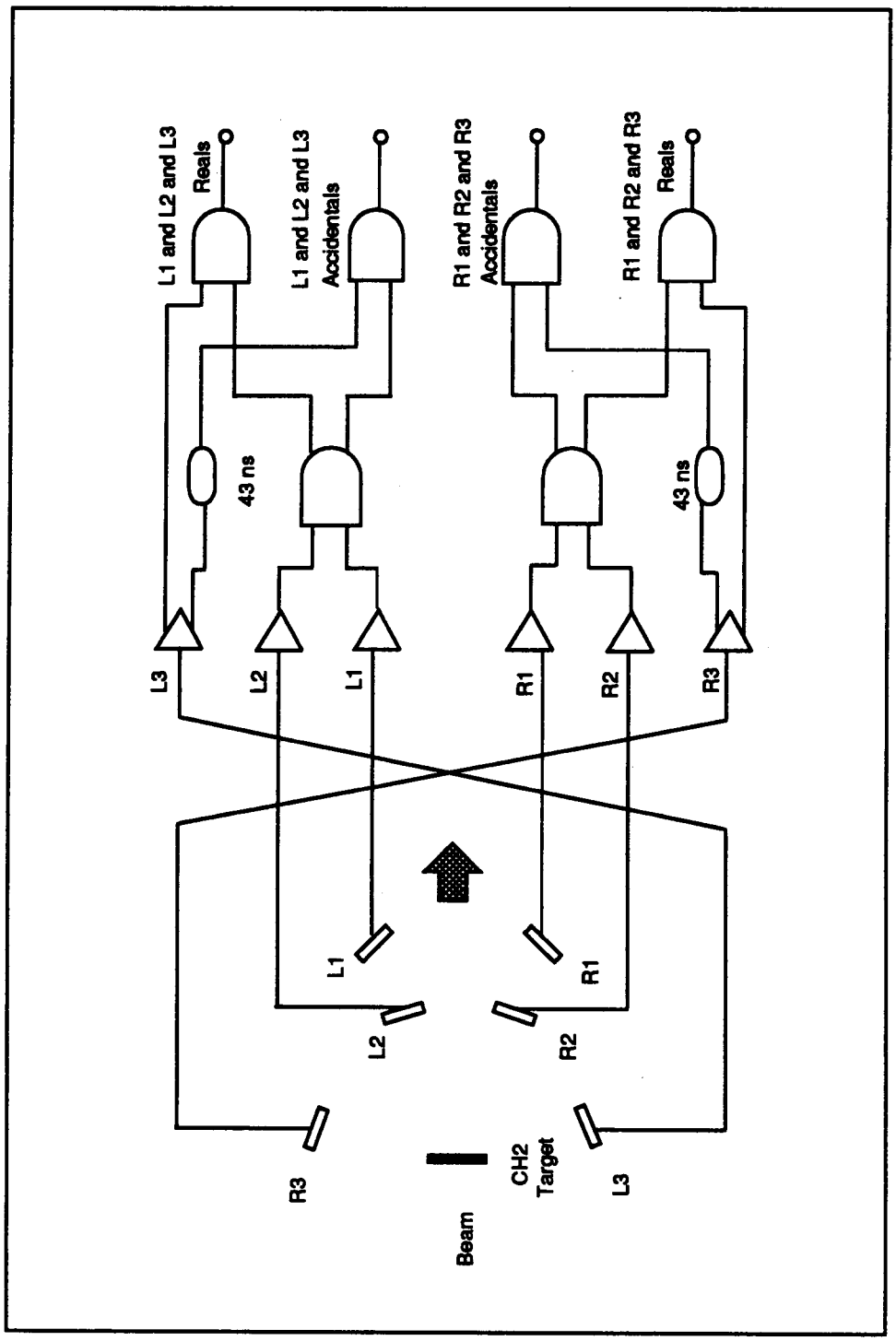

Figure 7. A schematic of the beam line 4B In Beam Polarimeter logic

Table 5. Beam Normalization Values

Beam Energy (MeV)	(L+R) $\frac{counts}{secXnAX(mg/cm^2)}$	$A_N(CH_2)$	SEM $\frac{counts}{secXnA}$
200	46.8	0.285	10.82
250	49.1	0.344	9.467
300	51.9	0.387	8.514
350	55.4	0.416	7.869
400	59.5	0.434	7.346
450	64.2	0.456	6.947
500	69.6	0.466	6.636

provided the proton-proton elastic analyzing power $A_N(p,p)$ is known at 17°. See Table 5 [30]

The sideways polarization beam component is similarly measured with the top and bottom telescopes of the IBP.

There is no direct measurement of the longitudinal polarization component. For indirect measurement, however, during the experiment, the primary proton beam was periodically switched to the beam line 4A (BL4A in Figure 4) in the Proton Hall which has a in beam polarimeter similar to that of beam line 4B. The transverse polarization component of the beam in BL4A is related to the longitudinal component of the beam in BL4B by the transport and precessing parameters of the beam line systems and therefore can be used as a monitor for the longitudinal polarization of the beam in BL4B.

Slight lateral movement of the primary beam at the polarimeter target could cause false asymmetry in the counting rates because the target-to-detector distances are no longer the same (causing solid angles to differ) and the mean scattering angles are no longer the same (causing different unpolarized differential cross sections within the angle ranges subtended by the two arms) for the left and right

(top or bottom) detectors. To eliminate such an instrumental asymmetry to the first order, the solid-angle-defining counters of the forward arms were rotated so that they are no longer normal to the line joining their center and the center of the target. As a result the solid angle subtended by the left (right) counter will increase (decrease) as the beam moves to the right (left) at the target, for example. This may compensate both the distance factor and the effect of changing cross section.

The last column of Table 5 is the Faraday cup calibrated rate of another beam current monitor, the Secondary Emission Monitor (SEM) which is located down stream of T2 of the beam line 4B and just in front of the beam dump. The SEM collects electrons from surface emission as the proton passes through several gold foils. The number of electrons given off is proportional to the Stopping Power ($\frac{dE}{dx}$) and is independent of the foil thickness.

4.5 Medium Resolution Spectrometer (MRS)

The Medium Resolution Spectrometer is a magnetic prism. It disperses charged particle momentum at its focal plane so events of different nature (with different energies) can be identified. The MRS consists of a magnetic quadrupole and a bending dipole to transport charged particles, and front end chambers and vertical drift chambers to measure particle trajectories and momenta. It pivots at target 4BT2 and can cover laboratory scattering angle from $-12°$ to $+140°$. Its acceptance solid angle, depending upon its run mode, can be from .5 to 2 msr. Its momentum acceptance is $\pm 7\%$ at 1.5 GeV/c. The MRS optical axis bends (in the dipole) 60° in the vertical plane. Figure 8 shows a scaled MRS picture.

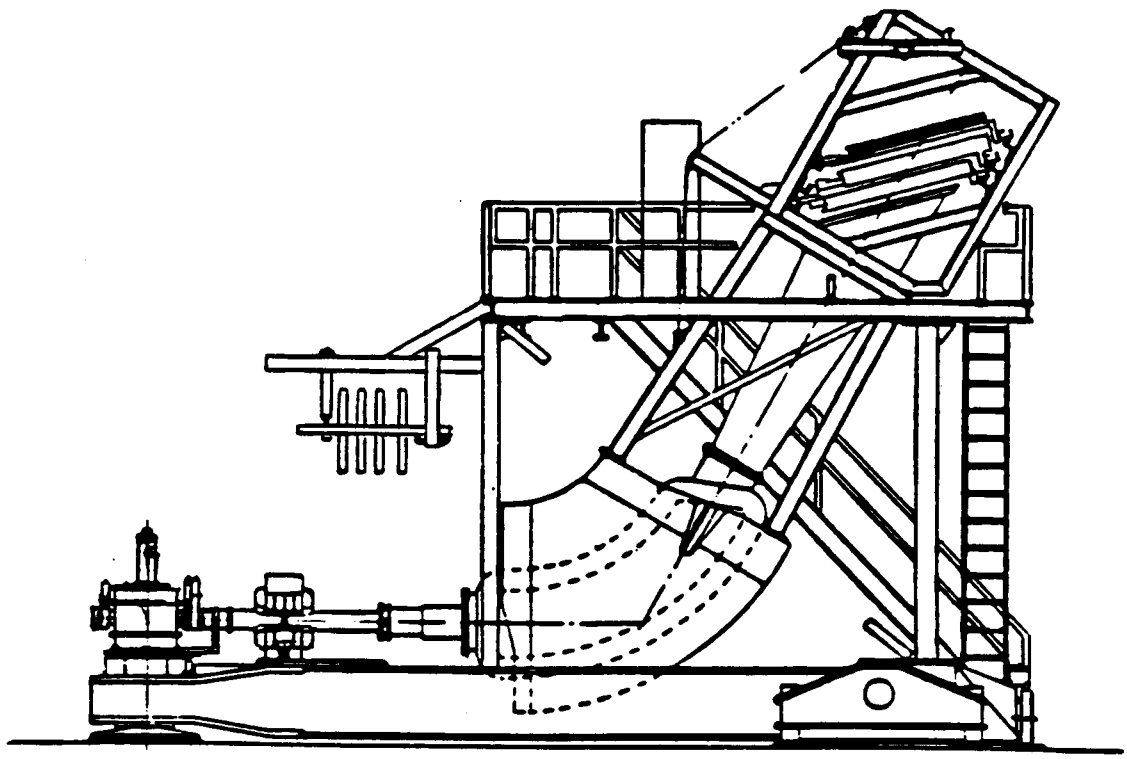

Figure 8. A scaled MRS picture

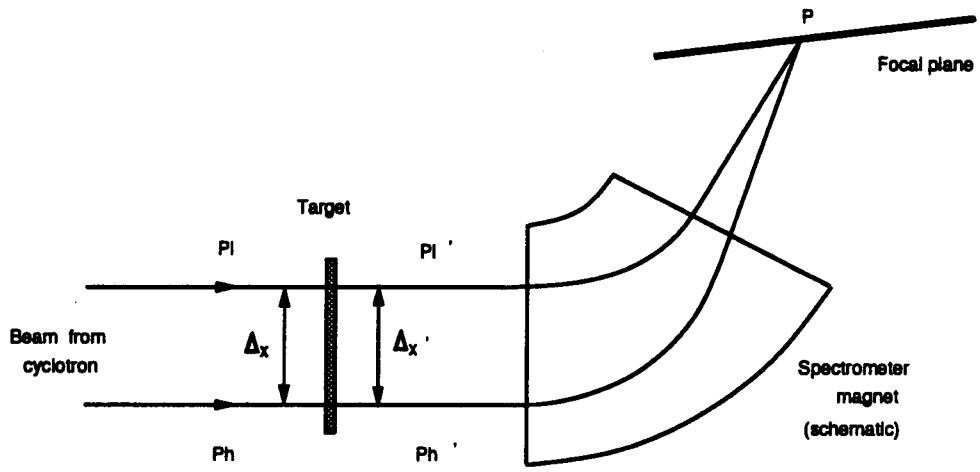

Figure 9. Illustration of dispersion matching technic

4.5.1 Dispersion Matching

In order to ensure the highest possible momentum resolution of MRS [4], it is important to match the beam dispersion at the target with that of the MRS acceptance (see illustration 9), so that the excitation energy resolution is made independent of the energy spread in the incident beam.

An ideal bending magnet works just like an optical prism. If a non-dispersed ($\Delta X = 0$), non-monoenergetic charged particle beam with momentum spread from P'_L to P'_H was emitted from the point P at the focal plane passing through the dipole magnet reversely, the particles of different momenta would be spread out (dispersed) in space at the target position (entrance of the magnet), i.e. $\Delta X' > 0$. The dispersion is related to the momentum spread as the following,

$$\Delta X' = \frac{D_s}{M_s} \frac{(P'_H - P'_L)}{\overline{P'}}, \tag{4.5}$$

[4]This experiment had used achromatic beam mode, instead of dispersion matching, so this section should be considered as a general description of an useful aspect of the MRS system.

where D_s, M_s is the dispersion, magnification of the spectrometer respectively, and $\overline{P'} = (P'_H + P'_L)/2$ is the average momentum. If this imaginary process were done exactly reversely, i.e. if a beam of dispersion of equation 4.7 from the target traveled through the magnet to the focal plane, it would focus at a single point P at the focal plane.

For a beam transport system with dispersion D_t, a beam of momentum spread ranging from P_L to P_H would be spread at the target as

$$\Delta X = D_t \frac{(P_H - P_L)}{\overline{P}}, \tag{4.6}$$

where $\overline{P} = (P_H + P_L)/2$ is the average momentum. From above arguments, if the beam dispersion ΔX were matched with $\Delta X'$, then all the particles after the target would be focused at a single point at the focal plane, and the highest momentum resolution would be achieved. We then have the general dispersion-matching condition

$$D_t \frac{(P_H - P_L)}{\overline{P}} = \frac{D_s}{M_s} \frac{(P'_H - P'_L)}{\overline{P'}}. \tag{4.7}$$

For the reactions in which the proton energy loss is small enough so that $P'_H = P_H$ and $P'_L = P_L$, then the condition is simply

$$D_t = \frac{D_s}{M_s}. \tag{4.8}$$

Otherwise, the required beam line dispersion should be calculated with the dispersion matching condition, equation 4.7.

4.5.2 Detectors

As illustrated in Figure 2 and 5, the detector system used in this experiment includes mainly the In Beam Polarimeter, the Medium Resolution Spectrometer

and the Focal Plane Polarimeter. We have introduced the IBP beam polarization monitor system in Section 4.4 and now we discuss the MRS detectors.

Front End Chamber (FEC)

The Front End Chamber is the first detector of MRS intercepting the scattered particles. It measures the vertical (Y0) and horizontal (X0) coordinates of the particle passing through the chamber. The particle coordinates can be used for (a), aberration corrections and (b), together with the VDC trajectory information, reconstruction of the coordinates at the target (Chapter 5), which is important for excluding the events not originating from the target.

The FEC covers an area of $8cm \times 8cm$ with 4 wire planes. Two of the wire planes measure the horizontal position of the particles trajectories ($X0$ and $X0'$) and the other two measure the vertical positions ($Y0$ and $Y0'$), see Figure 2. Each wire plane consists of 16 pairs of alternating anode and cathode wires. The primed planes are offset from the unprimed planes by one half of the anode wire spacing.

Figure 10 illustrates the FEC wire configurations. With the struck wire number N and N' and the drifting time T and T' ($T(') = const - t(')$, TDC values), the coordinate (e.g. X) of the particle trajectory at the FEC can easily be derived,

$$X = \frac{L}{4}(1 + \frac{T' - T}{t_l}), \tag{4.9}$$

and, in the FEC coordinate system, the particle position is

$$X0 = NL + [2(N' - N) - 1]X, \tag{4.10}$$

where $L = 5.0$ mm is the inter anode spacing, t_l is electron drift time at a distance of $l = L/2$. In deriving Equation 4.10 the relations $N = chn - First$ and $N' = Last - chn'$ were used, where the chn and chn' are the channel numbers of the

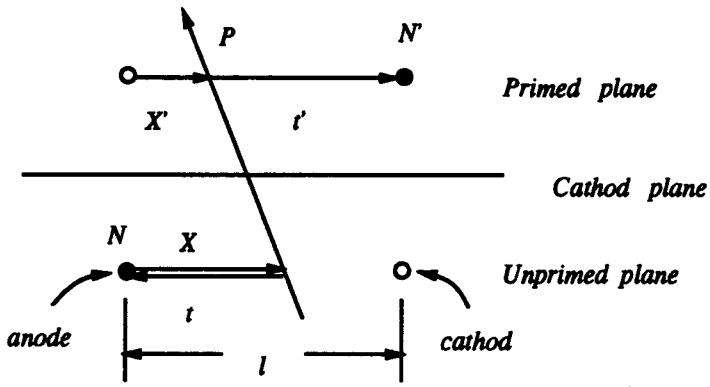

Figure 10. Illustration of FEC wire configuration

wire N and N' respectively which count the wires (in both planes separately) in the increasing direction of X coordinate, and *First* and *Last* are the first and the last of the total number of wires (in this case, 1 and 32 respectively). The FEC of the MRS achieves a spatial resolution of $<0.5mm$.

Vertical Drift Chambers (VDC)

A pair of Vertical Drift Chambers, VDC1 and VDC2, located just above the focal plane is the heart of the MRS detector system. It gives the coordinates of the particle trajectory–VDC intercepts, XA, YA for VDC1 and XB, YB for VDC2 which are used for the reconstruction of a), focal plane position XF and b), particle bend and non-bend plane trajectory angles θ and ϕ, see Chapter 5. The trajectory information is also used for the focal plane polarimeter collinearity tests as well as carbon scattering angle and vertex calculations, which we will discuss in Section 5.5.3.

VDC1 and VDC2 are 37 cm apart and set 45° to the optical axis parallel to the focal plane. Each VDC consists of two crossed wire planes, which give coordinates

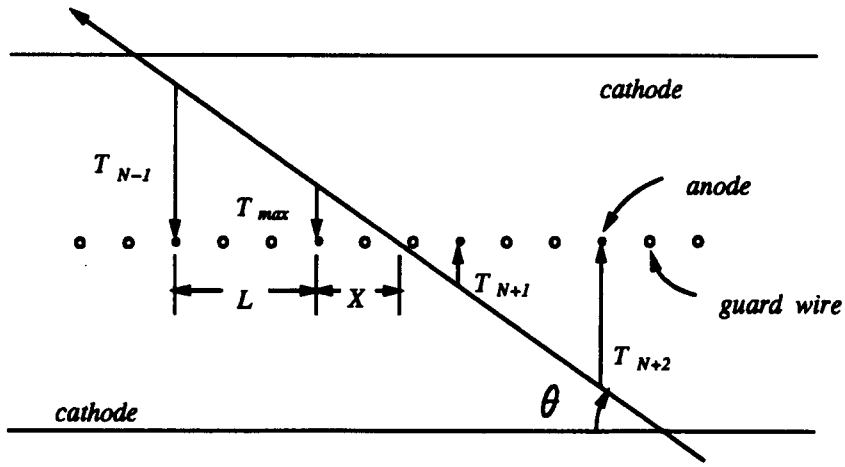

Figure 11. Illustration of a "hit" in a VDC drift chamber

in the x direction (X plane) and in the direction 30° to the x direction (U plane). The "X" direction here is the direction of the longer axis of the VDC frame pointing to the decreasing momentum direction in focal plane. The wire planes of VDC1 (X1, U1) and VDC2 (X2, U2) each contains 176 anode wires, and these wires are 6mm apart.

A valid hit needs at least 3 struck wires. From the geometry of Figure 11 it is straightforward to derive the particle coordinate with respect to the Nth anode wire

$$X = \frac{L}{2}\left(\frac{T_{N+1} - T_{min}}{T_{max} - T_{min}}\right), \tag{4.11}$$

and in the VDC coordinate system

$$X_{tot} = \frac{L}{2}\left(NL + \frac{T_{N+1} - T_{min}}{T_{max} - T_{min}}\right). \tag{4.12}$$

where $T_n = t_0 - t_n$ is the TDC time in common stop mode corresponding to the nth anode wire, and t_n is the drift time.

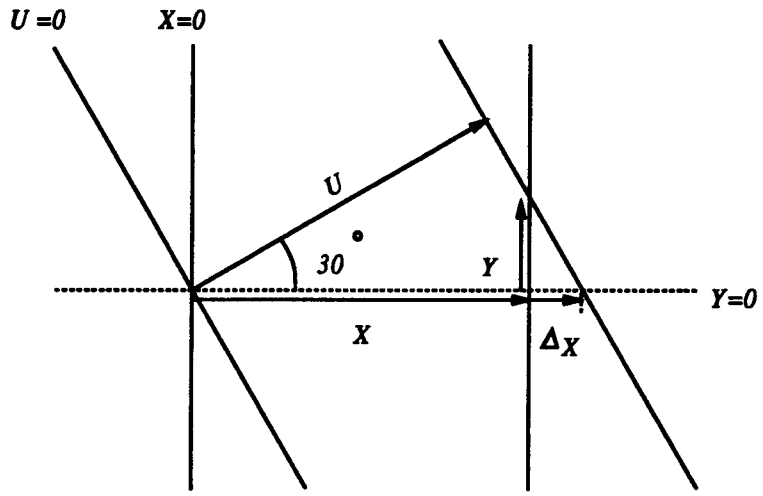

Figure 12. The relation between the coordinates X, U and Y.

With X and U coordinates, Y can be easily calculated (Figure 12) by[5]

$$Y = 2U - \sqrt{3}X. \tag{4.13}$$

However, since the X and U planes are not coincident in the z direction due to the small separation $XUSEP$ between them (Figure 13), a correction to X, $XCORR$ must be made,

$$XCORR = \frac{DX12 \times XUSEP}{VDCDIST}, \tag{4.14}$$

so $X - XCORR$, instead of X must be used in the Y calculation.

The motivation behind using *vertical drift* chambers at the MRS focal plane is now clear. More struck wires and their associated drift times are involved in a

[5]In data analysis, the positive Y direction of the MRS system was defined as the positive scattering angle direction, i.e. to the left of the beam line when looking downstream, which is the negative Y direction defined in Figure 12. The X direction is the decreasing momentum direction at the MRS focal plane.

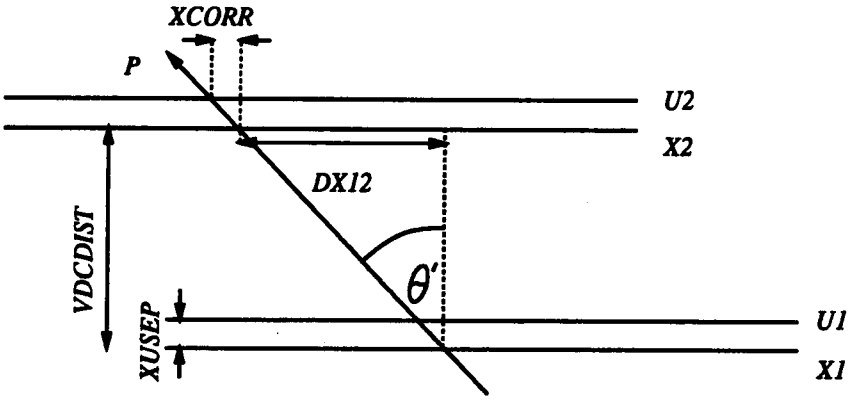

Figure 13. Illustration of a correction to coordinate X

vertical drift hit than in a horizontal drift. So a single drift has smaller influence in the coordinate calculation. In other words, the errors in the drift time tend to average out. Because a tilted wire plane (i.e. not perpendicular to optical axis) is longer in x dimension than that of a not tilted one, the inter-wire space may be made larger in the VDC wire planes, which increases the relative accuracy in wire positions when making the chambers. The above arguments also explain the reason of using a U instead of Y wire plane for the orthogonal coordinate dimension. A Y wire plane would clearly not provide at least 3 struck wires for each "hit", and it would be just like horizontal drifting. A Y plane would have fewer wires due to the shorter side of the wire plane in y dimension but at the expense of lengthy wires in the x dimension and problems associated with that.

Paddle Detectors

There are 10 plastic scintillator paddles (see Figure 2) lined up above the MRS focal plane in between the VDC's and the FPP. The paddle detectors cover the

entire focal plane area covered by VDC's, and they can be individually turned on and off, when used as part of MRS trigger, to restrict the momentum acceptance of the focal plane so as to select the interesting focal plane area and reduce the number of unwanted events.

4.6 Focal Plane Polarimeter (FPP)

The last but most important piece of experimental equipment is the Focal Plane Polarimeter. It provides the information (carbon scattering polar angle θ_c, azimuthal angle ϕ_c and analyzing power A_c) necessary for the calculation of the polarization at the focal plane. Four delay line horizontal drift chambers $D1, D2, D3$ and $D4$ are the main detectors, as shown in Figure 14, D1 is 80cm downstream from VDC1 and the same distance upstream of D4, while D2 is located in the middle of D1 and D4 with D3 downstream in the middle of D2 and D4. Each chamber has two orthogonal wire planes (Figure 15), and each wire plane consists of alternating anode and cathode wires, with anode-cathode spacing of 4 mm. Anode wires are connected to a common delay line. The cathode wires are alternately bussed together to form two (odd and even) cathode outputs. Four carbon slabs (4.5 cm, 3 × 3 cm) can be placed upstream just before D2. Two scintillator counters located just before the carbon slabs (S1) and at just after D4 (S2) are used to provide timing references for the chambers and detector trigger.

For each chamber plane, encoded signals are the TDC times for each end of delay line T_l and T_r, the cathode timing signal T_c, the ADC values of the two cathode signals E_{odd} and E_{even}. With this information the following expressions are generated [32]:

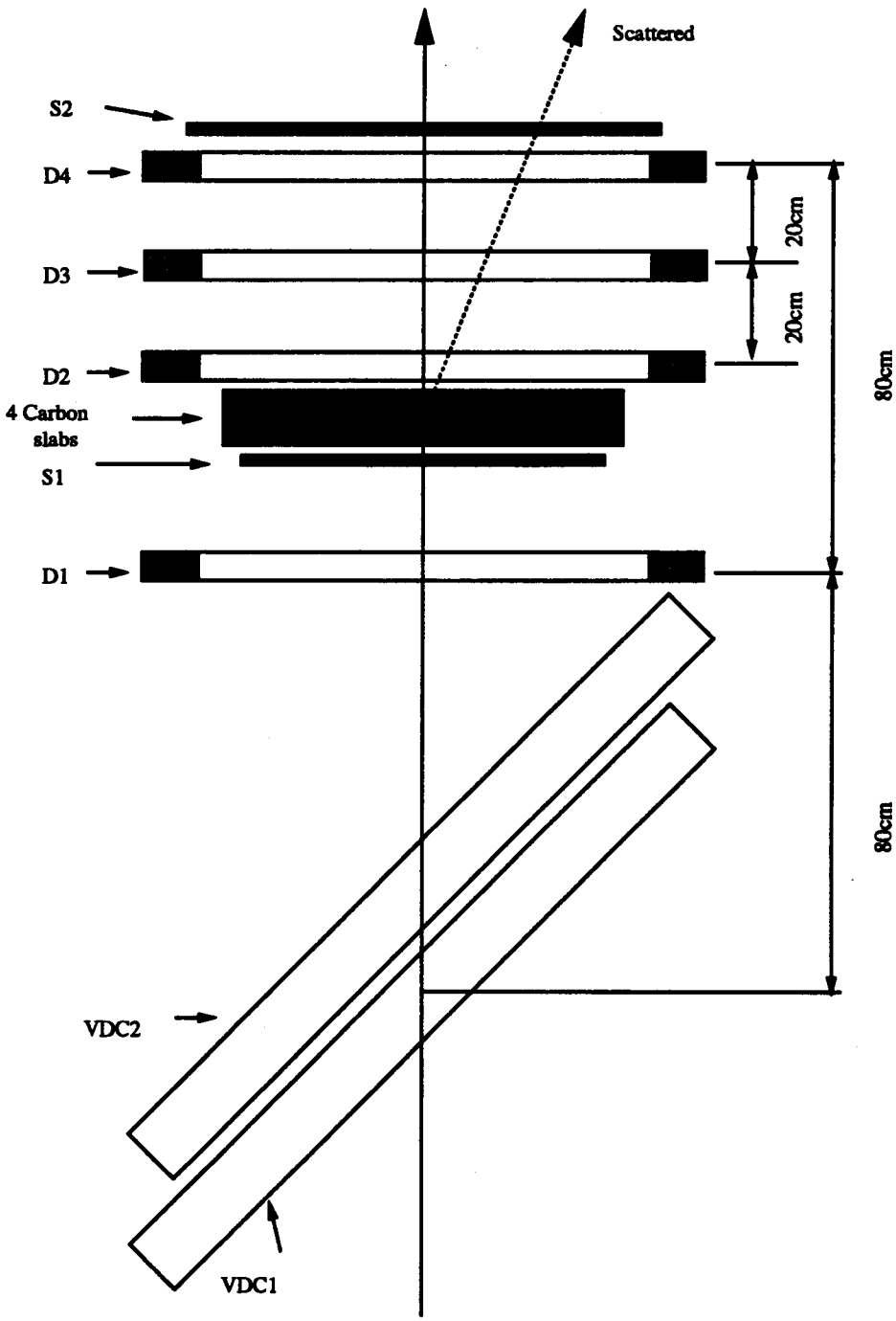

Figure 14. A schematic diagram of the Focal Plane Polarimeter

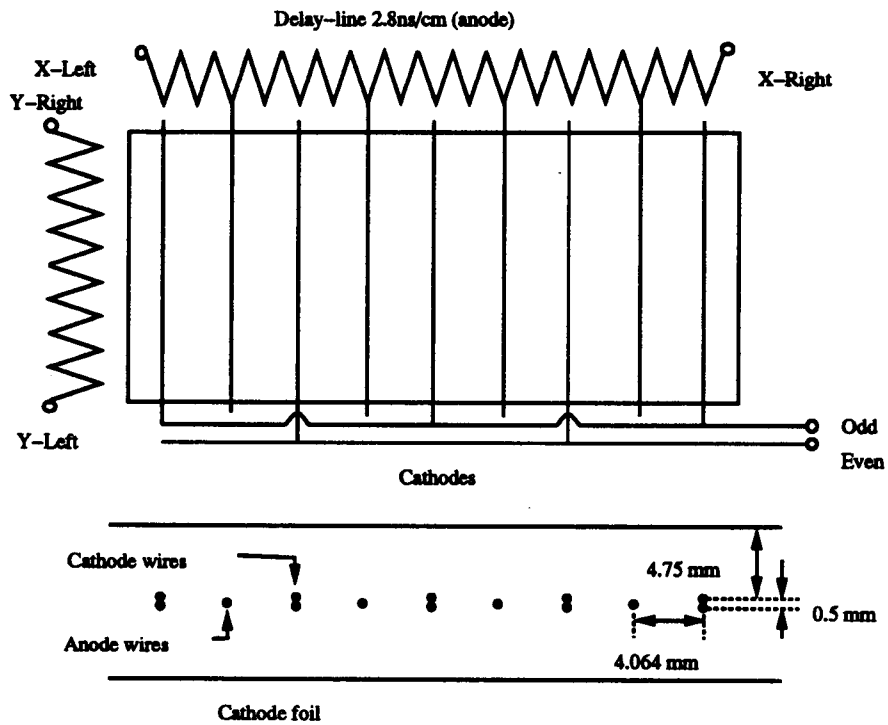

Figure 15. FPP wire plane diagram

The anode wire position

$$X = T_l - T_r; \tag{4.15}$$

The drift time from the anode timing

$$T_d = T_l + T_r = 2T_d + constant; \tag{4.16}$$

The drift time from the cathode timing

$$T'_d = T_c - (T_l - T_r)f; \tag{4.17}$$

A CHECKSUM spectrum

$$T_l + T_r - 2T'_d = 2(T_d - T'_d) + constant; \tag{4.18}$$

(i.e. T_d should be equal to T'_d) and normalized cathode difference spectrum

$$\frac{E_{odd} - E_{even}}{E_{odd} + E_{even}}. \tag{4.19}$$

4.7 Detector Readout and Data Stream

The MRS detector uses programmable LeCroy CAMAC modules which allow keyboard command to change the logic of some inputs. Figure 16 shows the MRS electronic logic diagram. A typical MRS event trigger requires a signal from the FEC (with a proper time delay) coincidences with signals from X1 of VDC, any one (or group) of the trigger paddles and, if FPP is in use, the S1 and/or S2 of the FPP.

FPP has a separate trigger system independent from MRS. Several tests are made for the FPP trigger by its microprocessor. Only those events passing the tests are treated as good events. The FPP data of a good event is stored in the

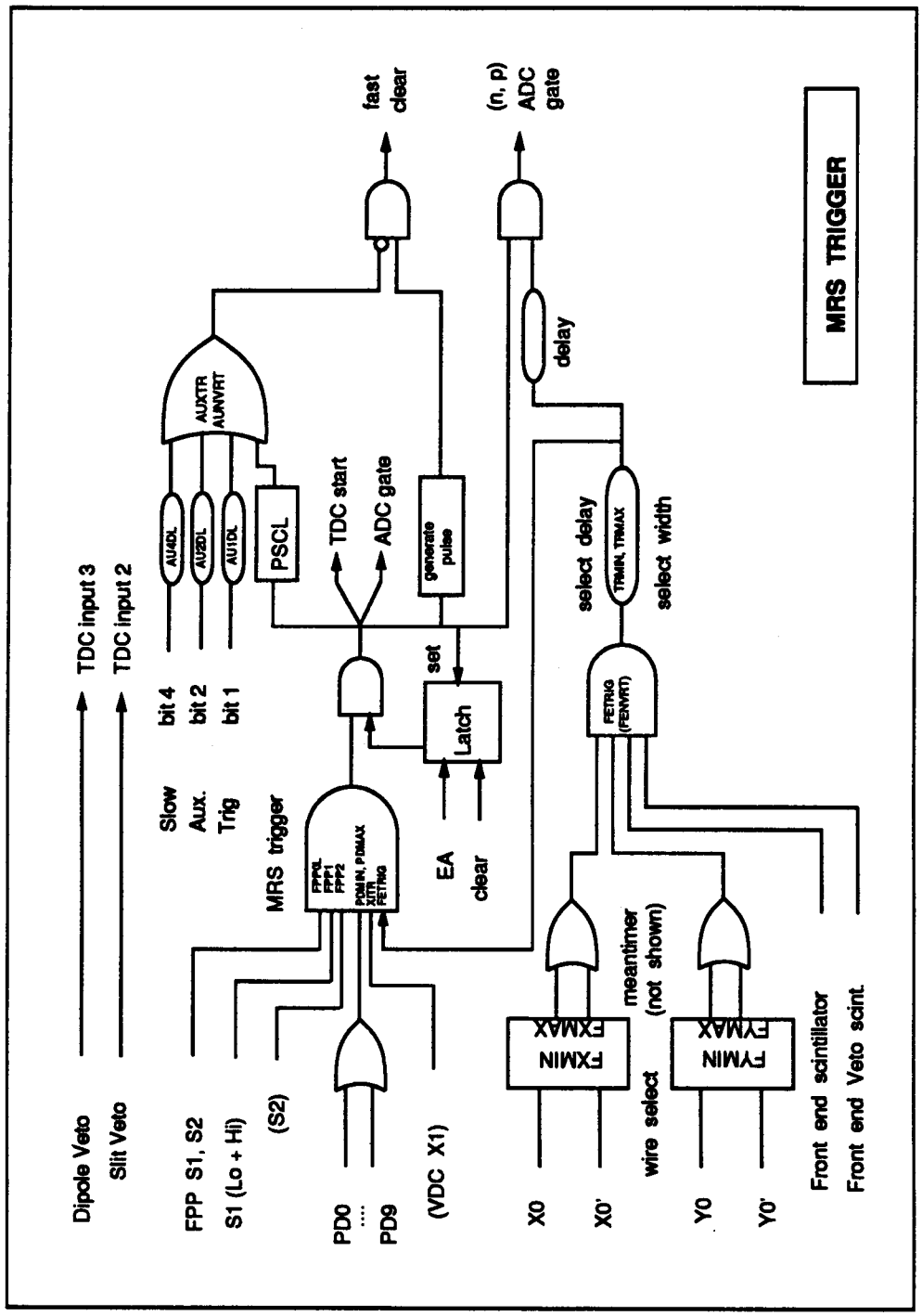

Figure 16. MRS event trigger logic

Starburst computer memory, then a LAM signal is issued by the Starburst and the MRS data acquisition computer reads this buffer along with standard spectrometer data. Not all the particles scattering from the carbon scatterer are useful. At small ($< 5°$) scattering angles, the proton-carbon analyzing power is virtually zero and thus make little contribution to the scattering asymmetry. In fact, less than 10% of the particles scattered in the FPP have a scattering angle large enough to be useful. So, a "small scattering angle" test is performed to limit the overhead of transferring and recording useless data. The criterion for this test is that the value of $dX = X1 - 2X2 + X4$ and $dY = Y1 - 2Y2 + Y4$ should be small (this should be obvious from the FPP geometry shown in Figure 14), Xn and Yn are the nth chamber coordinates. If the sum of the squares of the dX and dY is less than a required value which corresponds to $\sim 5°$ in scattering angle, the event is rejected. The second test is the CHECKSUM test on every chamber plane which excludes the "nearly coincident" (multi-track) events that cause the chamber output from one end of a delay line to be from one event and that of the other end to be from a different event. Finally, the pulser-generated events and software pre-scaled events are passed without any test. One use of the pre-scaled events, in our case, was for the FPP chamber collinearity adjustments, which we will discuss in Section 5.5.1.

The data acquisition computer reads the CAMAC ADC's and TDC's detector output information and writes the information onto magnetic tapes in a sequence specified by the user in a file written in TWOTRAN computer language. The data stream for a typical MRS event, also referred to as event type 2, consists of a fixed and a variable length portion, which take the following order: 1) 5 header words that describe the event length, type and sequence number, 2) 6 scintillator TDC signals including TTB, TRF, TSLT, TDIP, TSI, TAUX proceeded by a header word, 3) 12 scintillator ADC signals i.e. ESLT, EDIP, PD, PD1, ... PD9 and 4), when FPP is in use, 54 words of information from FPP ADC and TDC's, and

the variable length part, the VDC TDC's values proceeded by two header words. In the above names of the detector outputs, TTB is the TDC value started by (usually) the paddle scintillators (or S1, S2) and stopped by delayed FEC signal, which is related to the time of flight of the particle; SLT and DIP are the Slit and Dipole veto respectively, and PD's are the paddle detectors. Because the variable part length varies with events, making it *variable* can save computer time and data tape.

Also written on tape is scalar information which is referred to as Event Type 1. Scalar events include the information of number of charged particles passing the wire chambers, scintillator detectors, and the beam monitors, i.e. IBP and SEM. Unlike event type 2, the scalar event is recorded to tape every 5 seconds. So, the scalar information can be used to monitor the particle rates of detectors and beam; The IBP detector counts information is used for beam polarization calculation.

Chapter 5

Data Analysis

5.1 Data Replay

The data analysis of the experiment E482 was carried out on the TRIUMF VAX cluster and the MICROVAX II computer at Oregon State using the TRIUMF LISA data analysis package, a general purpose and completely interactive data analysis command environment designed to process large amount of event mode data.

For MRS experiments, as in our case, a wire chamber decoding routine DRIFT was first run by LISA to decode the FEC and VDC's chamber information to obtain the struck wires, corresponding drift times and the raw coordinates for the MRS chambers (FEC: $X0$ and $Y0$; VDC: XA, UA, XB and UB. The specific experiment dependent (secondary) coordinates and the necessary corrections were specified by the user in a user interface routine INSERT which LISA calls after the DRIFT routine. The secondary coordinates related to the MRS detectors are the non-bend and bend plane scattering angles ϕ and θ, the particle position at MRS focal plane XF, reconstructed particle position at target XI, YI, and the reconstructed y coordinates of the VDC's YA, YB. For the FPP chambers, the raw wire chamber positions were constructed in the routine INSERT as well as its

secondary coordinates θ_c, ϕ_c, the proton scattering angles, and $Z0$, the scattering vertex. Necessary corrections and tests for the coordinates were also performed in the INSERT routine, such as the momentum correction to θ and the *cone* test for the FPP events, etc. LISA provides means for the user to set gates on the coordinates. The gate conditions can be combined in logic expressions to form complex logic conditions. LISA allows users to define histograms (one or two-dimension) with coordinates (both raw and secondary) and with logic conditions. After INSERT, LISA evaluates the user specified conditions with the coordinates. LISA then runs the second user routine EVBEV which further processes the events. In our case, EVBEV incremented the FPP polarization asymmetry spectra. The final step in a LISA event loop increments the user defined histograms according to the values of the corresponding conditions. All the detector specifications necessary for the decoding and coordinates calculation are stored as parameters in the LISA parameter list, which can be used in all the executable routines.

In this chapter, we will discuss the construction of the secondary coordinates, some important corrections and tests made for some of the coordinates, determination of spin variables, and the treatments of the background.

5.2 MRS Secondary Coordinates and Corrections

In the user interface subroutine INSERT, a set of secondary variables was calculated using the raw event wire plane coordinates. This includes tracing back target positions XI and YI, reconstructing the bend plane and non-bend plane scattering angle θ and ϕ, and the focal plane position XF.

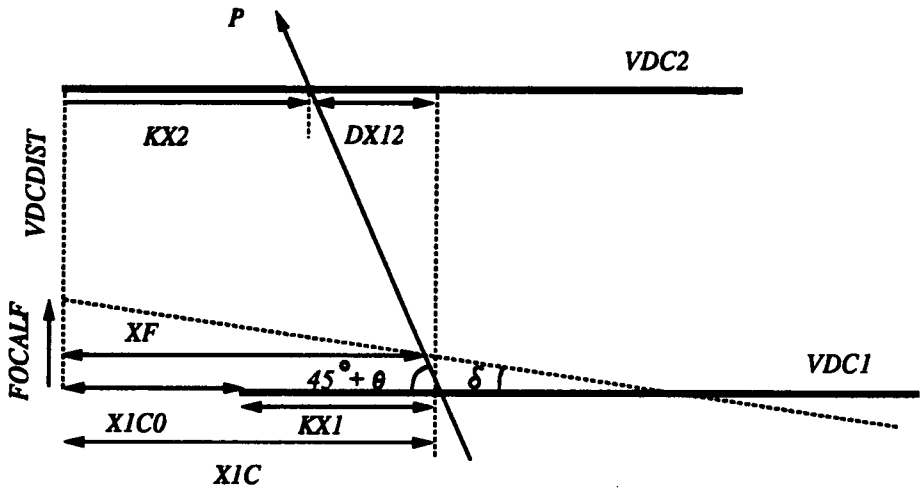

Figure 17. Illustration of the focal plane geometry

5.2.1 Coordinate Reconstruction

Focal Plane Coordinate, XF

The focal plane position of a particle is directly proportional to its momentum. Figure 17 illustrates the geometry of related variables at the focal plane, from which the following geometrical relations hold,

$$\frac{VDCDIST}{DX12} = \frac{Y_{traj}}{X1C - XF} \tag{5.1}$$

$$\tan\delta = \frac{FOCALF - Y_{traj}}{XF} \tag{5.2}$$

from which XF can be solved,

$$XF = \frac{(VDCDIST \times X1C) - (FOCALF \times DX12)}{VDCDIST - (DX12 \times \tan\delta)}. \tag{5.3}$$

In the case of MRS, $\delta = 0$.

Bend, Non-bend plane scattering angles θ, ϕ

The scattering angles θ and ϕ were defined as the angles between the particle trajectory and the MRS optical axis in the bend (dispersion) and non-bend (transverse) plane respectively at the focal plane. They were two of the degrees of freedom which affect the spectrometer momentum resolution and were determined with the VDC coordinates XA, YA, XB and YB.

Again, from Figure 17 the following is obvious,

$$\tan(45^\circ + \theta) = \frac{VDCDIST}{DX12} = \frac{1+\tan\theta}{1-\tan\theta}. \tag{5.4}$$

For small proton polar scattering angle, which is true for MRS, $tan(\theta) \rightarrow \theta$, then

$$\theta = \frac{\frac{VDCDIST}{DX12} - 1}{\frac{VDCDIST}{DX12} + 1}. \tag{5.5}$$

The non-bend plane scattering angle ϕ can be directly written as

$$\phi = \frac{Y2 - Y1}{\sqrt{(VDCDIST)^2 + (DX12)^2}}. \tag{5.6}$$

Target Coordinates, XI, YI

The target position of an event provided a direct mean to exclude events that did not come from the target; Like the scattering angles θ and ϕ, the target coordinates are important degrees of freedom that affect the momentum resolution. We reconstructed the target position coordinates from the FEC coordinates $X0$, $Y0$ and scattering angles θ, ϕ, as shown in Figure 18

$$XI = (X0 - \frac{L}{R_{22}}\theta_{pc})\frac{R_{22}}{R_{22} - LR_{21}}, \tag{5.7}$$

$$YI = (Y0 - \frac{L}{R_{44}}\phi)\frac{R_{44}}{R_{44} - LR_{43}}. \tag{5.8}$$

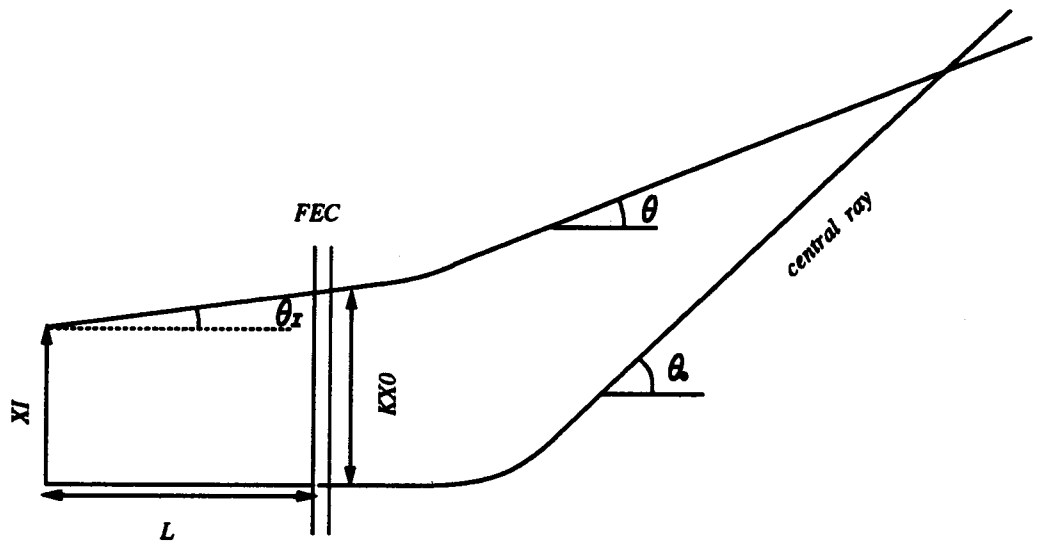

Figure 18. Target coordinates reconstruction

In deriving equation 5.7 the following beam optics was used,

$$\theta_{pc} = R_{21}XI + R_{22}\theta_I \tag{5.9}$$

$$\phi = R_{43}XI + R_{44}\phi_I, \tag{5.10}$$

where $R_{ij}, (i,j = 1,2,3,4)$ are transfer coefficients [30]. θ_{pc} is momentum corrected bend plane scattering angle (Section 5.2.2).

5.2.2 Momentum Correction

Because the MRS dipole disperses particles according to their momenta, the bend plane scattering angle θ of the particle is momentum dependent, and therefore it changes with focal plane position, See Figure 19.

In order to have the window condition on the θ coordinate gate consistent throughout the focal plane, it was desired to make θ momentum independent. This

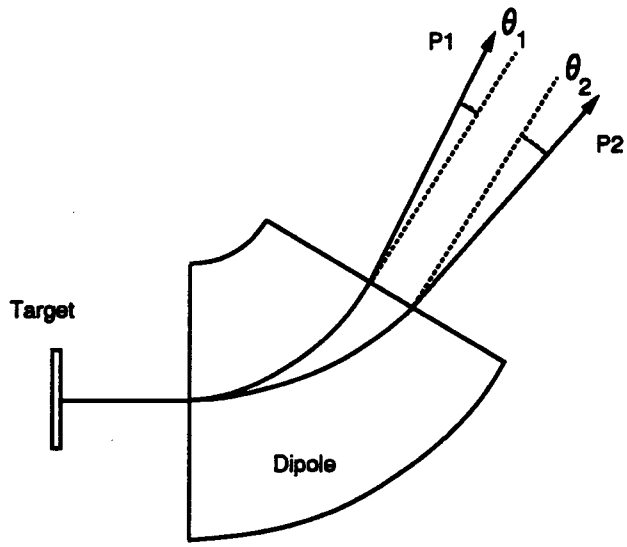

Figure 19. Bend plane scattering angle is momentum and focal plane position dependent

was achieved, to the first order, by a subtraction of a linear focal plane coordinate XF term from θ,

$$\theta_{pc} = \theta - K_{pc}(XF + X0). \tag{5.11}$$

The parameter K_{pc} was adjusted to obtain the best correction. Figure 20 shows the effect of the momentum correction to θ.

5.2.3 Aberration Correction

The focal plane coordinate of an ideal magnetic spectrometer depended only on the particle's momentum. So for instance, particles with the same momentum would focus on a single point at the focal plane regardless of their positions at the target where they originated and their scattering angles. If a histogram of any of these degrees of freedom verses the focal plane coordinate were drawn, particles with

same momentum would appear on a vertical straight line. However, in the case of a real spectrometer, there is always some dependence of other degrees of freedom in XF in addition to particle momentum. This worsens the resolution of the system and is called the magnetic aberration analogous to the image aberration of an imperfect optical lens system. The cause of this is due partially to the imperfectness of the magnet components (such as the material. etc.) of the spectrometer system and to particles passing through the inhomogeneous field regions of the magnet elements, such as the regions near the edges of dipole. In general, a particle's position at the MRS focal plane is a function of a all the geometrical coordinates associated with its trajectory in the spectrometer as well as its momentum, so the ideal aberration correction should be done as

$$XFK = XF + \sum_j \sum_i a_{ij} X_j^i + \text{crossterms} \tag{5.12}$$

with the coefficients a_{ij} adjusted until XFK was independent of all the geometrical coordinates, X_j $(j = 1, 2, ...)$ which includes the coordinates of the front end chamber $(X0, Y0)$, target (XI, YI) and the scattering angles in bend and non-bend plane (θ, ϕ). Usually, a correction of the order ≤ 4 would lead to a satisfactory result. In our case,

$$\begin{aligned} XFK &= XF + a_1 Y0 + a_2 Y0^2 + b_1 X0 + b_2 X0^2 + \\ &\quad c_1\theta_{pc} + c_2{\theta_{pc}}^2 + c_3{\theta_{pc}}^3 + c_4{\theta_{pc}}^4 + d_{11}\theta\phi + e_1 XI. \end{aligned} \tag{5.13}$$

The highest order correction to the bend plane scattering angle θ_{pc} reflected the fact that the inhomogeneity of the dipole field over a large area played an important role in the aberration, since this degree of freedom was most influenced by the dipole magnetic field. The parameter of each coordinate was adjusted while inspecting the two dimensional spectrum of the selected variable verses XFK until the ultimate correction was reached. A small amount of high order residual

aberration at the tails of the variable spectrum of some coordinates was gated out by a properly chosen window condition. The histograms shown in Figure 21 are after a 4th order aberration correction to θ_{pc}. The higher order aberration effect at the lower and higher ends of the θ_{pc} was eliminated by setting gate on the coordinate, shown as the horizontal lines.

5.2.4 Kinematic Correction

The momentum of a scattered proton is dependent of its entry vertical coordinates at the FEC ($Y0$), and the width of the momentum distribution depends on the reaction kinematics (i.e. beam energy, scattering angle and the target type). If one plots the two dimensional histograms of $Y0$ versus focal plane position XF for p-d and p-C scattering, for instance, the protons scattered from deuteron and those scattered from carbon will show as two straight event bands with different slopes (having different momenta widths), as shown in Figure 22.

To obtain ultimate resolution at the focal plane of a particular reaction, a particular correction has to be made, which was basically a rotation to the interested events band to make it vertical. This was done by adding a linear $Y0$ term $-S \times Y0$ to XF, with $\frac{dXF}{dY0} = S$.

5.3 Events Identification

The protons were identified with their locations on the two dimensional histogram SPID which was formed by the proton time of flight TTB between the FEC and the trigger scintillator S_2 and its energy lost in S_2 ESUM. Figure 23 shows a typical ESUM, TTB, SPID histogram and the associated gate for proton identification.

An accepted event must be first identified as a proton. It must also be within

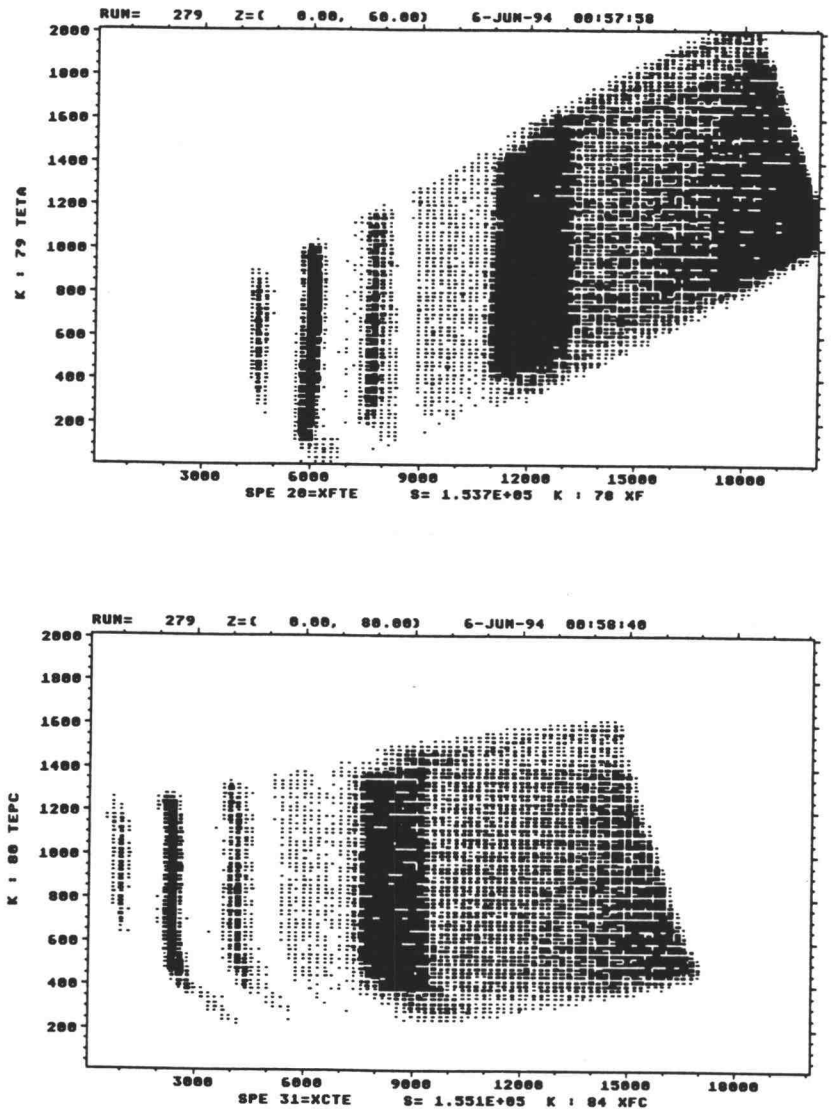

Figure 20. Effect of θ momentum correction: Top — the events distribution over the 2-D area of TETA(θ)×XF, before momentum correction to θ. Bottom — TEPC(θ_{pc}) is θ after correction, and XFC is the focal plane coordinate after kinematic correction for carbon.

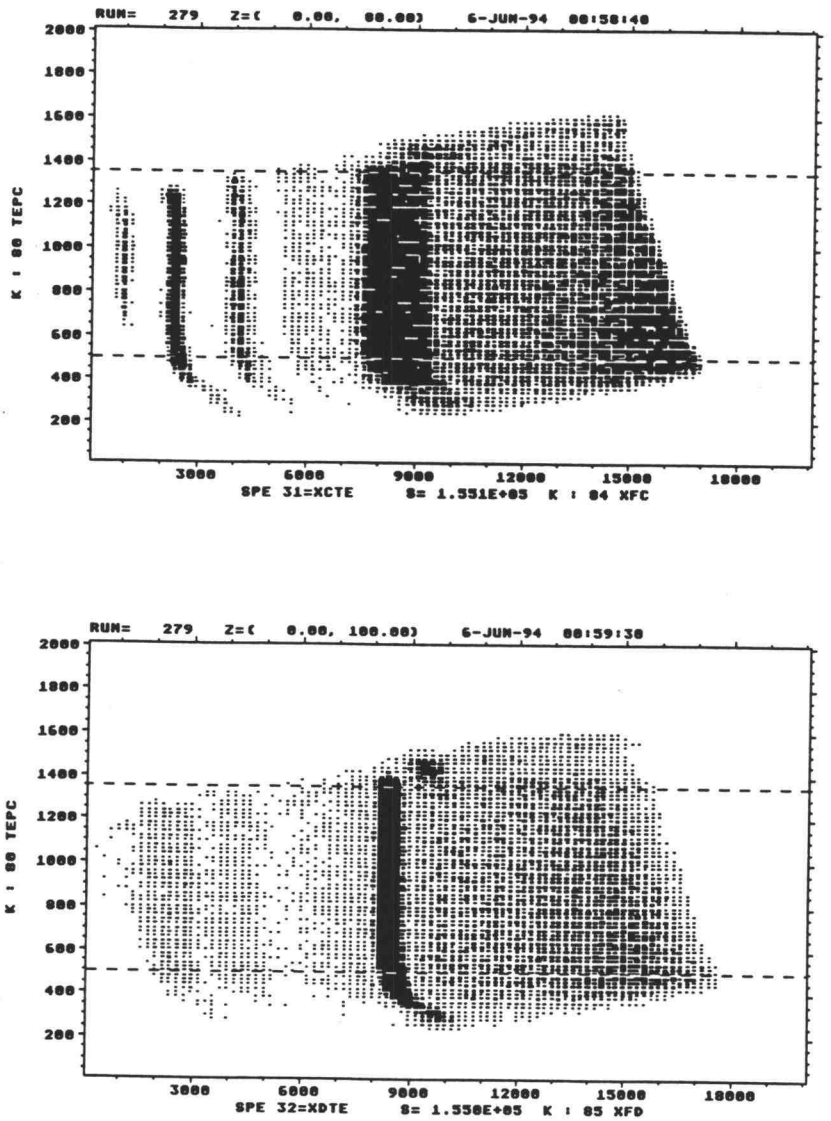

Figure 21. Effect of θ aberration correction: Both histograms have momentum corrected θ (or θ_{pc}, (TEPC)) as vertical axis; The horizontal axis is the focal plane coordinate after kinematic correction for: Top — carbon (XFC), Bottom — deuteron (XFD). The dashed horizontal lines show the gates set on θ_{pc}.

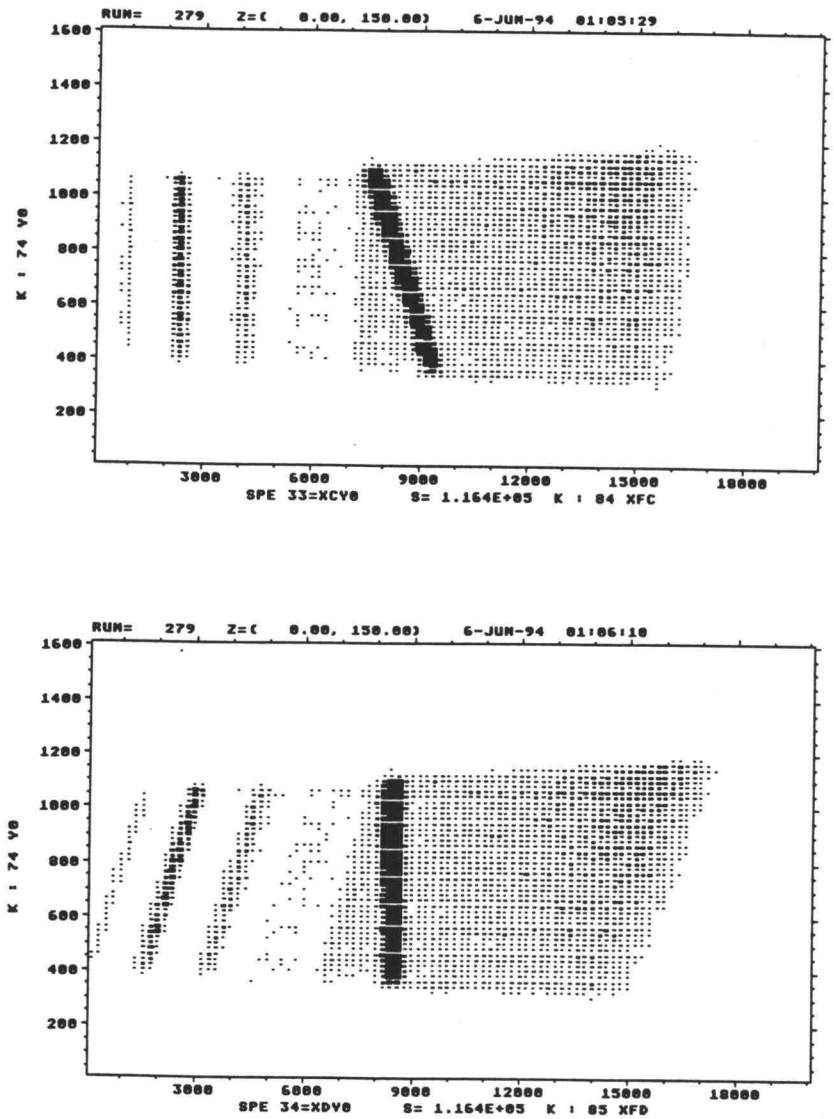

Figure 22. Effect of kinematic correction: Both histograms have the vertical coordinate $Y0$ of the FEC as vertical axis; The horizontal axis is the focal plane coordinate after kinematic correction for: Top — carbon (XFC), Bottom — deuteron (XFD).

the windows of the FEC ($X0 \times Y0$), target ($XI \times YI$) and bend and non-bend plane scattering angle ($TEPC(\theta_{pc}) \times PHI(\phi)$). Figure 24, 25 and 26 show the typical windows set on the coordinates $X0$, $Y0$, XI, YI, θ_{pc} and ϕ. The deuteron kinematic corrected focal plane distributions of the accepted events for 400 and 290 MeV incident proton energies at the proposed scattering angles are shown in Figure 27 through 33. The windows shown in the histograms were for p-d events selections. The background in the peak region consists mainly of proton-carbon scattering and some proton-deuteron inelastic scattering (break-up) in the lower momentum region. The p-d elastic scattering event count N_d was obtained by subtracting the background count N_b from the total count N_{tot} in the elastic p-d region, $N_d = N_{tot} - N_b$.

5.4 Proton-Deuteron Analyzing Power

The conservation of parity implies that only *normal* component of the analyzing power can be non-zero (Section 3.2.2), therefore, proton beam of normal polarization was used for the measurement of p-d analyzing power. The polarities of the beam, spin up, down and off, was switched in an approximate sequence 3, 3 and 1 minutes, respectively.

Applying up and down beam polarization polarities $P\uparrow$ and $P\downarrow$ to the equation 3.10, we obtained two independent expressions for the opposite beam polarization polarities:

$$I_\uparrow = I_o(1 + P_{N\uparrow}A_N), \tag{5.14}$$

$$I_\downarrow = I_o(1 - P_{N\downarrow}A_N), \tag{5.15}$$

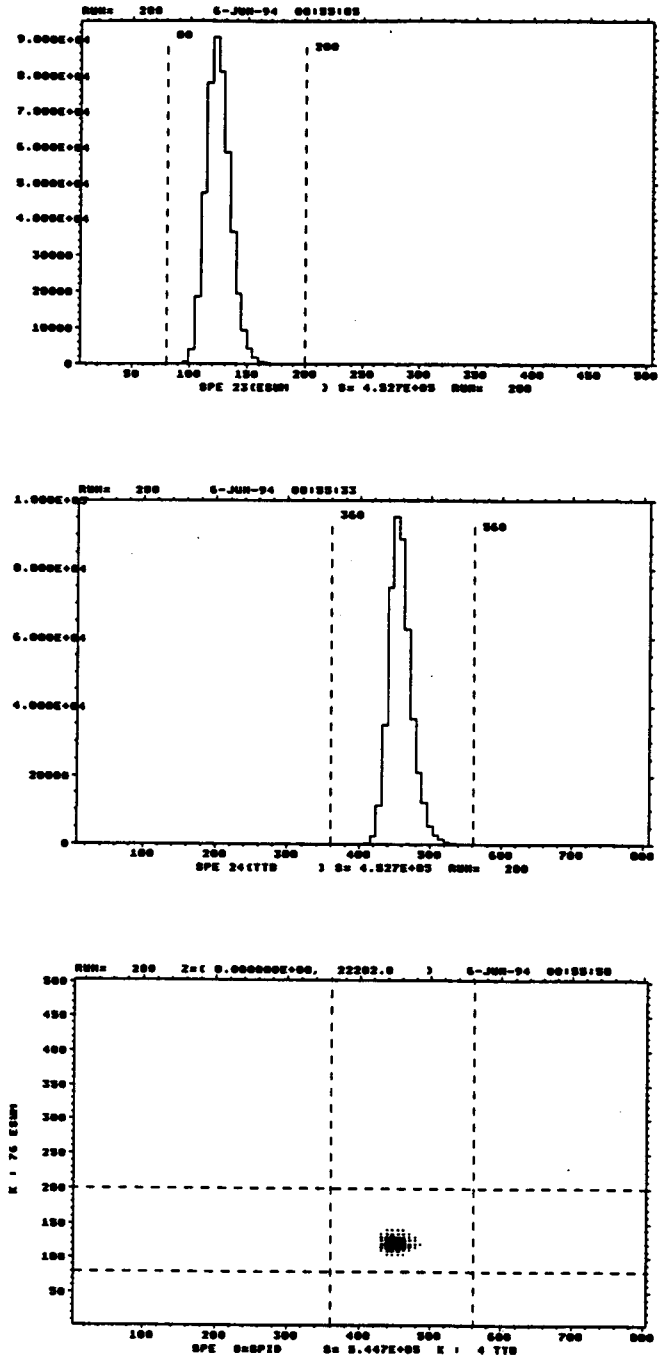

Figure 23. Proton identification: Top — proton energy lost in trigger scintillator (ESUM); Middle — histogram of a typical Time of flight (TTB); Bottom — TTB×ESUM (SPID). Particles inside of windows (dashed lines) in SPID were accepted as protons.

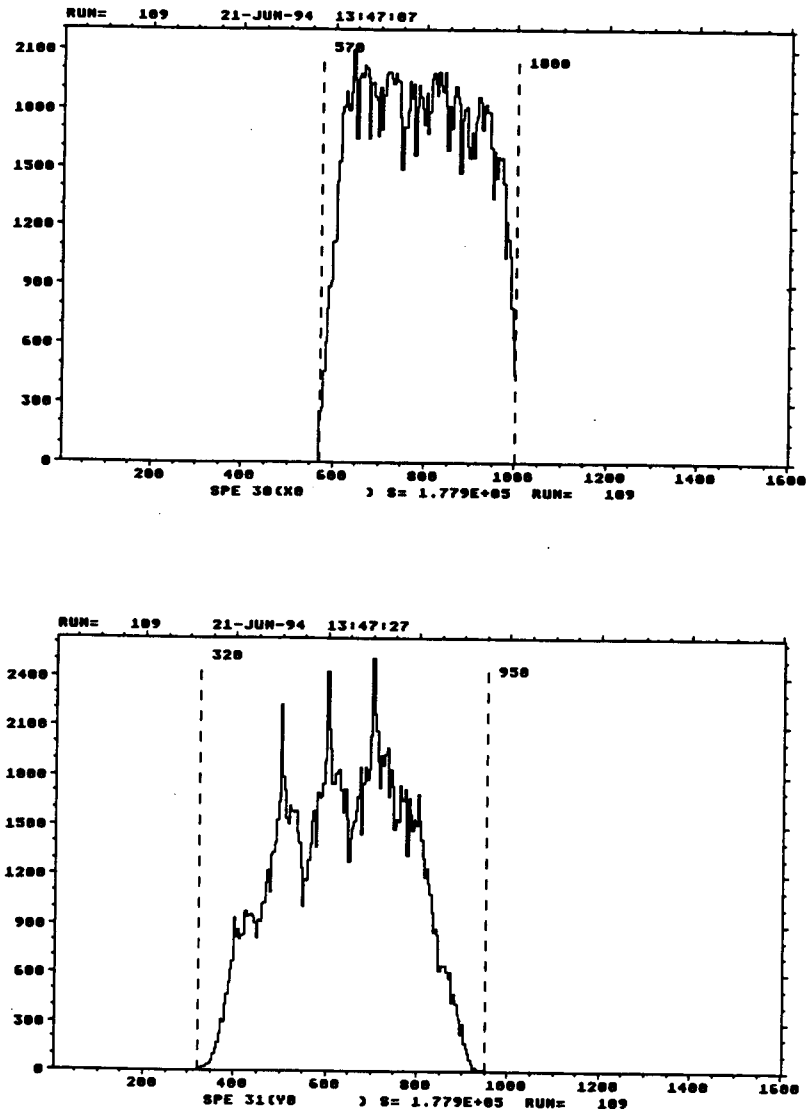

Figure 24. Typical FEC windows: Top — $X0$; Bottom — $Y0$. Windows are shown by the dashed lines.

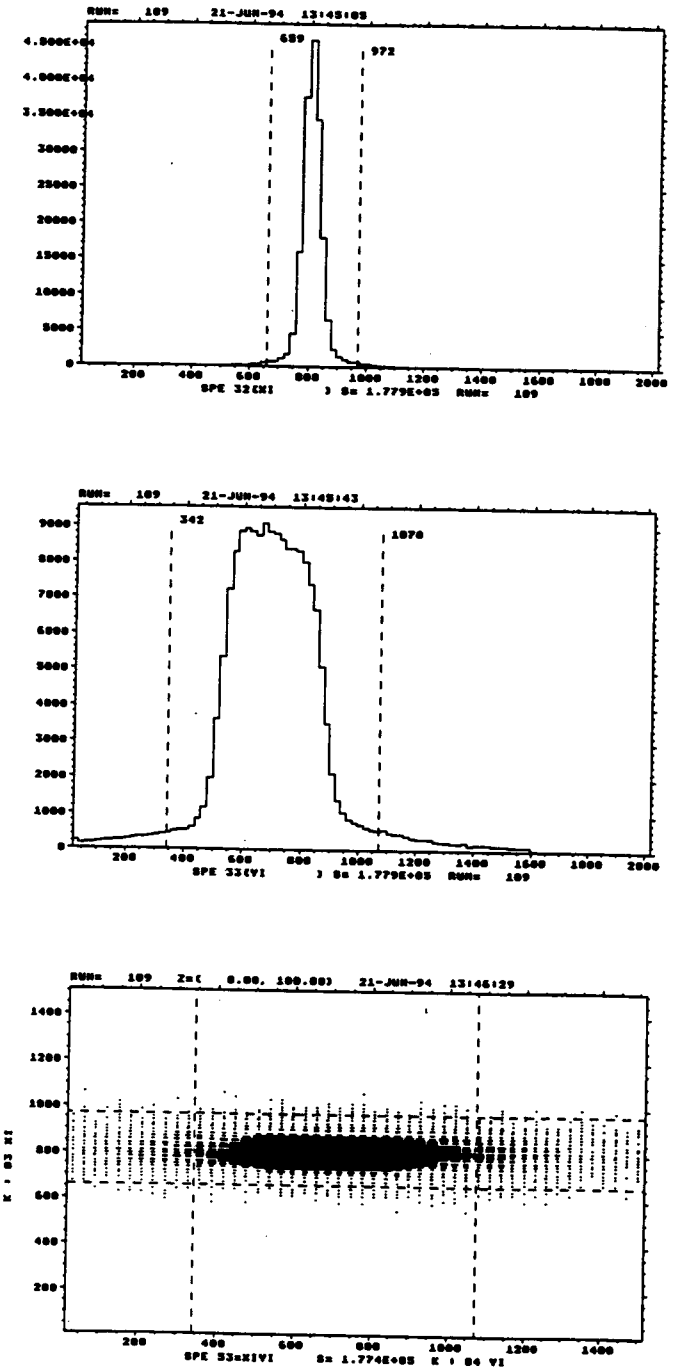

Figure 25. Typical target windows: Top — XI; Middle — YI; Bottom — $XI \times YI$. Windows are shown by the dashed lines.

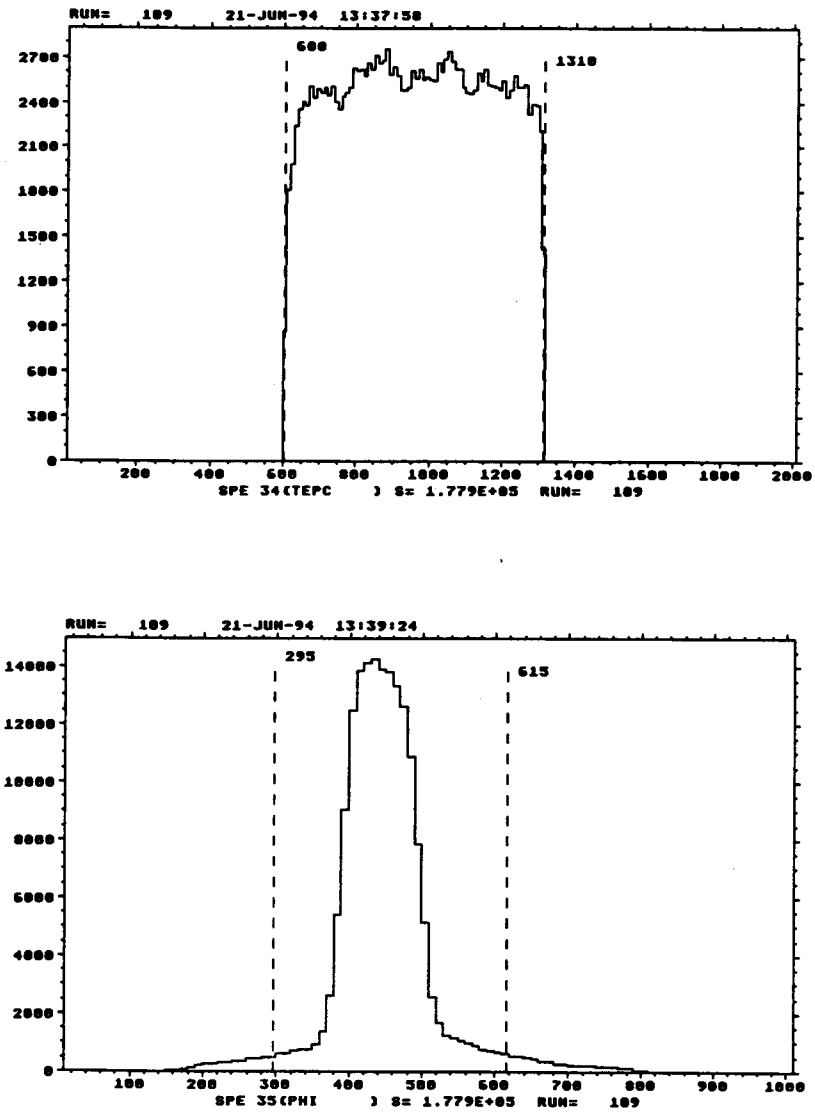

Figure 26. Typical scattering angle windows: Top — TEPC (θ_{pc}); Bottom — PHI (ϕ). Windows are shown by the dashed lines.

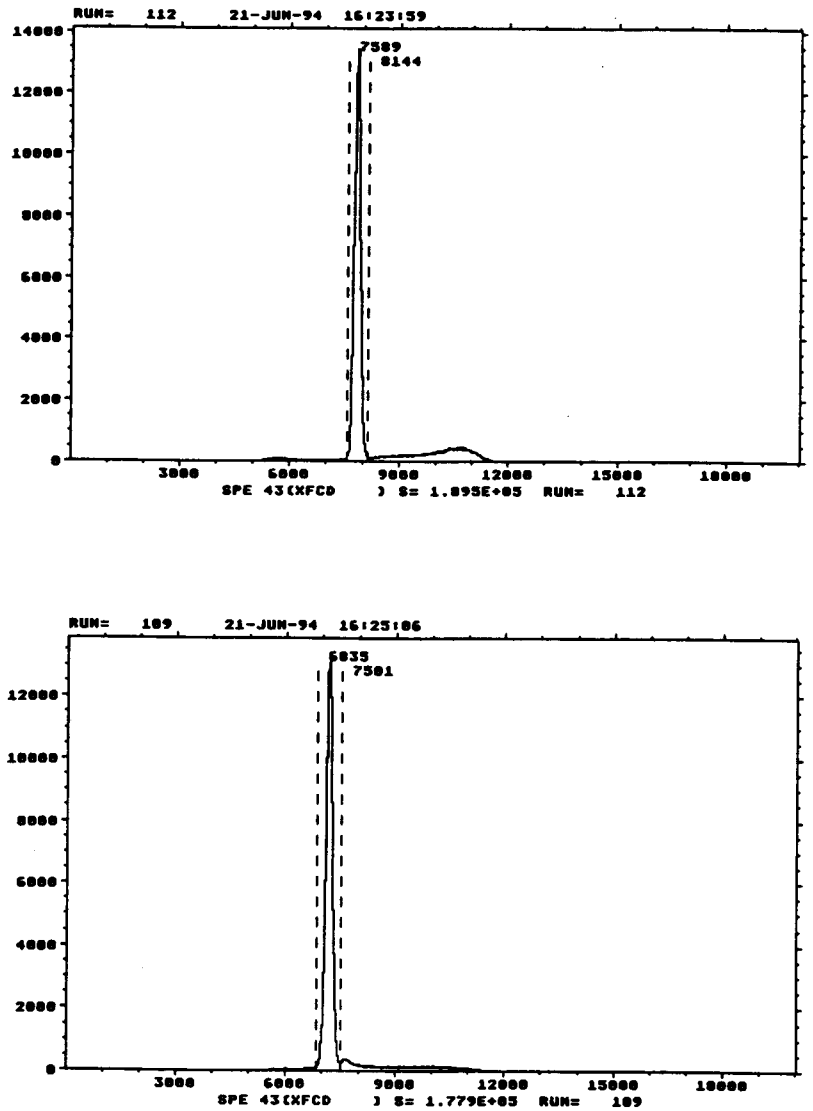

Figure 27. The focal plane distribution of the MRS accepted events (T_p=400 MeV): Top — $\theta_{MRS} = 20°$; Bottom — $\theta_{MRS} = 30°$.

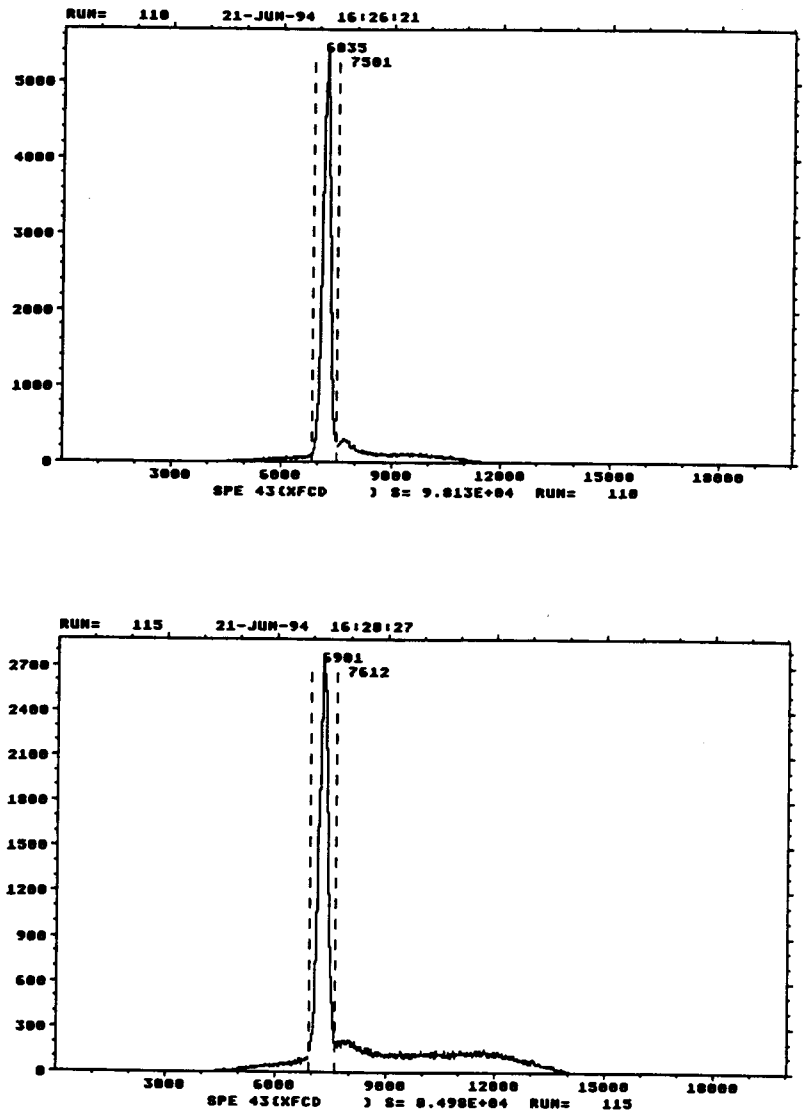

Figure 28. The focal plane distribution of the MRS accepted events (T_p=400 MeV): Top — $\theta_{MRS} = 40°$; Bottom — $\theta_{MRS} = 50°$.

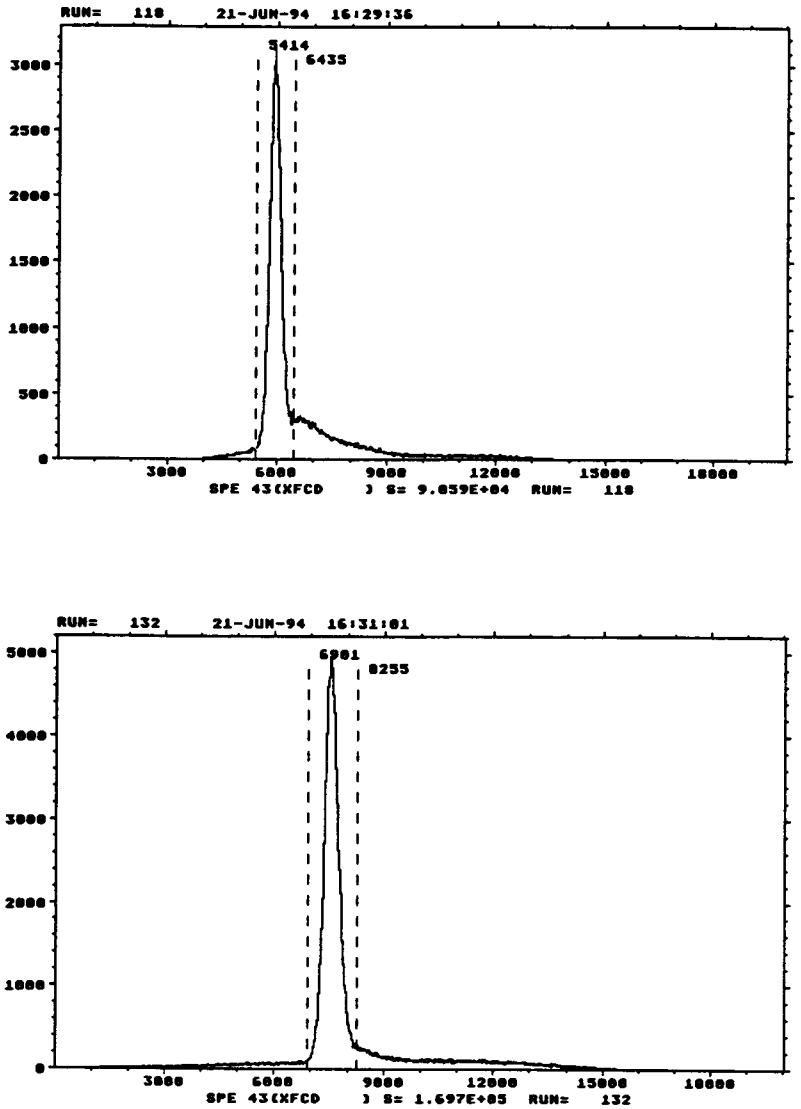

Figure 29. The focal plane distribution of the MRS accepted events (T_p=400 MeV): Top — $\theta_{MRS} = 60°$; Bottom — $\theta_{MRS} = 70°$.

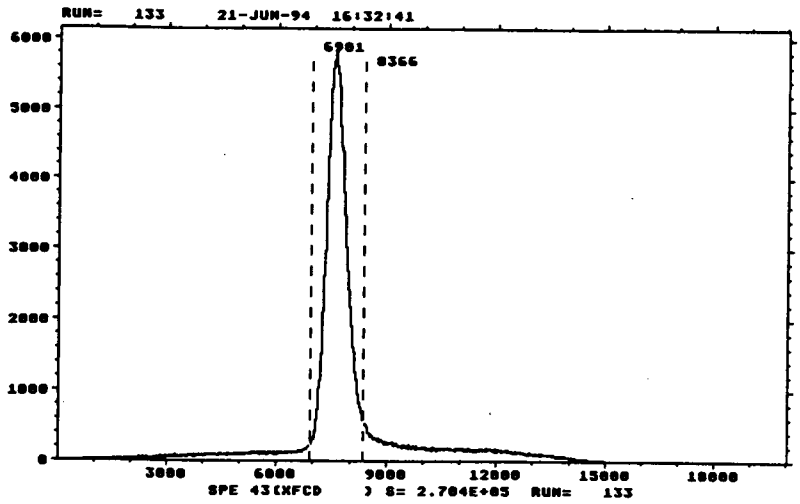

Figure 30. The focal plane distribution of the MRS accepted events (T_p=400 MeV): $\theta_{MRS} = 80°$.

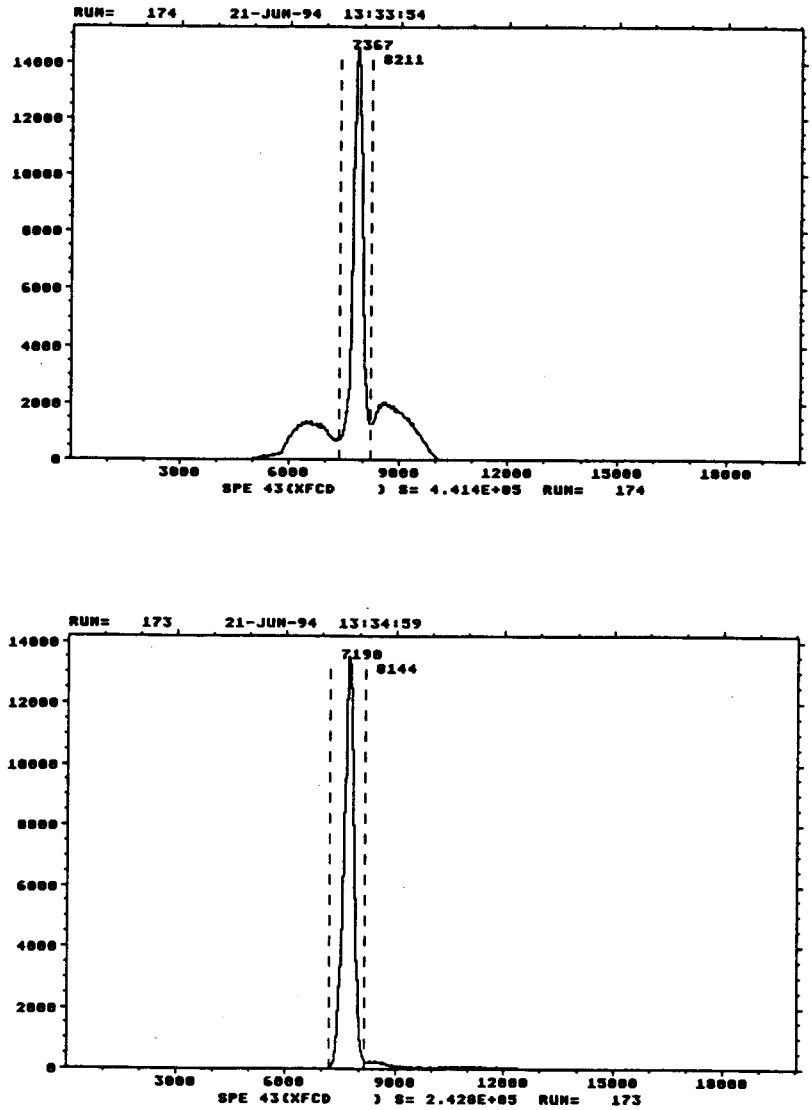

Figure 31. The focal plane distribution of the MRS accepted events (T_p=290 MeV): Top — $\theta_{MRS} = 20°$; Bottom — $\theta_{MRS} = 30°$.

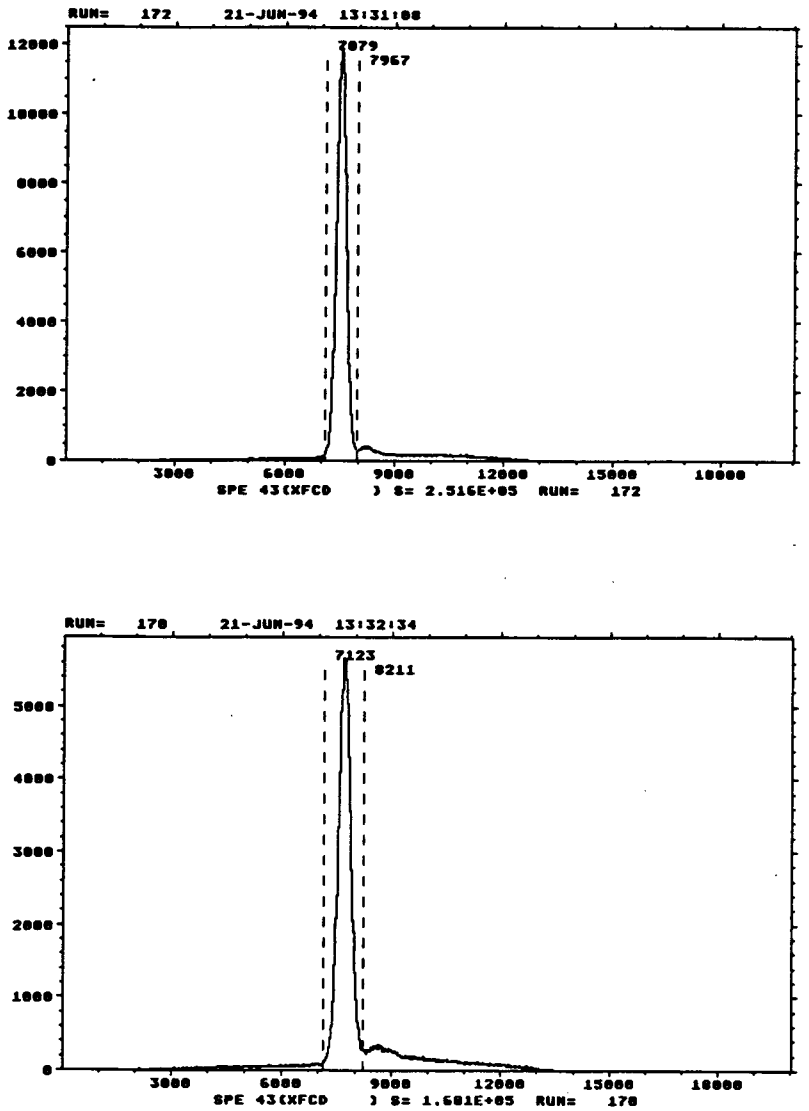

Figure 32. The focal plane distribution of the MRS accepted events: T_p=290 MeV): Top — $\theta_{MRS} = 40°$; Bottom — $\theta_{MRS} = 50°$.

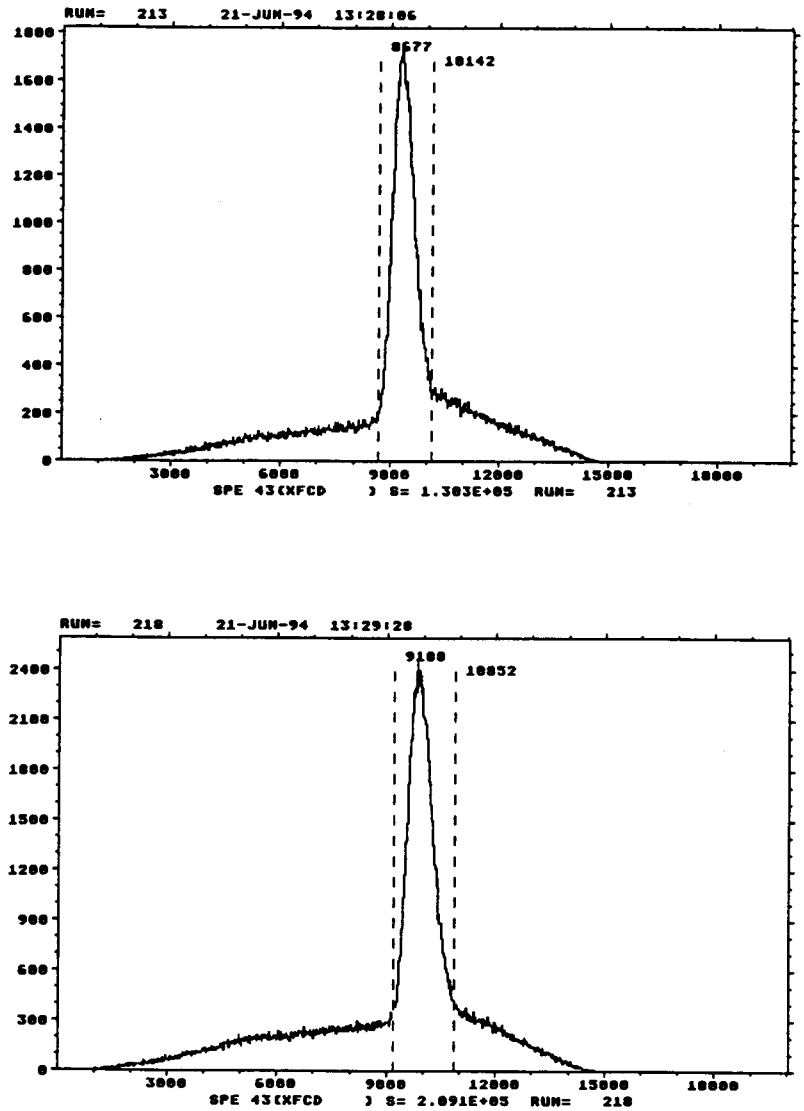

Figure 33. The focal plane distribution of the MRS accepted events: T_p=290 MeV): Top — $\theta_{MRS} = 70°$; Bottom — $\theta_{MRS} = 80°$.

from which A_N can be solved,

$$A_N = \frac{I_\uparrow - I_\downarrow}{(P_{N\uparrow} + P_{N\downarrow})[(I_\uparrow + I_\downarrow) - \frac{P_{N\uparrow} - P_{N\downarrow}}{P_{N\uparrow} + P_{N\downarrow}}(I_\uparrow - I_\downarrow)]}. \tag{5.16}$$

The cross section $I_{\uparrow\downarrow}$ is related to the events count $N_{d\uparrow\downarrow}$ by

$$I_{\uparrow\downarrow} = \frac{N_{d\uparrow\downarrow}}{\epsilon \tau n_t n_b}, \tag{5.17}$$

where ϵ is the probability of a particle traversing MRS and being detected (detector efficiency), τ is the detector system available time per unit time (detector live-time), n_t is the number of target scatterers per unit area (constant) and n_b is the beam particle number flux intensity at the target. $N_{d\uparrow(\downarrow)}$ is the p-d elastic scattering events count with $\text{spin}_{\uparrow(\downarrow)}$ beam polarization polarity conditions, which was obtained from the integral of the events count over the p-d elastic region ($\text{N}_{tot\uparrow(\downarrow)}$) of the focal plane distribution of $\text{spin}_{\uparrow(\downarrow)}$ polarity less background count ($\text{N}_{b\uparrow(\downarrow)}$).

The statistic errors of the analyzing power ($\delta A_{N stat}$) were resulted from that of the beam polarization ($\delta P_{N\uparrow(\downarrow)}$) and the p-d elastic events count $\delta N_{d\uparrow(\downarrow)}$. The uncertainties in determination of the background count was the main contribution to the non-statistic error ($\delta A_{N syst}$), see Appendix A.

5.5 FPP Coordinates and Tests

5.5.1 Wire Chamber Linearity Check

To ensure the accurate determination of the scattered proton angles (θ_c, ϕ_c) at the carbon scatterer in the focal plane polarimeter, it is important to properly line up the FPP wire chambers' physical coordinate systems along the the optical axis of the MRS and VDC system.

"Straight through" runs were made for this purpose in which the carbon scatterer was not used so that the protons from MRS passed straight through the FPP. To describe the particle track position at the wire chambers, the Cartesian coordinate system for the FPP was defined as: the z direction being along the optical axis of the FPP, x being in both the MRS bend plane and chamber central plane pointing to decreasing momentum direction at the focal plane, and the y being the increasing MRS angle direction (i.e. pointing to the left of the incident beam momentum direction). The origin of the FPP z coordinate is chosen to be at the vertex of optical axis crossing the central plane of the first FPP chamber, D1. Then (X_i, Y_i, Z_i) $(i = 1, 2, 3, 4)$ is the coordinates of the vertex of the particle track crossing the central plane of the ith chamber. The coordinate system for VDC1 (VDC2) was defined as: x being in both the chamber central plane and MRS bend plane pointing to the decreasing momentum direction, y being the same direction as that of the FPP system. The coordinates XA, YA (XB, YB) describe the vertex of the proton track crossing VDC1 (VDC2) central plane.

With the particle tracks and wire chamber intercept coordinates represented in the above coordinate systems, the event distributions for the following test variables were formed for the alignment propose,

$$X234 = X4 - 2X3 + X2 \tag{5.18}$$

$$Y234 = Y4 - 2Y3 + Y2 \tag{5.19}$$

$$X123 = X3 - 1.5X2 + 0.5X1 \tag{5.20}$$

$$Y123 = Y3 - 1.5Y2 + 0.5Y1 \tag{5.21}$$

$$X124 = X4 - 2X2 + X1 \tag{5.22}$$

$$Y124 = Y4 - 2Y2 + Y1 \tag{5.23}$$

$$XAB1 = (XB - XA) - (ZA - ZB)\frac{X1 - XA}{ZA} \tag{5.24}$$

$$YAB1 = (YB - YA) - (ZA - ZB)\frac{Y1 - YA}{ZA} \quad (5.25)$$

$$XA14 = (X1 - XA) - (-ZA)\frac{X4 - X1}{Z4 - Z1} \quad (5.26)$$

$$YA14 = (Y1 - YA) - (-ZA)\frac{Y4 - Y1}{Z4 - Z1}. \quad (5.27)$$

From the the FPP dimension layout shown in Figure 14 it is obvious that if all the chambers were perfectly aligned with the optical axis, the above test variables would all vanish, i.e. the corresponding spectra would appear as a sharp spike (limited by the wire chamber spatial resolution) at zero. The misalignment were corrected by adjusting the offset values of individual coordinates in a trial-and-error manner.

With the carbon slab(s) in place, the check variables involving chambers both up and downstream of the scatterer ($X123$, $X124$, $XA14$, $Y123$, $Y124$ and $YA14$) would no longer have sharp peaks at zero because the scattering of the protons by the carbon nuclei. However for good events the $X234, Y234, XAB1$ and $YAB1$ should still be peaked at zero. Events caused by accidentals and/or scatterings by chamber wires were usually far off zero. These multiple track events were rejected by properly gating the spectra. Figures 34 through 38 show typical alignment histograms (offset=200) defined by Equations 5.18 through 5.27 using "straight-through" data. The misalignment was controlled to be within 0.05°, which could introduce a relative systematic error of ≤ 0.01 to the polarization measurement.

An alternative method to check and adjust the alignments was to use the pre-scaled events which did not undergo small θ_c exclusion test. Although the pre-scaled events did pass through the carbon scatterer, small scattering angle events dominated their population. This method provided a practical way to check FPP chamber alignment for data taking runs.

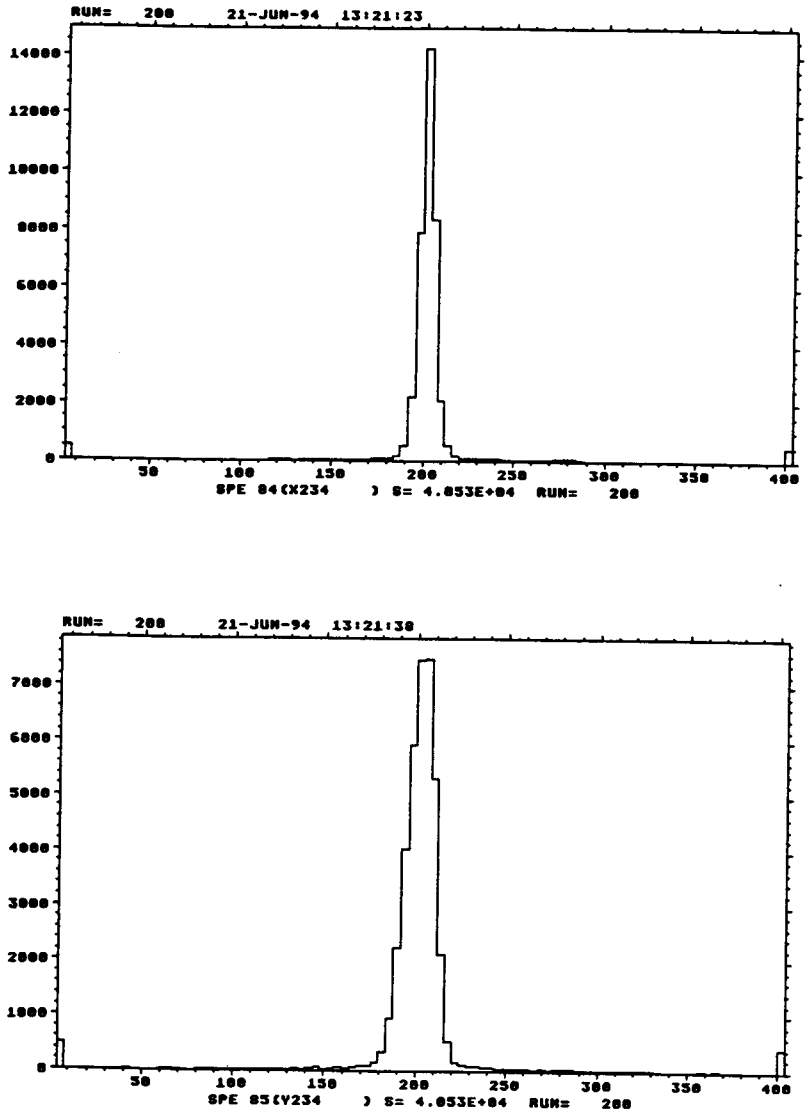

Figure 34. Typical FPP alignment (unit=0.01 mm): Top — X234; Bottom — Y234.

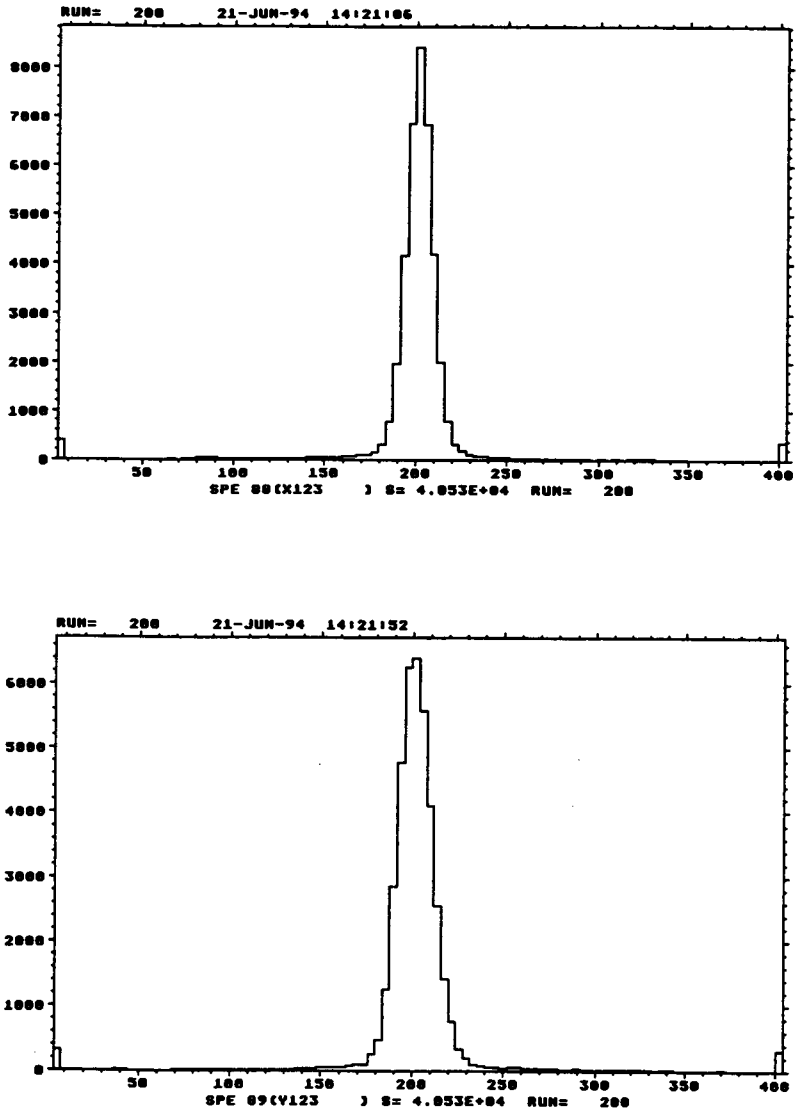

Figure 35. Typical FPP alignment (unit=0.01 mm): Top — X123; Bottom — Y123.

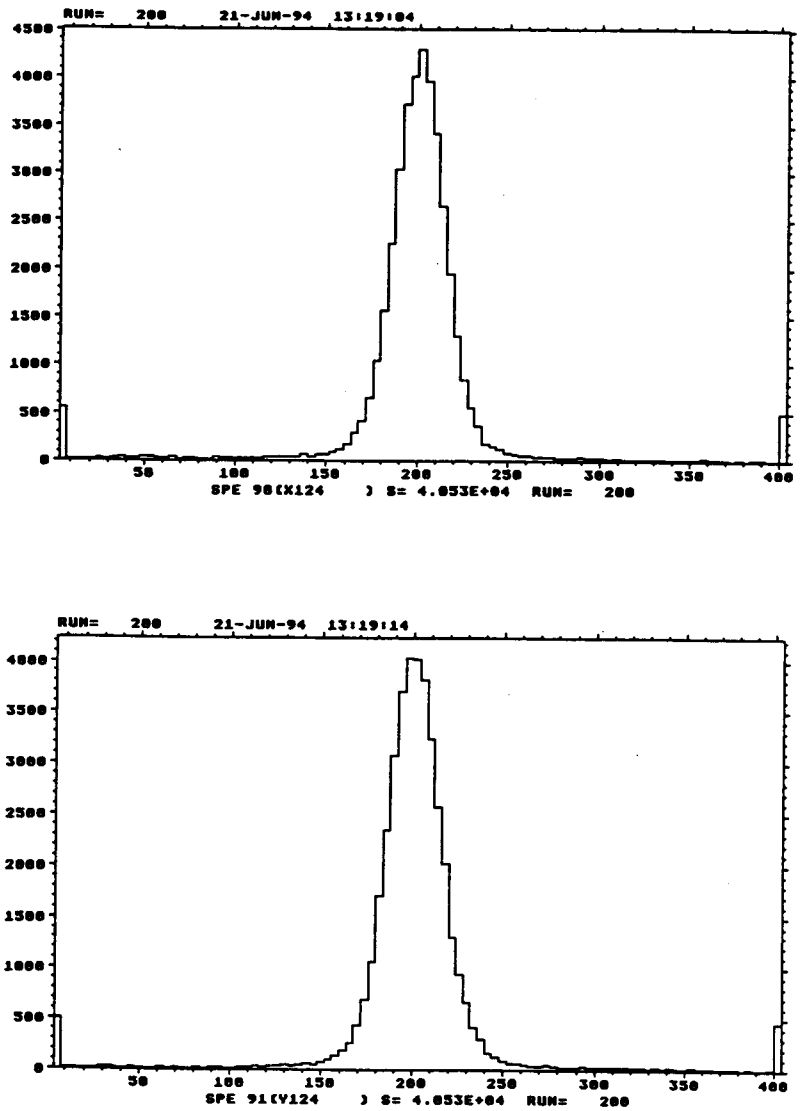

Figure 36. Typical FPP alignment (unit=0.01 mm): Top — X124; Bottom — Y124.

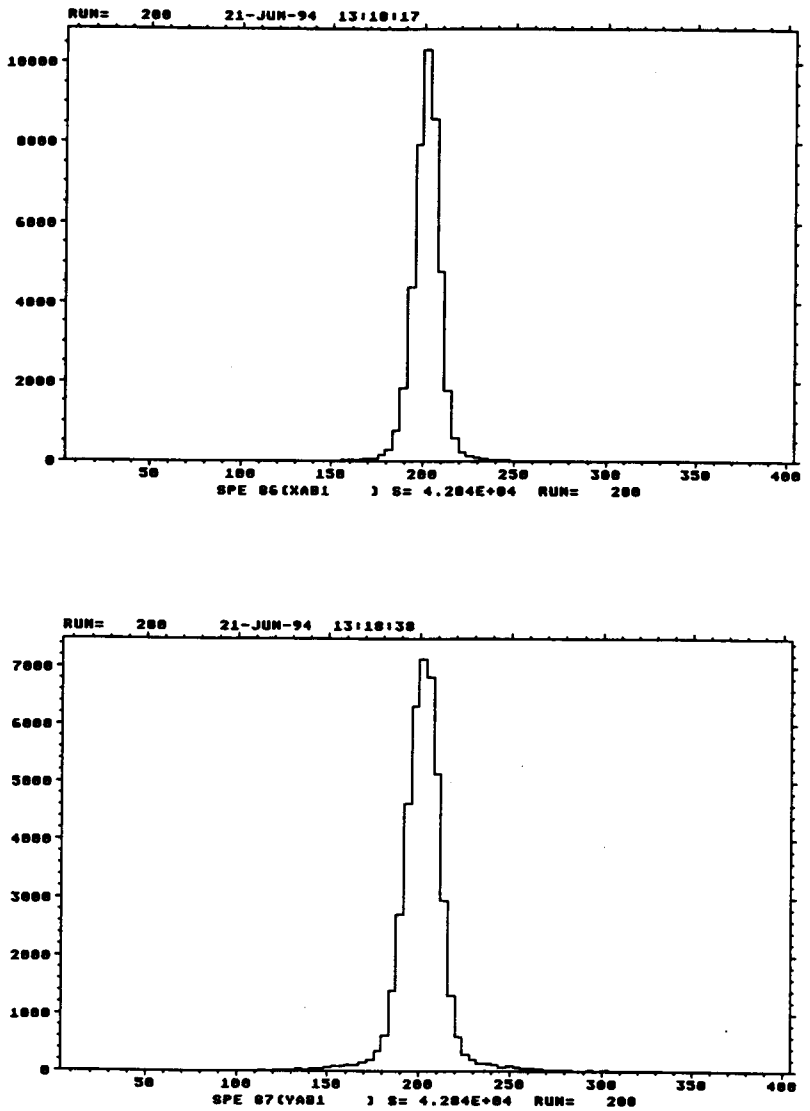

Figure 37. Typical FPP alignment (unit=0.01 mm): Top — XAB1; Bottom — YAB1.

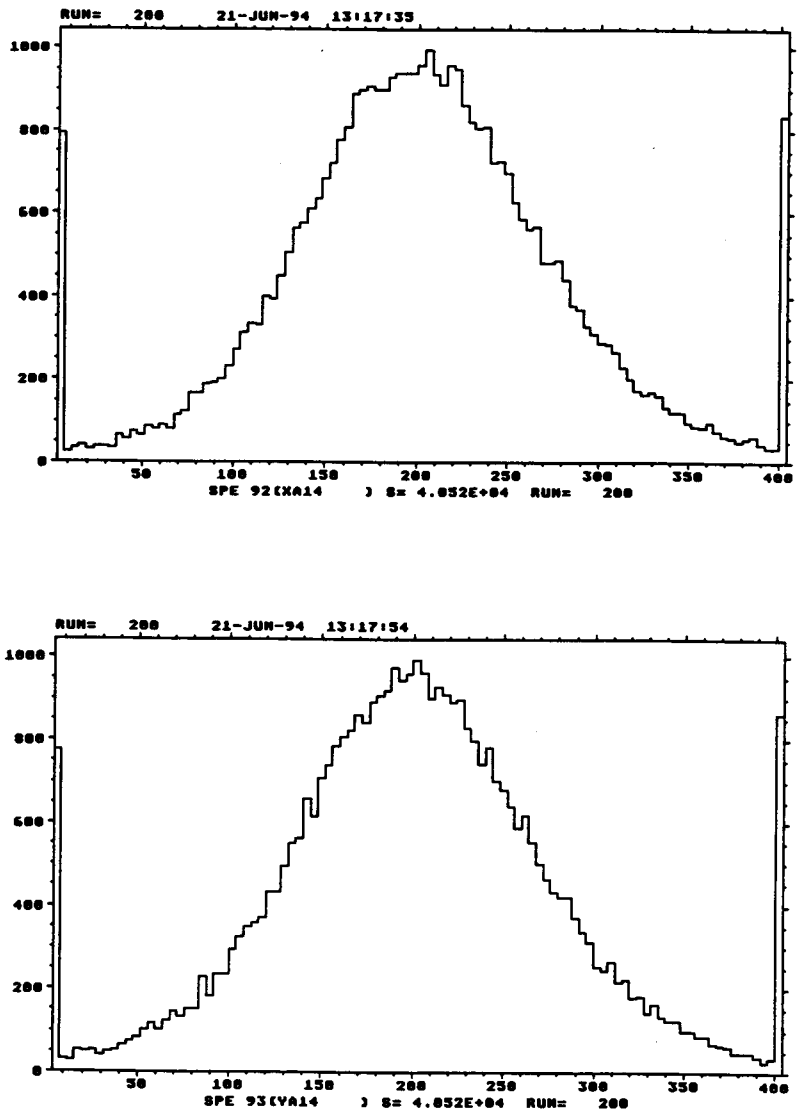

Figure 38. Typical FPP alignment (unit=0.01 mm): Top — XA14; Bottom — YA14.

5.5.2 Proton scattering angles

After proper alignment of the FPP wire chambers, the proton scattering angles θ_c and ϕ_c from carbon were determined with the wire chamber coordinates information in its projectile-helicity-system. Define $\vec{R}_{in}$ and $\vec{R}_{out}$, as shown in Figure 39, representing the trajectory vectors of the incoming and outgoing proton respectively for protons scattered by carbon.

$$\vec{R}_{in} = \vec{R}1 - \vec{R}A = (X1 - \frac{XA}{\sqrt{2}})\hat{i} + (Y1 - YA)\hat{j} + (Z1 - ZA)\hat{k} \quad (5.28)$$

$$\vec{R}_{out} = \vec{R}4 - \vec{R}2 = (X4 - X2)\vec{i} + (Y4 - Y2)\vec{j} + (Z4 - Z2)\vec{k}. \quad (5.29)$$

The polar scattering angle θ_c is defined as the opening angle between $\vec{R}_{in}$ and $\vec{R}_{out}$,

$$cos(\theta_c) = \frac{\vec{R}_{out} \cdot \vec{R}_{in}}{|\vec{R}_{out}||\vec{R}_{in}|}. \quad (5.30)$$

The azimuthal scattering angle ϕ_c is the angle between the transverse (to the optical axis) component of the scattering plane normal vector, $\vec{R}_n$, and the MRS non-bend plane, as illustrated in Figure 39

$$\cos(\phi_c) = \frac{Y_n}{R_n}, \quad (5.31)$$

$$\sin(\phi_c) = \frac{-X_n}{R_n}, \quad (5.32)$$

where $\vec{R}_n = (\vec{R}_{in} \times \vec{R}_{out})_n = (X_n, Y_n, Z_n)$.

The top histogram of Figure 40 shows a typical θ_c (in $\frac{9}{50\pi}^\circ$) distribution, in which the window was set to avoid as much as possible the asymmetry introduced by the small θ_c exclusion procedure as discussed in Section 4.7 and cover as bigger angular range in A_c data as possible. The effect of small θ_c exclusion is clearly seen. The peak near 0° was contributed by the pre-scaled events. Figure 41 and 42 are typical ϕ_c distributions for spin up and down beam polarization polarities.

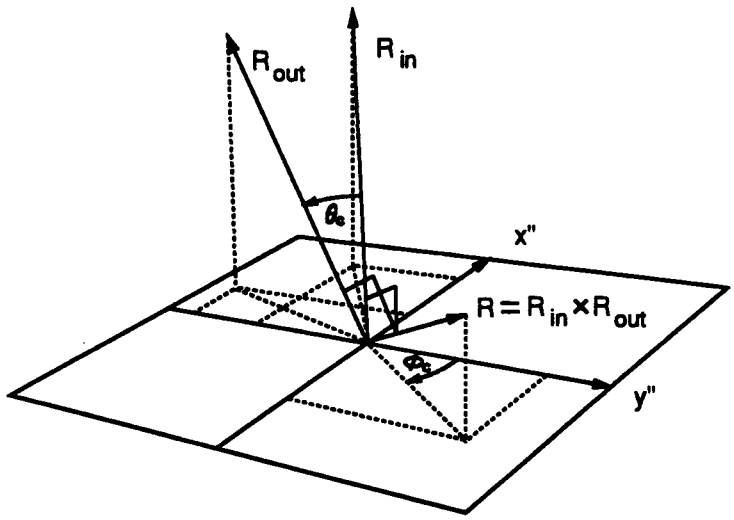

Figure 39. Illustration of p-C scattering angles

5.5.3 Carbon Scattering Vertex

With the concept of *incoming* and *outgoing* trajectory introduced in the Section 5.5.2, the scattering vertex is the vertex that connects the two trajectories. Due to the finite spatial resolution of the wire chambers the calculated incoming and outgoing trajectories generally did not meet. As an reasonable approximation, the scattering vertex was defined as the center of the closest approach of the two trajectories, as the point R shown in Figure 43. The closest distance between the two trajectories is $D_{min} = |\vec{R}_1 - \vec{R}_2|$.

One of the reasons for reconstructing the scattering vertex is to reject multiply scattered events. A typical histogram of the closest approach distance is shown in Figure 44. The value D_{min} is a monitor of how much a role the proton multiple scattering played in the carbon slab. R_z, the scattering vertex z coordinate is also a good multiple scattering indicator.R_z was measured against the physical location

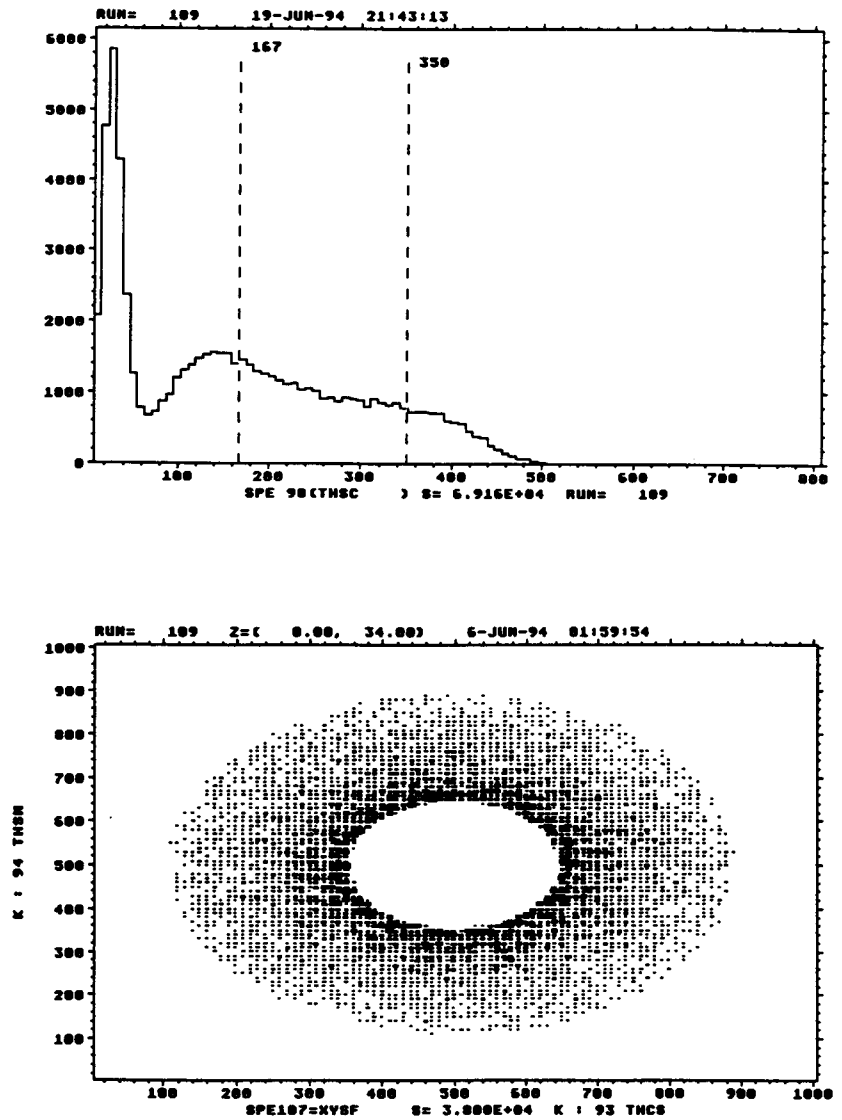

Figure 40. Typical θ_c distributions: Top — θ_c (THSC) in $\frac{9}{50\pi}^\circ$; Botton — $\theta_c \cos(\phi_c)$ vs. $\theta_c \sin(\phi_c)$ (THCS×THSN), showing only the events in the θ_c window.

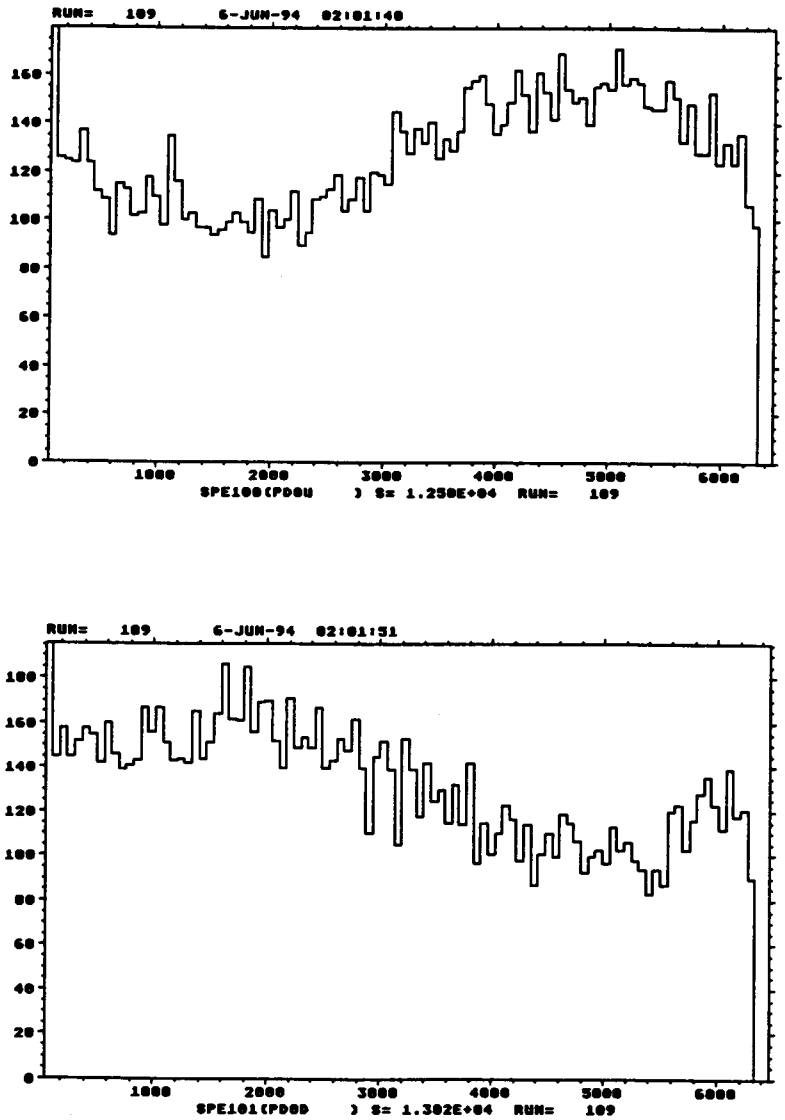

Figure 41. A typical ϕ_c asymmetry distribution, in $\frac{rad}{1000}$ with: Top — Spin up (PD0U), Bottom — Spin down (PD0D) beam polarization polarities.

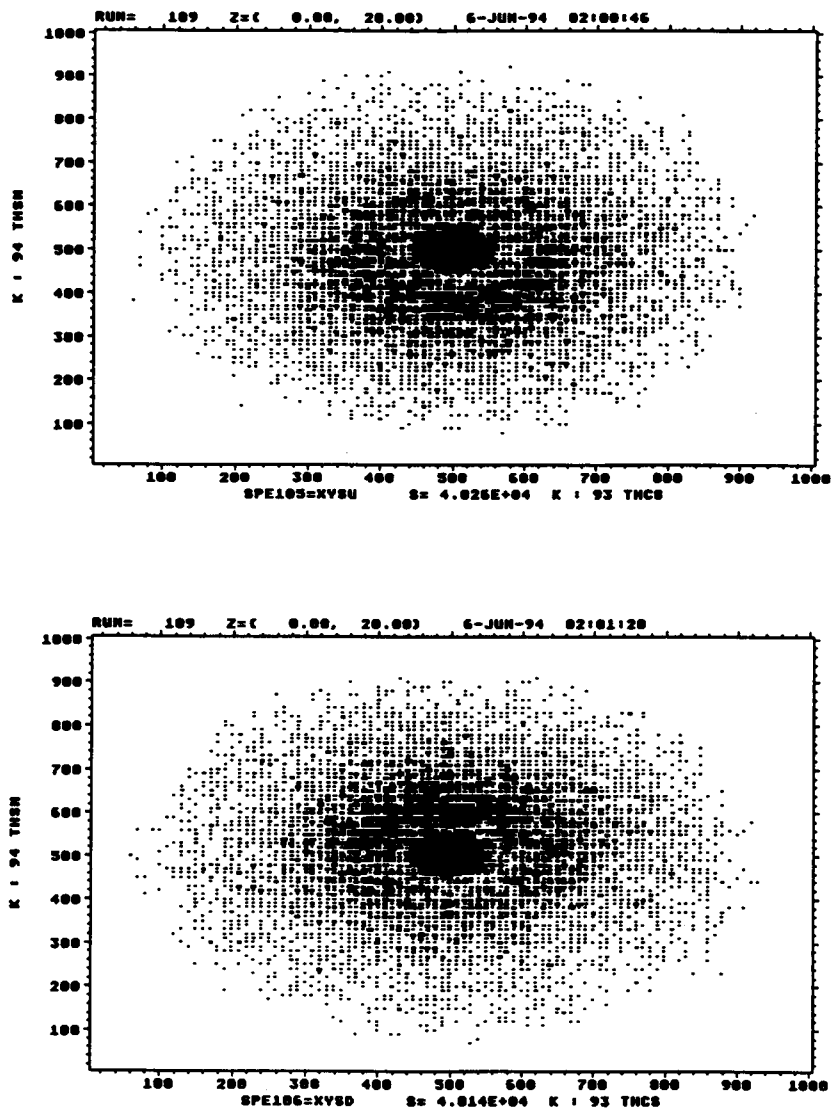

Figure 42. A typical ϕ_c asymmetry distribution in 2-D, $\theta_c \cos(\phi_c)$ vs. $\theta_c \sin(\phi_c)$ (THCS×THSN) with: Top — Spin up (XYSU), Bottom — Spin down (XYSD) beam polarization polarities.

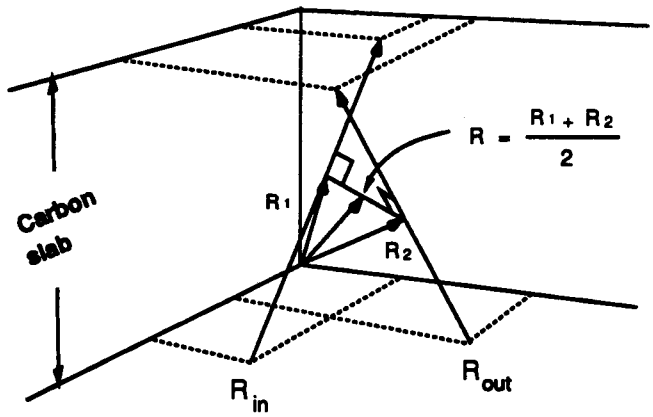

Figure 43. Proton-Carbon scattering vertex reconstruction

of the carbon analyzer along the z (optical) axis. Scattering events that happened outside the carbon slab were rejected, with $\sim$ 1cm tolerance. Figure 44 shows a histogram of typical D_{min} and R_z vertex coordinates. The vertex coordinate R_z was also used for estimating the proton energy lost in the carbon slab before scattering, which is necessary for obtaining the correct proton-carbon analyzing power which is a function of incident proton energy and proton scattering angle.

5.5.4 Cone Test

Not all the protons satisfying the tests described above in the FPP were accepted as good events. In order not to affect the asymmetry of the azimuthal scattering distribution at any polar angle by the finite openings of the chambers, a cone test was performed as the final test before an event was accepted.

With any incoming particle trajectory there exists a maximum polar scattering angle θ_{cone} defined by one of the four straight edges of the last wire chamber D_4 of FPP, see Figure 45. Scattering events with polar angles θ_c smaller than θ_{cone} would be "seen" by the chamber D_4 regardless of azimuthal scattering angle (shown as the

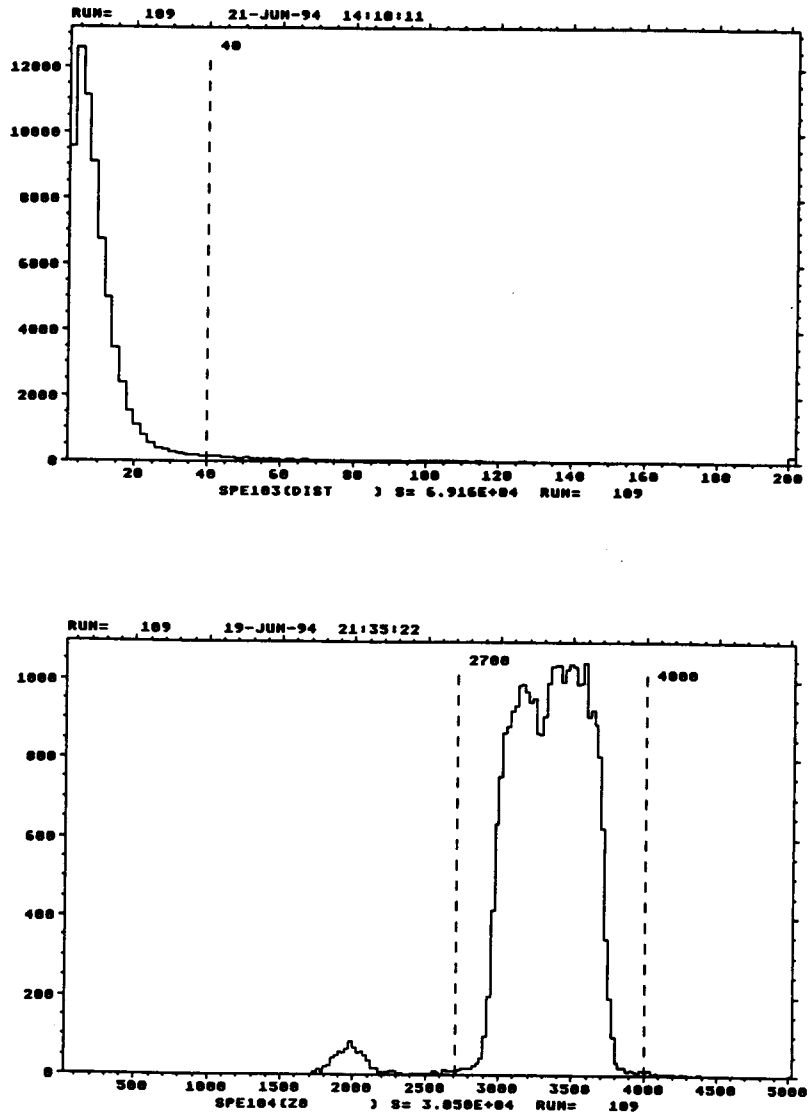

Figure 44. p-C scattering vertex: Top — A typical histogram of the closest approach, D_{min} (DIST) in 0.1 mm; Bottom — The vertex z coordinate R_z (Z0) in 0.1 mm. The dashed lines show the windows set for the variables. The small bump at 2000 in Z0 indicates the location of the scintillator S1.

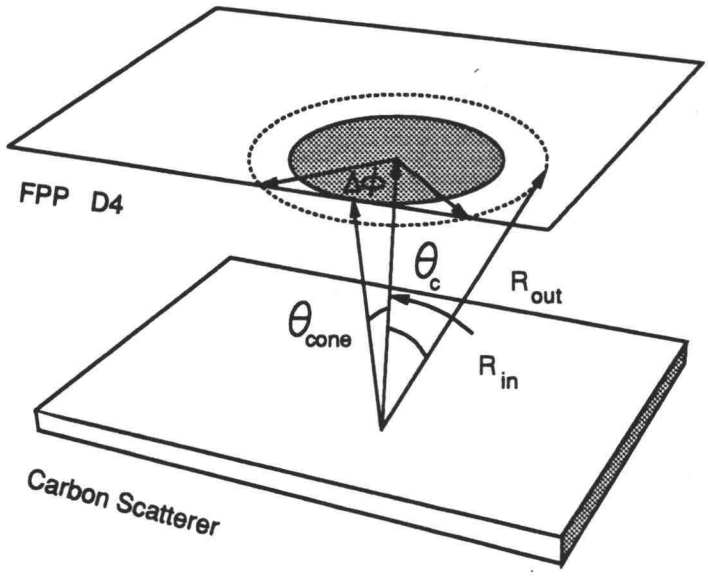

Figure 45. Cone test

shaded area), and the azimuthal asymmetries of these events would be preserved. On the other hand, for the events with $\theta_c > \theta_{cone}$ the chance of being "seen" by the chamber D_4 would not be isotropic in ϕ_c, i.e. it depended upon the azimuthal scattering angle. As illustrated in Figure 45, events with polar angle θ_c and all possible ϕ_c would appear on the dotted circle, however those with azimuthal angle falling into the region of $\Delta\phi$ would not be "seen" by the polarimeter, which creates a false azimuthal asymmetry of the ϕ_c distribution. This was avoided simply by rejecting the events with $\theta_c > \theta_{cone}$.

Each of the four edges of D_4 defines a acceptance polar angle. Obviously, the θ_{cone} should be the smallest of the four.

5.5.5 Polarization at Focal Plane

The transverse polarization components of the scattered proton at the MRS focal plane can be determined with the proton-carbon scattering angles θ_c, ϕ_c and the p-C analyzing power $A_c(E_p, \theta_c)$ [34],

$$P_{N''} = -2\frac{\sum_{event} A_c(E_p, \theta_c)\sin\phi_c}{\sum_{event} A^2(E_p, \theta_c)} \tag{5.33}$$

$$P_{S''} = 2\frac{\sum_{event} A_c(E_p, \theta_c)\cos\phi_c}{\sum_{event} A_c{}^2(E_p, \theta_c)}, \tag{5.34}$$

with statistical errors

$$\delta^2(P_{N''}) = \delta^2(P_{S''}) = \frac{2}{\sum_{event} A_c{}^2(E_p, \theta_c)}. \tag{5.35}$$

In the LISA user routine EVBEV, the A_c weighted $\cos\phi_c$ and $\sin\phi_c$ distributions over proton momentum (or focal plane coordinate XF) were defined and incremented for "up", "down" and "off" beam polarization polarities. They are histograms CP, CM, SP, SM and A,

$$A_c(E_p, \theta_c)\cos\phi_c|_{\cos\phi_c>0} \rightarrow CP, \tag{5.36}$$

$$A_c(E_p, \theta_c)\cos\phi_c|_{\cos\phi_c<0} \rightarrow CM, \tag{5.37}$$

$$A_c(E_p, \theta_c)\sin\phi_c|_{\sin\phi_c>0} \rightarrow SP, \tag{5.38}$$

$$A_c(E_p, \theta_c)\sin\phi_c|_{\sin\phi_c<0} \rightarrow SM \quad \text{and} \tag{5.39}$$

$$A_c{}^2(E_p, \theta_c) \rightarrow A. \tag{5.40}$$

If X_{pd} is the value of the integral over the p-d elastic peak momentum region of the histogram X, then using equation 5.33, 5.34 and 5.35, the focal plane polarization and their statistical errors can subsequently be determined by

$$P^{\uparrow}_{N''} = -2\frac{SP^{\uparrow}_{pd} - SM^{\uparrow}_{pd}}{A^{\uparrow}_{pd}}, \tag{5.41}$$

$$P_{N''}^{\downarrow} = -2\frac{SP_{pd}^{\downarrow} - SM_{pd}^{\downarrow}}{A_{pd}^{\downarrow}}, \tag{5.42}$$

$$P_{S''}^{\uparrow} = 2\frac{CP_{pd}^{\uparrow} - CM_{pd}^{\uparrow}}{A_{pd}^{\uparrow}}, \tag{5.43}$$

$$P_{S''}^{\downarrow} = 2\frac{CP_{pd}^{\downarrow} - CM_{pd}^{\downarrow}}{A_{pd}^{\downarrow}}, \tag{5.44}$$

$$\delta^2(P_{N''}^{\uparrow}) = \delta^2(P_{S''}^{\uparrow}) = \frac{2}{A_{pd}^{\uparrow}}, \tag{5.45}$$

$$\delta^2(P_{N''}^{\downarrow}) = \delta^2(P_{S''}^{\downarrow}) = \frac{2}{A_{pd}^{\downarrow}}, \tag{5.46}$$

where the $\uparrow$ and $\downarrow$ denotes the "up" and "down" beam polarization polarities. The calculation was carried out for each of the three beam polarizations.

The advantage of this method is that it allows one to evaluate the polarization of particles in any desired momentum region, which is important for background polarization subtraction.

5.6 Background Polarization Exclusions

There were two sources of background that need to be considered, the inevitable proton scattering from the carbon nuclei in the target and the proton inelastic scattering with deuteron (i.e. deuteron break-up). The carbon background was greatly suppressed by using the recoil deuteron coincidence counter. The recoiling deuterons were detected by a scintillator counter located inside or outside the target chamber at an appropriate angle. Most proton-carbon scattering events fail such a coincidence test due to their different kinematics than p-d elastic scattering. This method works especially well at small scattering angles where the momentum transfers are small and the scatterings are mostly elastic. This method not only cleans up the p-d elastic scattering spectrum but also frees up the data acquisition

computer time that would have been used transmitting the useless p-C events. However, residual carbon events still leaked into the data acquisition, especially at larger momentum transfer (e.g. inelastic few body final state, accidental coincidence, etc.) The p-d inelastic scattering, i.e. the deuteron break-up, starts a few MeV next to the elastic peak on the lower momentum side. Because of the finite resolution of the MRS spectrometer system the p-d elastic peak inevitably covered some inelastic events. Because the background contribution to the polarization is not proportional to its counting rate, a simple event number subtraction, as done in the case of analyzing power, is not appropriate. The asymmetry of the background needs to be subtracted.

The following technique was used to exclude the background polarization: Although it was not possible to separate the background in the p-d elastic peak and measure its polarization, we assumed the average polarization of the background in the immediate vicinity (left and right) of the p-d elastic scattering peak best resembles that of the background events inside the peak region. Define the following variables:

- P_b – the background polarization,
- P_{obs} – the observed polarization of all the events, i.e. p, d events and all the background events,
- P_d — the polarization of the p, d elastic events,
- N_b — the background count in the p, d region, and
- N_d — p, d elastic event count in the p, d region,

then the following relation holds,

$$N_b P_b + N_d P_d = (N_b + N_d) P_{obs}. \tag{5.47}$$

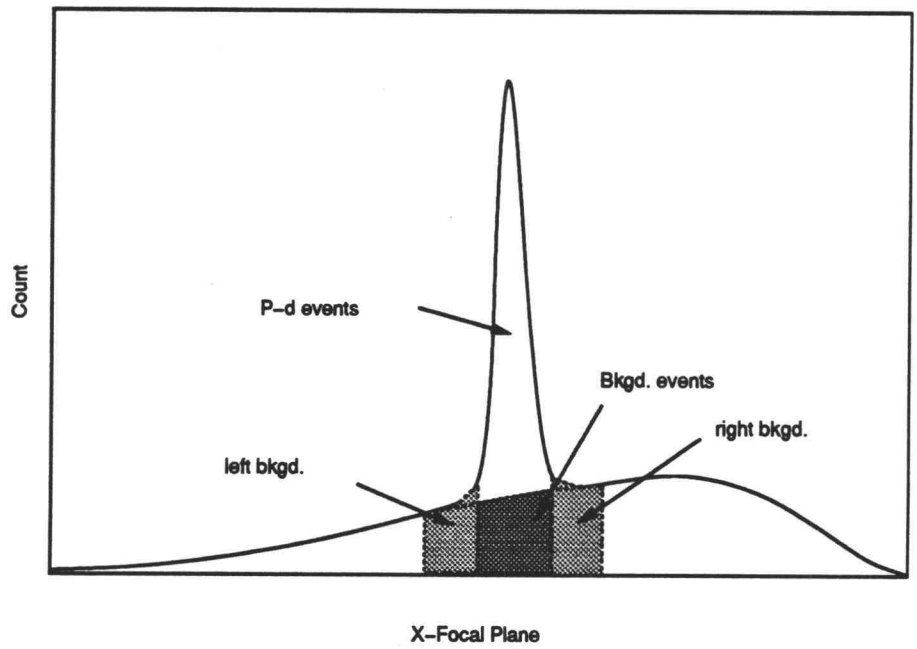

Figure 46. Method for subtracting the background polarization

The polarization of the p-d elastic events P_d then is solved as

$$P_d = \frac{(N_b + N_d)P_{obs} - N_b P_b}{N_d}. \tag{5.48}$$

N_b was determined by estimating the background inside the p-d elastic peak region (see Figure 46), similar to the method used in the p-d analyzing power determination, and an estimated uncertainty dN_b was assigned to N_b, which contributed to the non-statistic error of the polarizations.

5.7 Spin Transfer Coefficients

The equation 3.34 in Section 3 was used to derive the expressions for the spin transfer coefficients. Because the MRS dipole magnet precesses the particle spin

about the field direction (horizontal), the focal plane polarizations P_S'' P_N'' and P_L'' are related to the scattered proton polarizations P_S', P_N' and P_L' in their projectile-helicity-frame by a rotation through the precession angle χ,

$$\begin{pmatrix} P_S'' \\ P_N'' \\ P_L'' \end{pmatrix} = \begin{pmatrix} 1 & 0 & 0 \\ 0 & \cos(\chi) & \sin(\chi) \\ 0 & -\sin(\chi) & \cos(\chi) \end{pmatrix} \begin{pmatrix} P_S' \\ P_N' \\ P_L' \end{pmatrix}, \tag{5.49}$$

where the precession angle $\chi = \gamma(\mu - 1)\alpha$, γ is the Lorentz factor, μ is the proton magnetic moment and α is the bend angle of proton trajectory in the MRS dispersion plane ($\sim 60.5°$ for MRS).

We assumed that for each data taking run the beam polarization of two opposite polarities are close in magnitudes (see Table 19 and 20 in Appendix C), i.e.

$$P_{k\uparrow} = P_{k\downarrow} = P_k \qquad (k = S, N, L). \tag{5.50}$$

Combine the equation 3.34 and 5.49 and solve for the spin transfer coefficients in a iterative manner[6] (Appendix A),

$$P_N(\theta) = \frac{1}{2\cos(\chi)}[(1 + P_N A_N)P_{N''}^{\uparrow} + (1 - P_N A_N)P_{N''}^{\downarrow}] \tag{5.51}$$

$$D_{SS} = \frac{1}{2P_S}[(1 + P_N A_N)P_{S''}^{\uparrow} - (1 - P_N A_N)P_{S''}^{\downarrow} - 2D_{LS}P_L] \tag{5.52}$$

$$D_{SL} = \frac{1}{2P_S\sin(\chi)}[(1 + P_N A_N)P_{N''}^{\uparrow} - (1 - P_N A_N)P_{N''}^{\downarrow}) - 2P_N D_{NN}\cos(\chi) - 2P_L D_{LL}\sin(\chi)] \tag{5.53}$$

$$D_{NN} = \frac{1}{2P_N\cos(\chi)}[(1 + P_N A_N)P_{N''}^{\uparrow} - (1 - P_N A_N)P_{N''}^{\downarrow}) - 2P_S D_{SL}\cos(\chi) - 2P_L D_{LL}\sin(\chi)] \tag{5.54}$$

$$D_{LL} = \frac{1}{2P_L\sin(\chi)}[(1 + P_N A_N)P_{N''}^{\uparrow} - (1 - P_N A_N)P_{N''}^{\downarrow}) - 2P_N D_{NN}\cos(\chi) - 2P_S D_{SL}\sin(\chi)] \tag{5.55}$$

$$D_{LS} = \frac{1}{2P_L}[(1 + P_N A_N)P_{S''}^{\uparrow} - (1 - P_N A_N)P_{S''}^{\downarrow} - 2D_{SS}P_S] \tag{5.56}$$

$$C_{SS} = (1 + P_N A_N)P_{S''}^{\uparrow} + (1 - P_N A_N)P_{S''}^{\downarrow}. \tag{5.57}$$

[6]For simplicity in notation, the prime index "′" for the reactant system was omitted.

where C_{SS} is a check variable whose value should be close to zero. The results of C_{SS} are listed in Table 8.

Chapter 6

Results and Conclusion

In this Chapter, the results of the data analysis for this experiment are presented; some discussion is made from the point view of the Time Reversal Invariance (TRI) and the aspects of the experimental systematic errors; The spin observable data are compared with some theoretical calculations based on the multiple-scattering approach.

The measured spin observables are listed in Table 6 and 7. They are analyzing power A_N, target induced polarization P_N, and five polarization transfer coefficients D_{NN}, D_{LL}, D_{SS}, D_{SL}, D_{LS} at 400 and 290 MeV incident proton energies and 20 to 80°[7] proton scattering angles in lab system. The plots of the spin observables are shown with Figures from 60 and 64. The intermediate analysis results, including beam polarizations and scattered proton polarizations at the focal plane are listed in Appendix C.

[7]The spin transfer results at 290 MeV, 60° were missing because the longitudinal focal plane polarization data in this case were not successfully recorded during the experiment.

6.1 Checks With Time Reversal Invariance

As discussed in Chapter 3, because of parity conservation, eight of the fifteen spin observables in the $\vec{p}$-d elastic scattering vanish. If time reversal invariance (TRI) holds for the reaction, then there are the following inter-relations among the non-vanishing observables in the p-d center of mass system or Breit system,

$$A_N = P_N \tag{6.1}$$

$$D_{sl} = -D_{ls}. \tag{6.2}$$

For a spin-0 target the analyzing power A_N is automatically equal to the induced polarization P_N, and for spin non-zero target, the relation $A_N \cong P_N$ holds even if there is a violation to the time reversal invariance when $D_{NN} \cong 1$. The measured D_{NN} in this experiment is obviously different from unity except at scattering angles $\theta < 40°$ for 400 MeV incident proton energy, as shown in Figure 62 and 66. Therefore $\vec{p}$-d elastic scattering is a reasonably good choice for testing time reversal invariance in this energy range.

The comparison of analyzing power and induced polarization (Figure 47 and 48 shows that the relation 6.1 is satisfied within the experimental uncertainties[8] for 400 and 290 MeV. For more quantitative test, A quantity K [4] can be introduced,

$$K = \frac{1-T}{1+T}, \tag{6.3}$$

where T is a time reversal invariance violating factor. If $T = 1$ or $K = 0$ then there is no TRI violation. It can be proved that

$$K = \frac{P_N(\theta) - A_N(\theta)}{1 - D_{NN}}. \tag{6.4}$$

[8] All the error bars shown are only statistical errors. The non-statistical errors are listed in the result tables.

The values of K are listed in Table 9. The K results are consistent with time reversal invariance within the experiment uncertainties at 400 and 290 MeV incident proton energies.

In order to check the consistency of the measured spin observables with the time reversal invariance relation 6.2 we need to obtain the spin transfer coefficients in the proton-deuteron center of mass system. It can be shown [4] that the spin transfer coefficients of the proton-deuteron elastic scattering in the lab system are related to that in the p, d center of mass system by the following matrix equation,

$$\begin{pmatrix} D_{ss} \\ D_{ll} \\ D_{ls} \\ D_{sl} \end{pmatrix}_{CM} = \begin{pmatrix} a & b & -c & -d \\ b & a & d & c \\ c & -d & a & -d \\ d & -c & -b & a \end{pmatrix} \begin{pmatrix} D_{SS} \\ D_{LL} \\ D_{LS} \\ D_{SL} \end{pmatrix}_{Lab}, \tag{6.5}$$

in which

$$\begin{aligned} a &= cos\chi cos\chi', \\ b &= sin\chi sin\chi', \\ c &= sin\chi cos\chi', \\ d &= cos\chi sin\chi', \end{aligned} \tag{6.6}$$

where the χ and χ' are defined (in the center of mass system) in terms of $\theta_{\text{c.m.}}$ and $\bar{\theta}_L$, the scattering angles of the scattered proton in the center of mass system and anti-laboratory (Figure 49) system [14], respectively,

$$\chi = \frac{\theta_{\text{c.m.}}}{2}, \quad \chi' = \frac{\theta_{\text{c.m.}}}{2} + \bar{\theta}_L. \tag{6.7}$$

The transformed polarization transfer coefficients in the p-d center of mass system are shown in Table 10 and 11. The comparisons of the D_{sl} and D_{ls} for 400 and 290

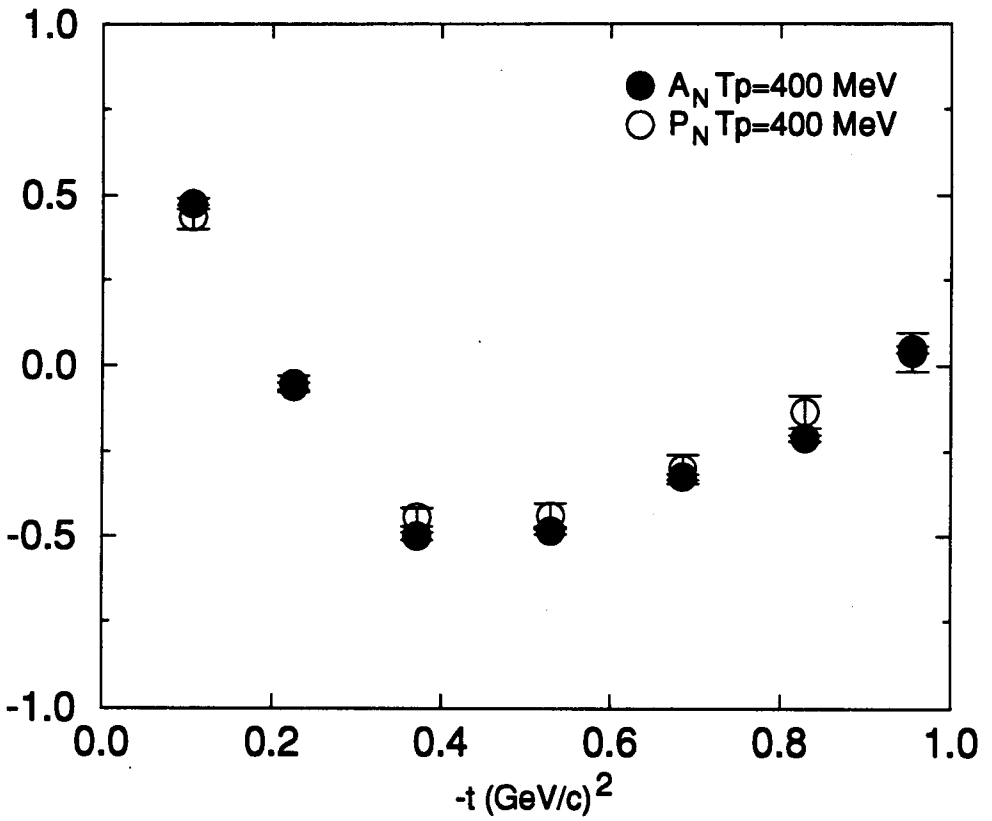

Figure 47. Comparison of A_N and P_N (Tp=400 MeV)

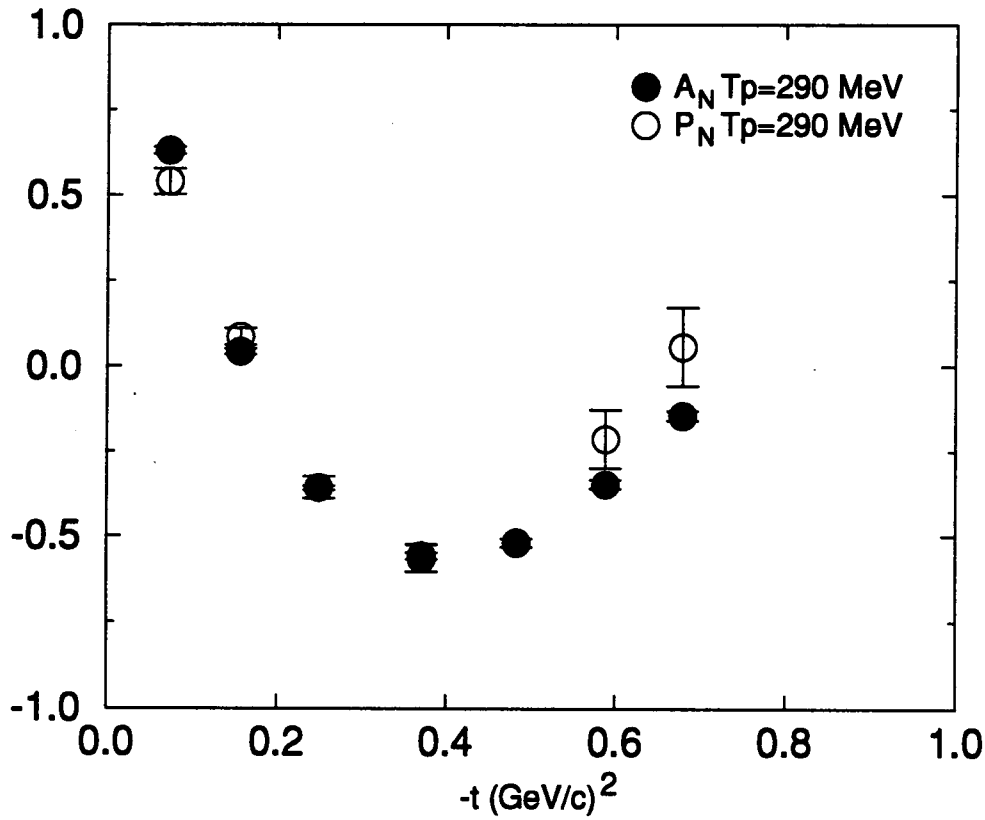

Figure 48. Comparison of A_N and P_N (Tp=290 MeV)

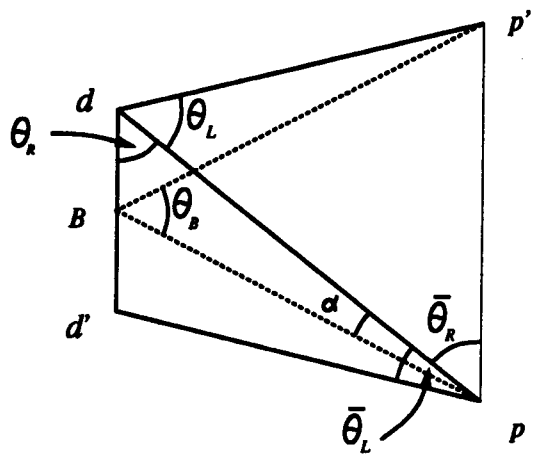

Figure 49. The velocity diagram with laboratory scattering and recoil angles θ_L and θ_R, and corresponding anti-laboratory angles $\bar{\theta}_L$ and $\bar{\theta}_R$. The Breit system scattering angle is θ_B. The angle α is related to Wigner angles

MeV proton energies are shown in Figure 50 and 51. It can be seen that within the experimental uncertainties the experimental data are consistent with the time reversal invariance relation 6.2.

6.2 Carbon Analyzing Power and Multiple Scattering

In the 50 to 140 MeV energy region (where the 80 and 70° scattered protons of the 400 and 290 MeV beam fell after 10 to 30 MeV energy loss), the carbon analyzing power has the largest slope (~0.4/100 MeV). However there was only one carbon analyzing power data point available for numerical fit in this region. As a result, the two dimensional fit in this energy region has potentially the least accuracy (Appendix B).

For a proton of energy ~100 MeV, the energy lost due to multiple scattering

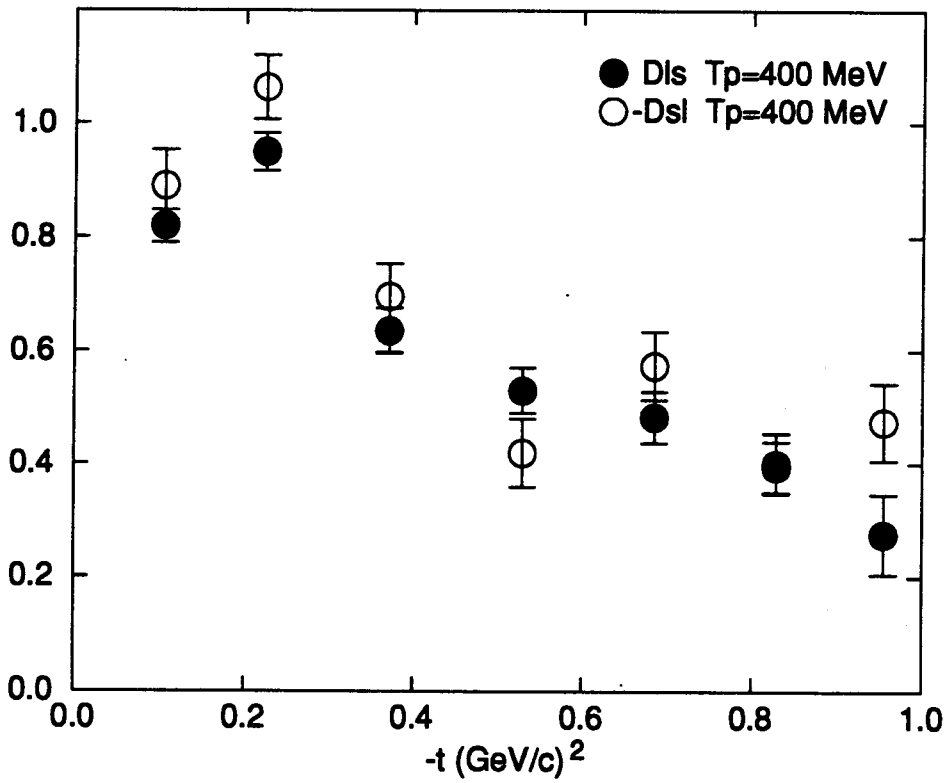

Figure 50. Comparison of D_{sl} and $-D_{ls}$ at 400 MeV

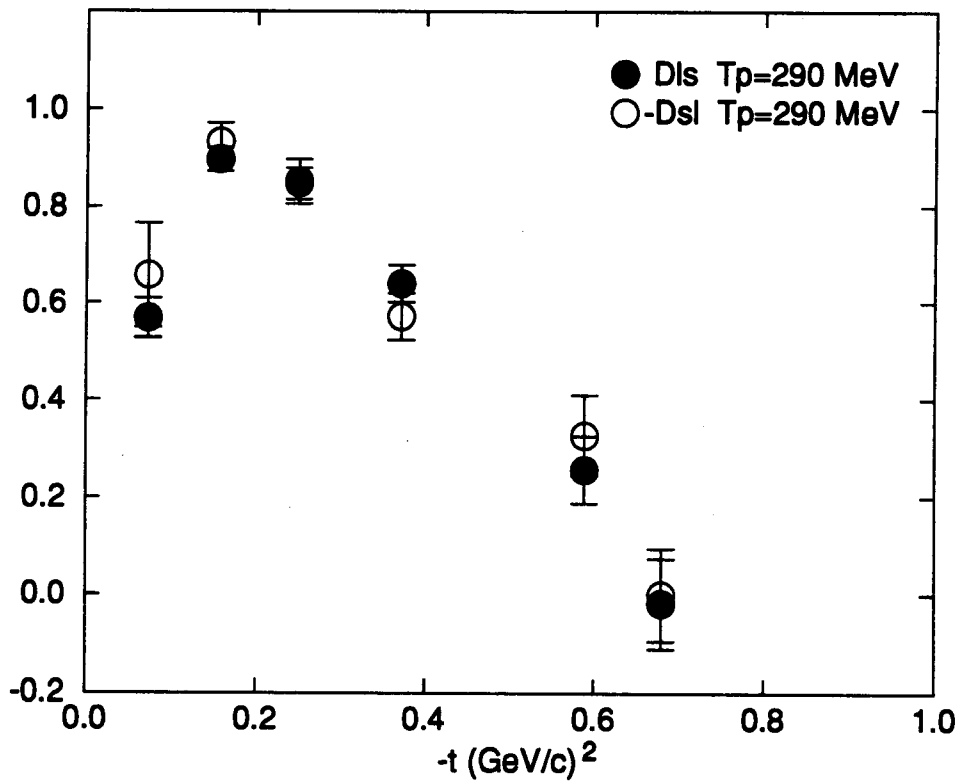

Figure 51. Comparison of D_{sl} and $-D_{ls}$ at 290 MeV

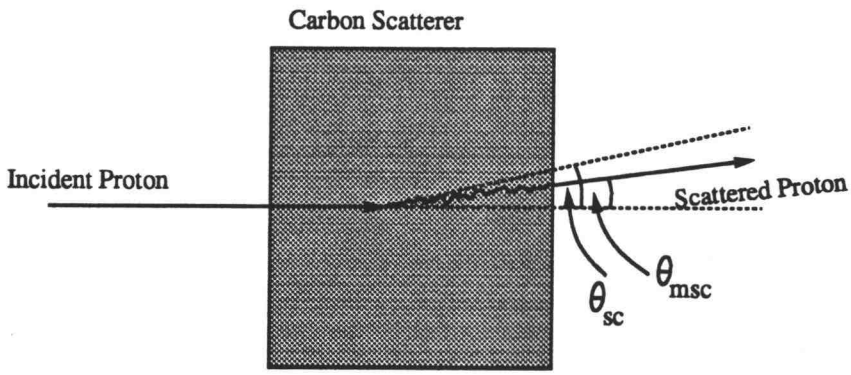

Figure 52. The proton multiple scattering in carbon. θ_{sc} is the real scattering angle, θ_{msc} is the angle after multiple scattering

in the carbon scatterer of the Focal Plane Polarimeter can be as high as 30% of its initial energy. The lost energy in principle is an accumulation of series of smaller scattering processes which modify the original proton-carbon scattering angles θ_c and ϕ_c, as illustrated in Figure 52. The multiple scattering effect gets more severe as the energy of the proton energy becomes lower. This could introduce error in polarization only if the thickness of the carbon scatterers used in the experiment were inconsistent with those used to obtain A_c data, which they were, to some extent, as shown in Table 3, 4 and Appendix B.

6.3 Comparison with Multiple Scattering Calculation

Theoretical calculation for the p-d elastic scattering spin observables have been made through several approaches. At the low proton energy region, <100 MeV, exact solution can be calculated using the Faddeév equations for the scattering amplitude. At higher energies, multiple scattering approximations are usually introduced so finite terms of the multiple scattering amplitudes can be selected for

the calculations. At very high incident proton energies, > 1 GeV, the calculations based on the Glauber multiple scattering model have been popular [14]. However the eikonal approximation of the Glauber model limits its application to the intermediate energy region, $\sim 200 - 500$ MeV. Because the nucleon-nucleon interaction amplitude becomes large and varies rapidly at intermediate energies, the convergence of the p-d scattering amplitude is expected to be poor, which is the most serious issue at 500 MeV and below and makes the calculation in this energy region more challenging.

For the comparison with the data of this experiment, spin observables of p-d elastic scattering has been calculated[9] for 400 MeV incident proton energy. The theoretical base of the calculation cited in this thesis is a multiple scattering expansion of the p-d scattering amplitude of the Faddeév equations [5]. The Lee nucleon-nucleon amplitude (Section 2.1.3) was used as the NN interaction in the calculation. The NN interaction amplitude was converted into functions of seven Wolfenstein coefficients [35] of spin invariants representing the spin dependent forces in the NN interaction, which makes the observation of the effects of various spin dependent forces convenient. Relativistic kinematics was used in the calculation of phase space p-d vs. NN center of mass frame changes and the energy denominators. Relativistic dynamics, which describes the fact that the off-shell NN amplitudes are frame dependent, was not included. It is generally a small effect even at 800 MeV [38], where the multiple scattering series converges quite well. Test calculation has shown that the difference between allowing the full off-shell dependence of the NN amplitude in the multiple scattering vs. constraining the amplitudes to their on-shell values as determined by the projectile energy, are much greater than the relativistic dynamical effects in the intermediate energy region.

[9]The calculation has been done by Prof. B. Keister at Carnegie Mellon University.

The calculation process has been continuously progressing. Limited by the current computing power the calculation has so far been concentrated on the calculation with A (central) and C (spin-orbit coupling) Wolfenstein spin dependence coefficients, single and single+double multiple scattering t-matrix terms. The options of on-shell and fully off-shell dependence of NN scattering were used. The effects of the calculation options on the differential cross sections are shown in Figure 53. The results of the calculation for 400 MeV p-d spin observables are presented in Table 12 through 15. The comparison with experimental data are shown in Figure 54 through 59.

The calculation shows a significant sensitivity of p-d spin observables to on-shell and fully off-shell dependence NN interaction. The experiment data (A_N, D_{SS}, D_{LL}, D_{SL}, and D_{LS}) in general, present a better agreement with the trends of the results of the fully off-shell, single+double scattering calculations. The fact that the measured D_{NN} generally disagrees with the calculated values, especially at large momentum transfer for both of the 400 and 290 MeV proton energies and that the calculation is relatively insensitive to on-, off-shell and single, double scattering variations may be suggesting that D_{NN} be more sensitive to other spin dependent forces than central and spin-orbit (A and C).

At 400 MeV the double scattering began to play an important role starting from $\sim 10 - 20^\circ$ in the lab system.

6.4 Conclusion

Proton-deuteron elastic scattering as the simplest few body system is expected to have significant advantages over two nucleon processes in the investigation of nucleon-nucleon interactions, one of the most fundamental problems in nuclear

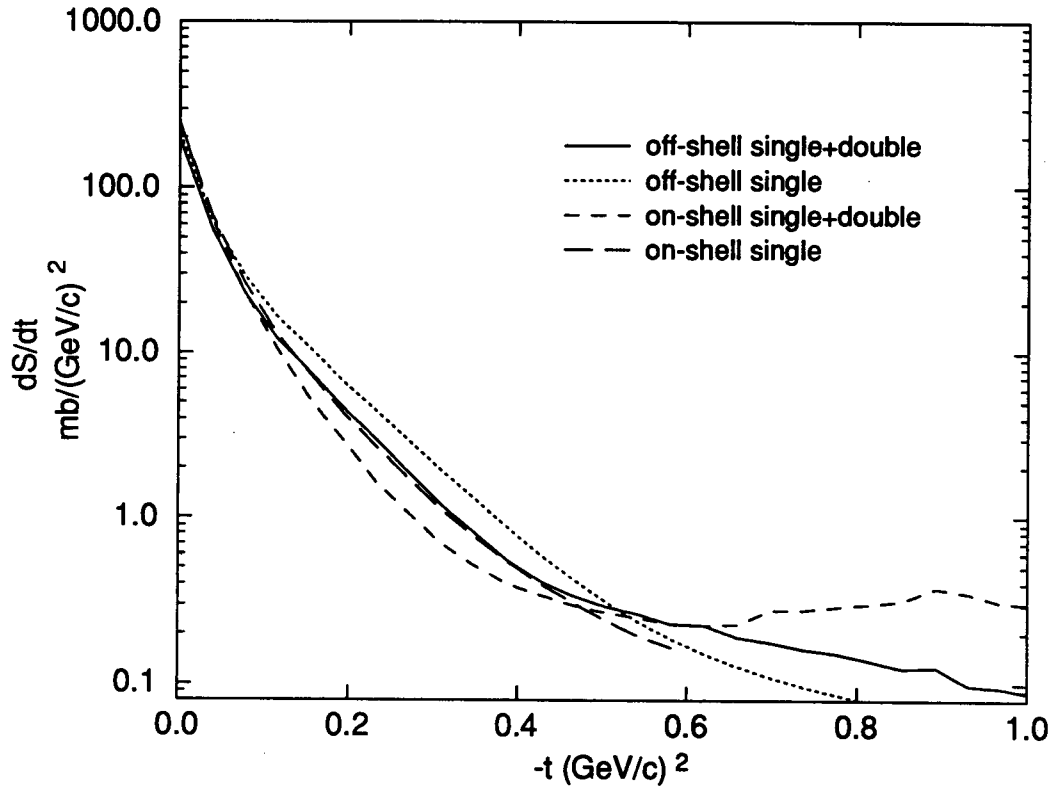

Figure 53. Differential cross section, (T_p=400 MeV)

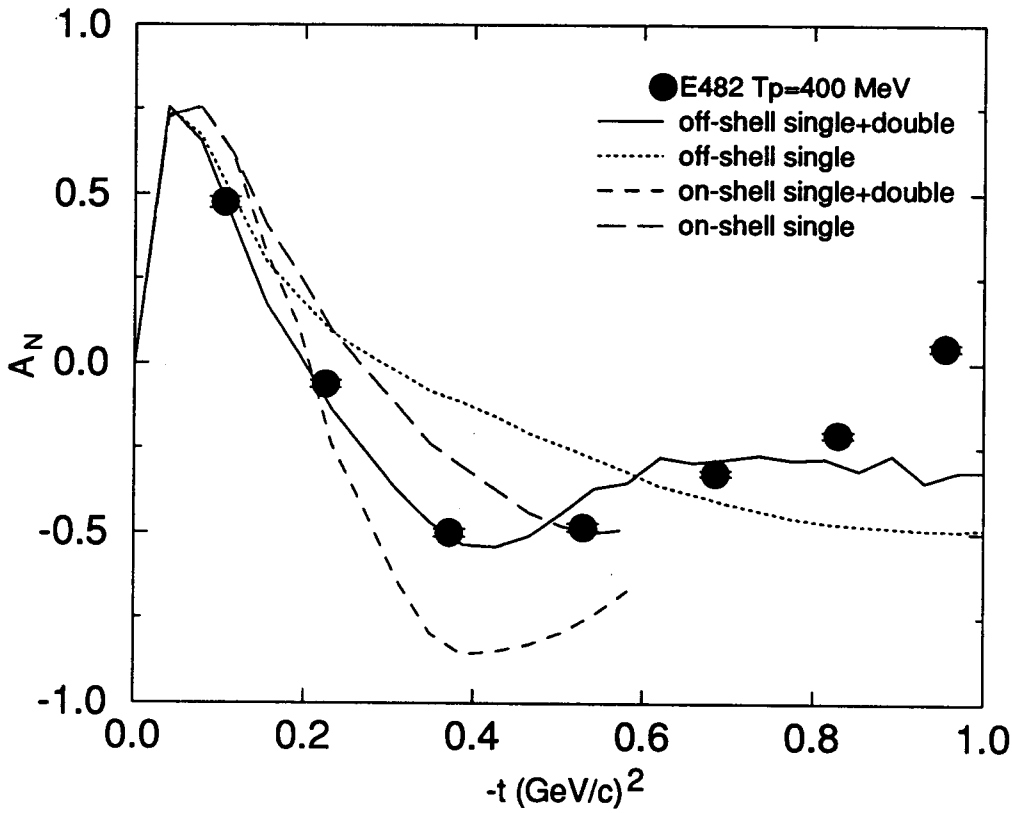

Figure 54. Analyzing power A_N, (T_p=400 MeV)

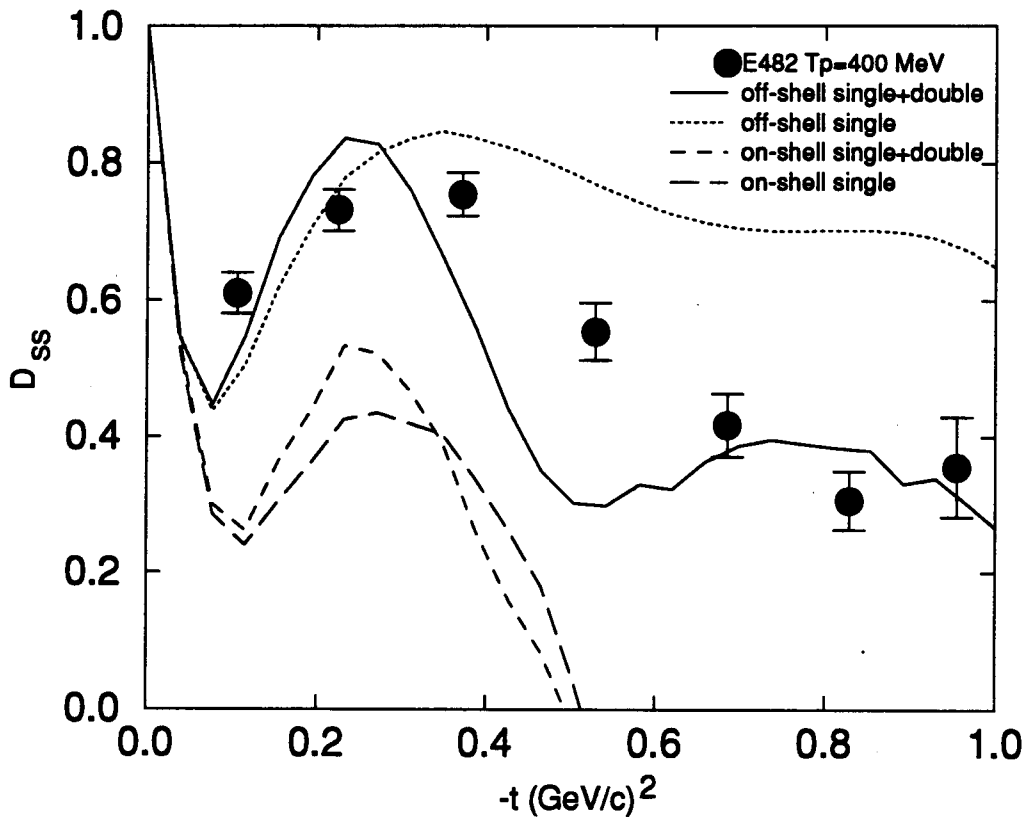

Figure 55. Spin transfer coefficient D_{SS}, (T_p=400 MeV)

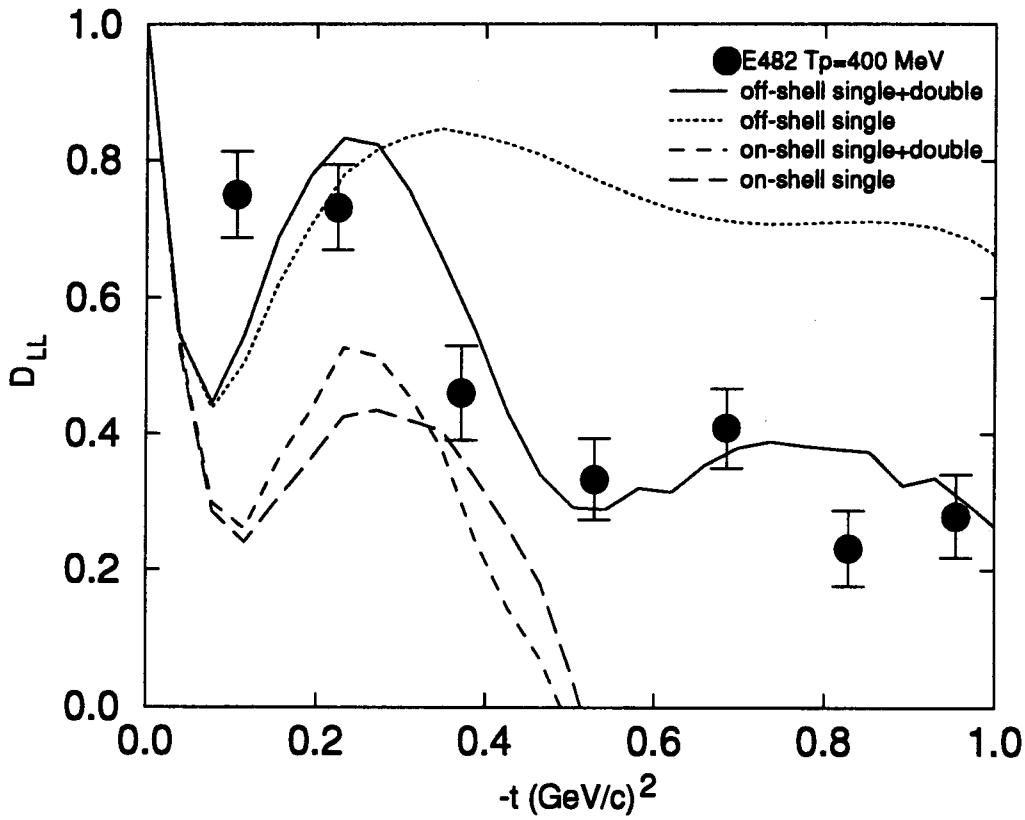

Figure 56. Spin transfer coefficient D_{LL}, (T_p=400 MeV)

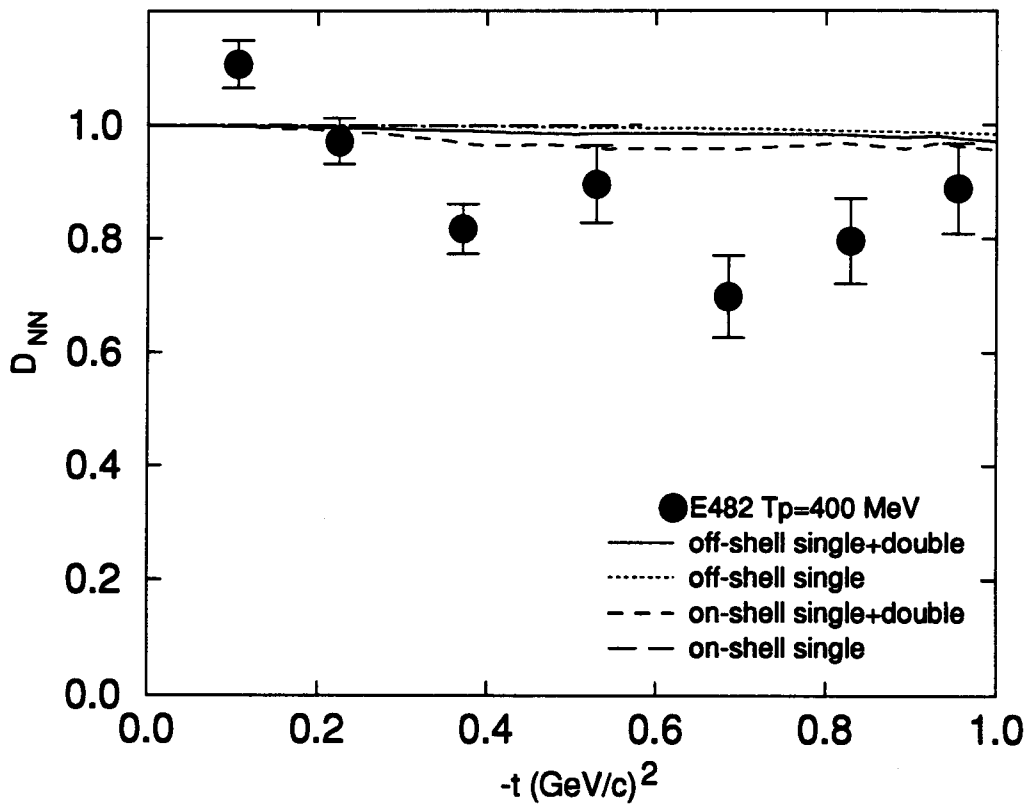

Figure 57. Spin transfer coefficient D_{NN}, (T_p=400 MeV)

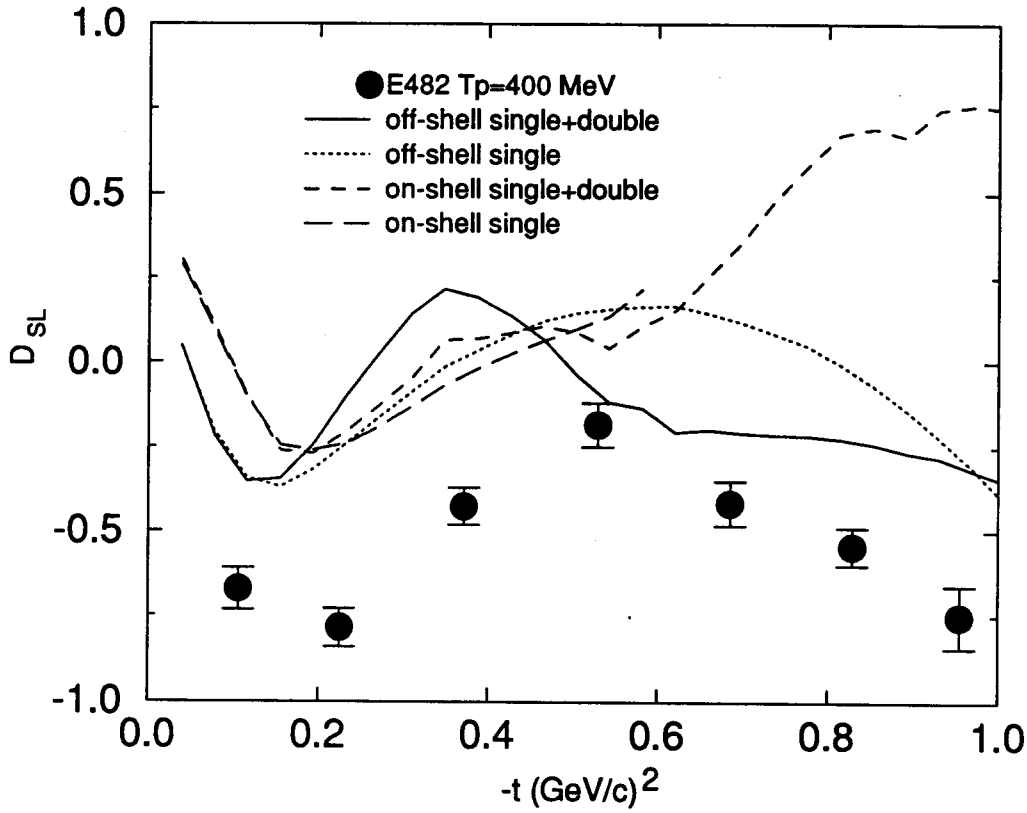

Figure 58. Spin transfer coefficient D_{SL}, (T_p=400 MeV)

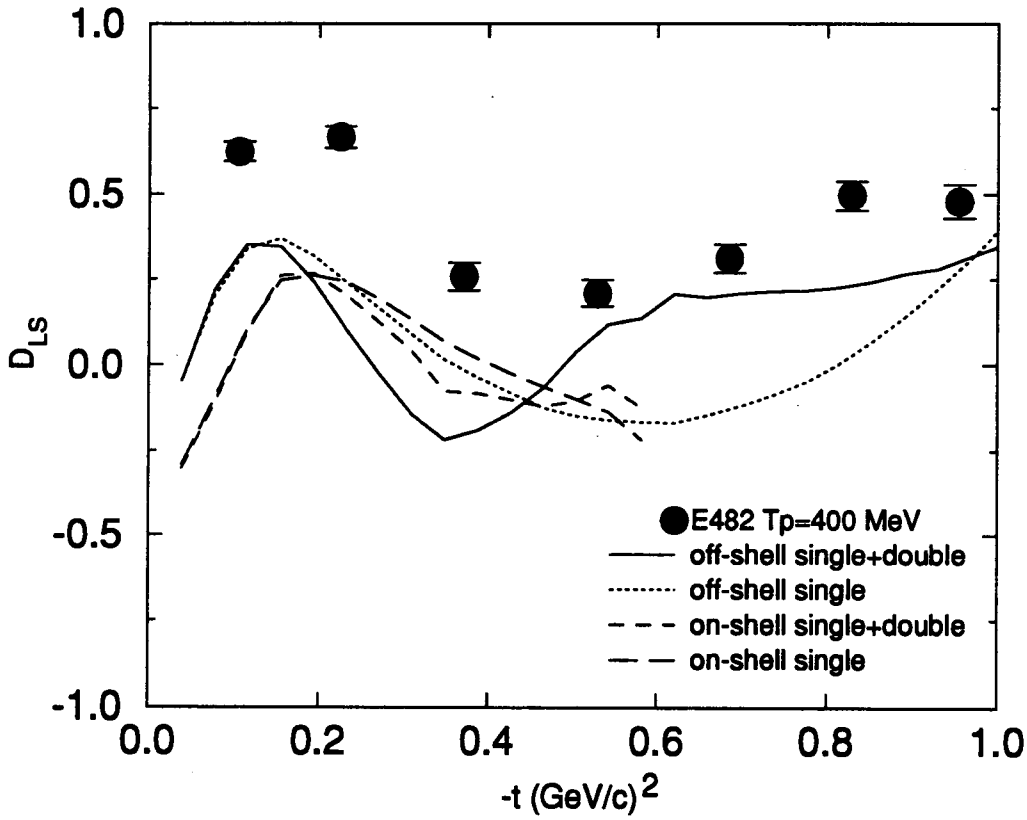

Figure 59. Spin transfer coefficient D_{LS}, (T_p=400 MeV)

physics, in the aspects of off-shell dependence and spin dependent forces. The 200 to 500 MeV incident proton energy region, where no spin observable measurement has been made up to now, is a fundamental region of nuclear physics where the Δ plays an important role, and it represents a great challenge to the theoretical explanation.

In this experiment, we have measured the parity allowed spin observables for proton-deuteron elastic scattering, including analyzing power A_N, induced polarization P_N, five spin transfer coefficients D_{NN}, D_{SS}, D_{LL}, D_{SL}, and D_{LS} at 290 and 400 MeV incident proton energies. The scattering angle of the proton is chosen from 20 to 80° in the lab system, which corresponds a momentum transfer from 0.05 to 0.96 $(GeV/c)^2$.

At 400 and 290 MeV, the measured spin observables showed good consistence with the time reversal invariance within the experimental uncertainties.

Theoretical calculations for the p-d elastic scattering spin observables based on the multiple scattering expansion of Faddeév equations have been made at 400 MeV using the central and spin-orbit Wolfenstein coefficients (A, C) of spin invariants. The calculation has been done using the options of on- off-shell nucleon-nucleon interaction, single and single+double scattering terms. The data showed a generally better agreement with the results of the calculation using fully off-shell NN interaction and single+double multiple scattering terms; the sensitivity to central and spin-orbit forces varies with individual observables.

The experimental data showed clearly that the calculation options, i.e. the A and C Wolfenstein coefficients of spin invariants, single and double multiple scatterings were not enough to describe all the spin observables in satisfactory details. The double scattering term in the multiple scattering series became significant at $\sim 10° - 20°$ in the lab system, which is a signal of slower convergence of the multi-

ple scattering t-matrix series in the region of higher momentum transfer. However, the comparison of the data with the results of the calculation has revealed interesting potentials of the simple few-nucleon systems, such as proton-deuteron elastic scattering in the investigations of the off-shell and spin dependence aspects of nucleon-nucleon interaction. It is hopeful that further and more systematic investigations of the experimental results with more spin dependent forces and higher order multiple scattering terms will extract useful information about the nature of the nucleon-nucleon interaction.

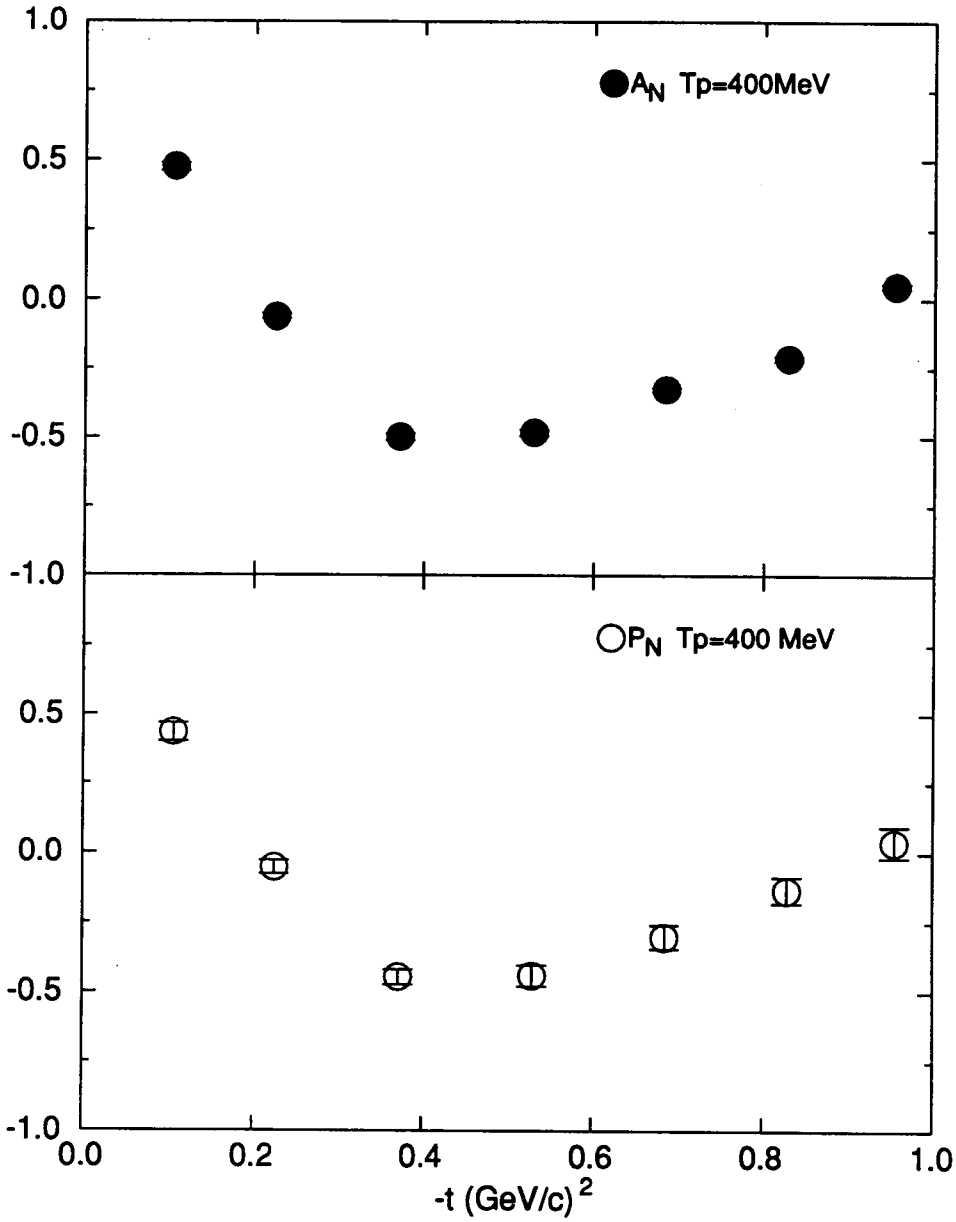

Figure 60. A_N, P_N (T_p= 400MeV)

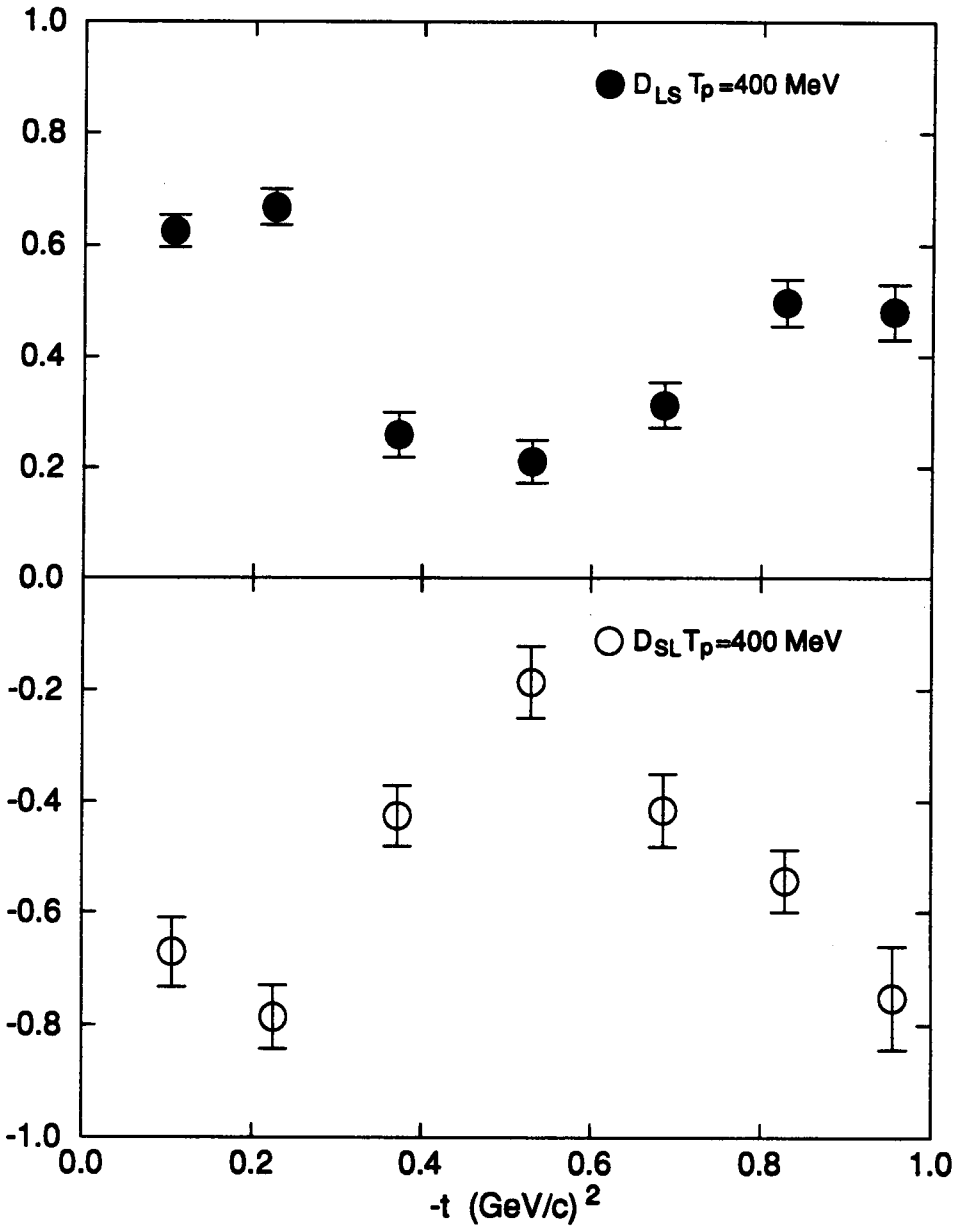

Figure 61. D_{LS}, D_{SL} (T_p=400 MeV)

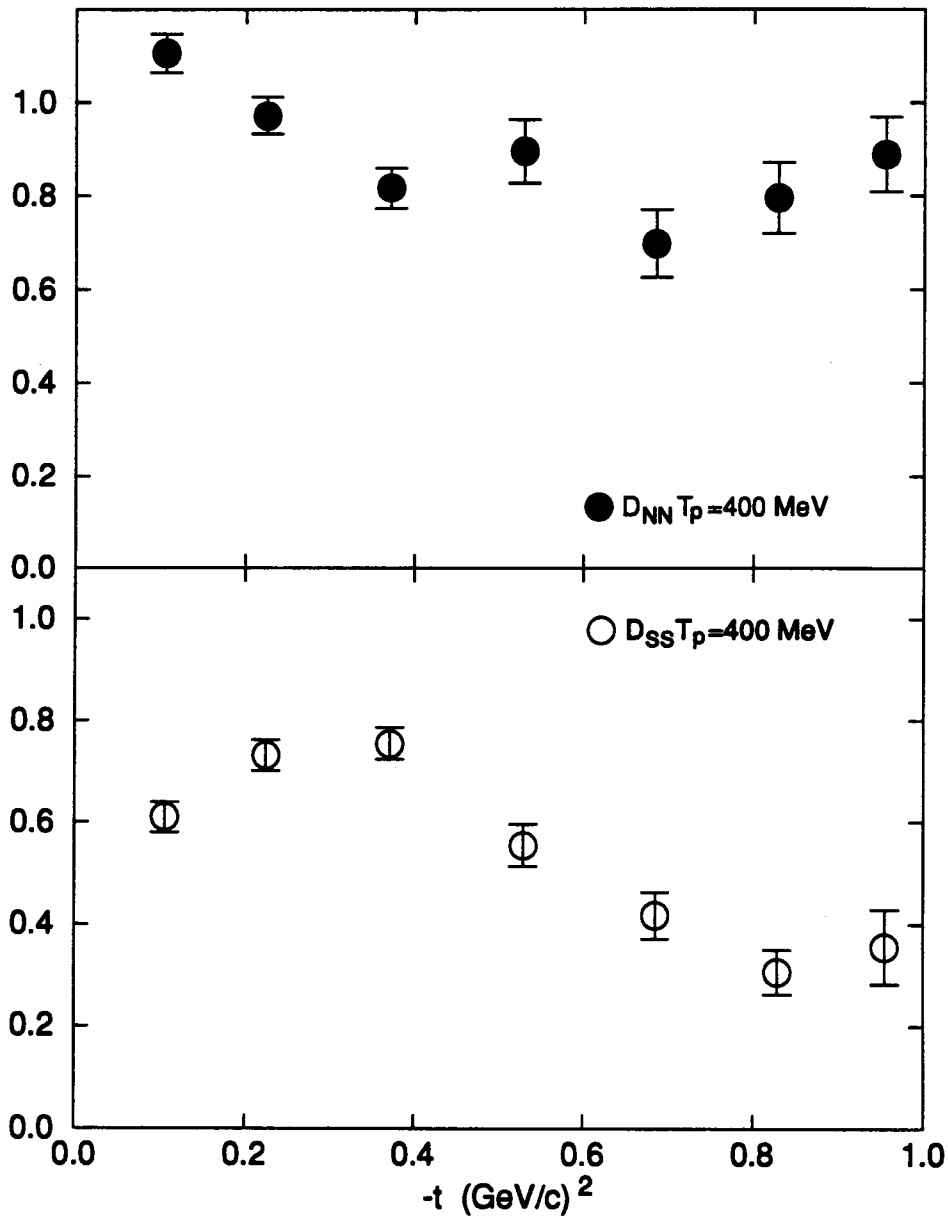

Figure 62. D_{NN}, D_{SS} (T_p=400 MeV)

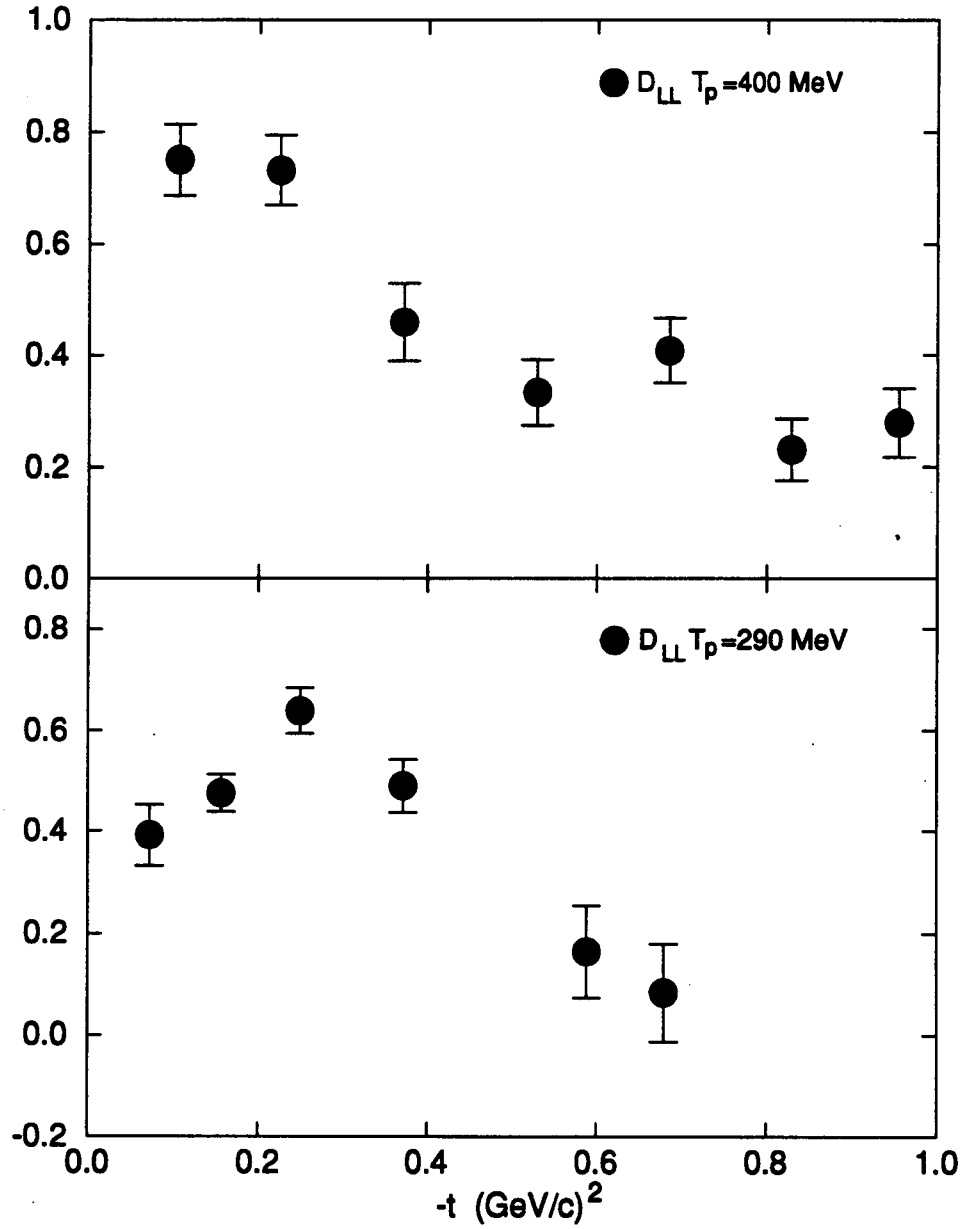

Figure 63. D_{LL}, (T_p=400, 290 MeV)

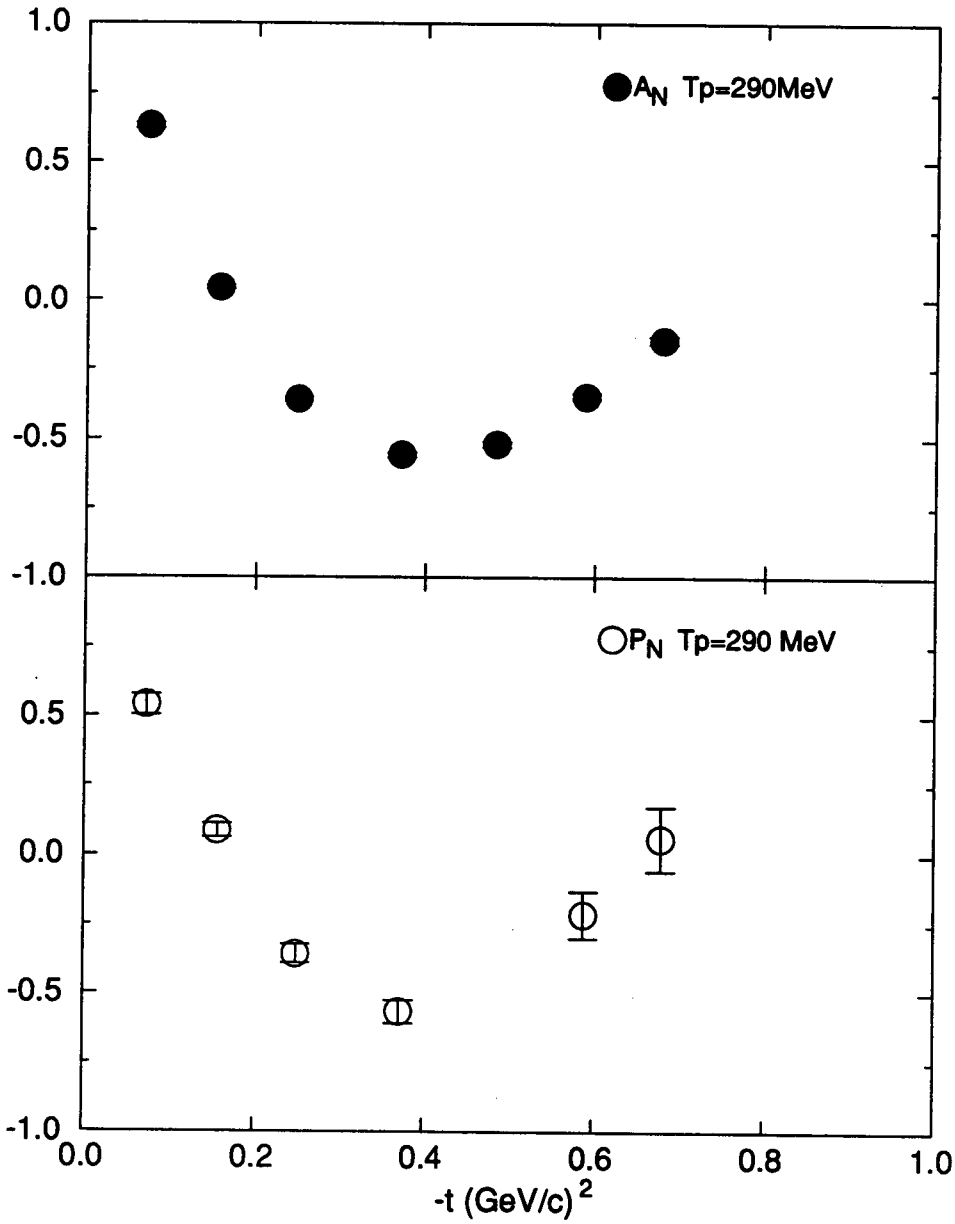

Figure 64. A_N, P_N (T_p=290 MeV)

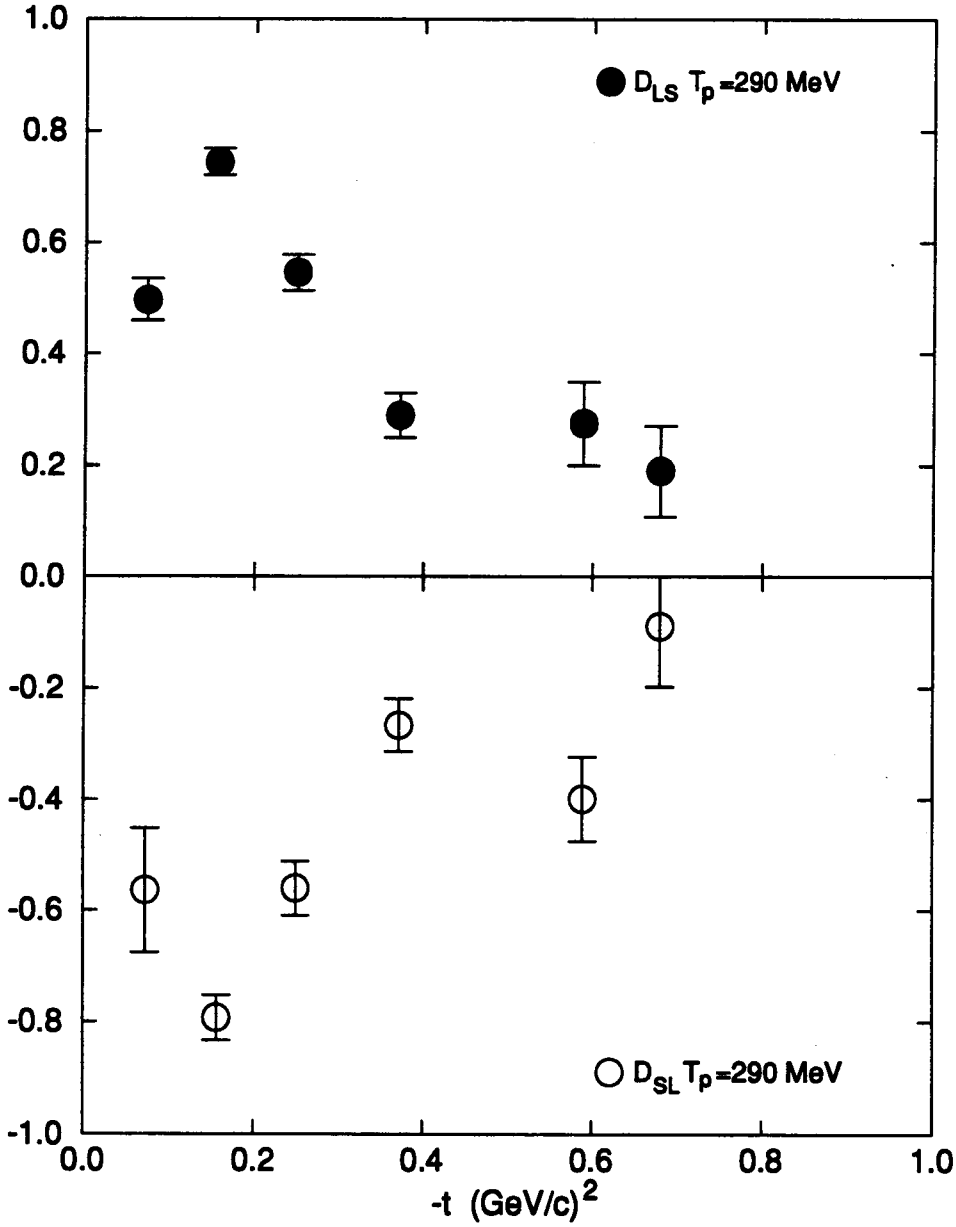

Figure 65. D_{LS}, D_{SL} (T_p=290 MeV)

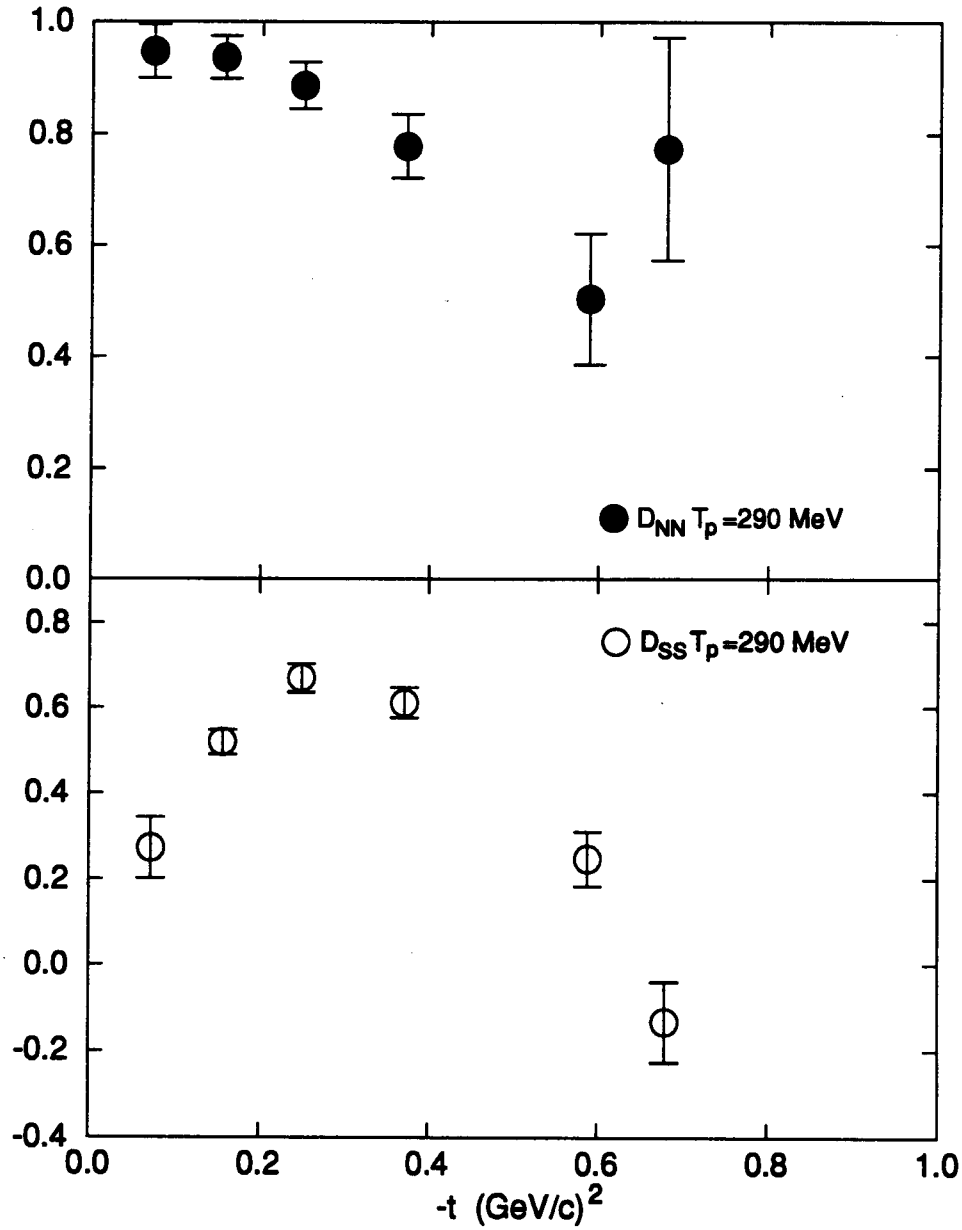

Figure 66. D_{NN}, D_{SS} (T_p=290 MeV)

Table 6. Spin Observables (T_p=400 MeV)

$\theta_{MRS}(^\circ)$	20	30	40	50	60	70	80
$-t(\frac{GeV}{c})^2$	.106	.226	.372	.530	.686	.830	.955
A_N	0.4748	-0.0614	-0.4991	-0.4833	-0.3250	-0.2110	0.0484
$\delta A_{N(stat)}$	0.0154	0.0105	0.0120	0.0109	0.0091	0.0102	0.0098
$\delta A_{N(syst)}$	0.0228	0.0119	0.0169	0.0217	0.0364	0.0626	0.0354
P_N	0.4348	-0.0532	-0.4454	-0.4399	-0.3018	-0.1341	0.0393
$\delta P_{N(stat)}$	0.0344	0.0235	0.0273	0.0376	0.0423	0.0470	0.0563
$\delta P_{N(syst)}$	0.0033	0.0012	0.0046	0.0055	0.0052	0.0032	0.0051
D_{NN}	1.1066	0.9723	0.8173	0.8964	0.6981	0.7964	0.8891
$\delta D_{NN(stat)}$	0.0408	0.0394	0.0440	0.0683	0.0722	0.0759	0.0796
$\delta D_{NN(syst)}$	0.0159	0.0151	0.0140	0.0180	0.0174	0.0209	0.0277
D_{LL}	0.7503	0.7319	0.4592	0.3332	0.4079	0.2313	0.2790
$\delta D_{LL(stat)}$	0.0625	0.0624	0.0699	0.0591	0.0584	0.0552	0.0613
$\delta D_{LL(syst)}$	0.0347	0.0261	0.0161	0.0202	0.0113	0.0077	0.0069
D_{LS}	0.6246	0.6672	0.2582	0.2106	0.3116	0.4963	0.4796
$\delta D_{LS(stat)}$	0.0285	0.0320	0.0402	0.0379	0.0411	0.0421	0.0493
$\delta D_{LS(syst)}$	0.0057	0.0085	0.0080	0.0050	0.0039	0.0038	0.0134
D_{SL}	-0.6711	-0.7853	-0.4262	-0.1856	-0.4163	-0.5439	-0.7517
$\delta D_{SL(stat)}$	0.0622	0.0563	0.0545	0.0649	0.0657	0.0563	0.0907
$\delta D_{SL(syst)}$	0.0351	0.0310	0.0173	0.0100	0.0126	0.0108	0.0159
D_{SS}	0.6100	0.7311	0.7537	0.5541	0.4164	0.3053	0.3546
$\delta D_{SS(stat)}$	0.0294	0.0300	0.0314	0.0417	0.0463	0.0434	0.0733
$\delta D_{SS(syst)}$	0.0157	0.0103	0.0114	0.0049	0.0054	0.0073	0.0100

Table 7. Spin Observables (T_p=290 MeV)

$\theta_{MRS}(^\circ)$	20	30	40	50	60	70	80
$-t(\frac{GeV}{c})^2$	.0734	.157	.250	.372	.484	.589	.680
A_N	0.6304	0.0431	-0.3589	-0.5582	-0.5195	-0.3475	-0.1454
$\delta A_{N(stat)}$	0.0110	0.0081	0.0076	0.0095	0.0116	0.0131	0.0141
$\delta A_{N(syst)}$	0.0182	0.0112	0.0173	0.0208	0.0252	0.0261	0.0358
P_N	0.5393	0.0864	-0.3578	-0.5654		-0.2146	0.0568
$\delta P_{N(stat)}$	0.0378	0.0242	0.0325	0.0412		0.0854	0.1148
$\delta P_{N(syst)}$	0.0064	0.0015	0.0050	0.0090		0.0115	0.0081
D_{NN}	0.9478	0.9373	0.8866	0.7773		0.5025	0.7726
$\delta D_{NN(stat)}$	0.0476	0.0386	0.0418	0.0579		0.1172	0.2008
$\delta D_{NN(syst)}$	0.0174	0.0177	0.0204	0.0195		0.0251	0.0329
D_{LL}	0.3921	0.4752	0.6382	0.4897		0.1639	0.0825
$\delta D_{LL(stat)}$	0.0603	0.0372	0.0448	0.0527		0.0907	0.0953
$\delta D_{LL(syst)}$	0.0330	0.0139	0.0169	0.0188		0.0221	0.0091
D_{LS}	0.4968	0.7440	0.5450	0.2898		0.2749	0.1897
$\delta D_{LS(stat)}$	0.0375	0.0245	0.0317	0.0393		0.0748	0.0815
$\delta D_{LS(syst)}$	0.0158	0.0116	0.0094	0.0067		0.0141	0.0077
D_{SL}	-0.5634	-0.7929	-0.5603	-0.2676		-0.3989	-0.0887
$\delta D_{SL(stat)}$	0.1118	0.0405	0.0477	0.0479		0.0756	0.1092
$\delta D_{SL(syst)}$	0.0423	0.0244	0.0152	0.0152		0.0167	0.0105
D_{SS}	0.2715	0.5192	0.6691	0.6109		0.2468	-0.1321
$\delta D_{SS(stat)}$	0.0703	0.0282	0.0340	0.0356		0.0624	0.0934
$\delta D_{SS(syst)}$	0.0193	0.0123	0.0072	0.0091		0.0088	0.0250

Table 8. Check variable C_{SS}

$\theta_{MRS}(°)$	20	30	40	50	60	70	80
C_{SS}(400MeV)	0.0173	0.0051	-0.0014	-0.0242	0.0216	0.0122	0.0934
$\delta C_{SS_{stat}}$	0.0005	0.0003	0.0013	0.0014	0.0010	0.0004	0.0024
-t (GeV/c)^2	0.1060	0.2256	0.3721	0.5303	0.6865	0.8303	0.9554
C_{SS}(290MeV)	-0.0346	-0.0107	0.0168	0.0064		0.0160	0.0221
$\delta C_{SS_{stat}}$	0.0017	0.0002	0.0004	0.0017		0.0028	0.0094
-t (GeV/c)^2	0.0734	0.1568	0.2599	0.3723		0.5888	0.6803

Table 9. K values for TRI test

$\theta_{MRS}(°)$	20	30	40	50	60	70	80
K(400MeV)	0.3752	0.2960	0.2939	0.4189	0.0768	0.3777	-0.0821
δK_{stat}	0.3816	1.0202	0.1779	0.4680	0.1445	0.2750	0.5187
δK_{syst}	0.2232	0.4610	0.0985	0.2280	0.1219	0.3103	0.3232
-t (GeV/c)^2	0.1060	0.2256	0.3721	0.5303	0.6865	0.8303	0.9554
K(290MeV)	-1.7452	0.6906	0.0097	-0.0323		0.2671	0.8892
δK_{stat}	1.7611	0.5886	0.2943	0.1900		0.1847	0.9355
δK_{syst}	0.6892	0.2655	0.1588	0.1018		0.0589	0.2064
-t (GeV/c)^2	0.0734	0.1568	0.2599	0.3723		0.5888	0.6803

Table 10. Transformation of spin observables to CM system, T_p=400 MeV

$\theta(°)$	20.	30.	40.	50.	60.	70.	80.
$\bar{\theta}(°)$	10.370	15.180	19.530	23.300	26.330	28.510	29.750
$\theta_c(°)$	32.420	48.080	63.100	77.330	90.640	102.930	114.130
χ	16.210	24.040	31.550	38.665	45.320	51.465	57.065
χ'	-5.840	-8.860	-12.020	-15.365	-18.990	-22.955	-27.315
a	0.9553	0.9024	0.8335	0.7529	0.6649	0.5737	0.4831
b	-0.0284	-0.0627	-0.1090	-0.1655	-0.2314	-0.3051	-0.3851
c	0.2777	0.4025	0.5118	0.6024	0.6723	0.7203	0.7457
d	-0.0977	-0.1407	-0.1775	-0.2069	-0.2288	-0.2430	-0.2495
Dss	0.3226	0.2349	0.3700	0.1972	-0.1219	-0.3847	-0.4810
$\delta Dss_{(stat)}$	0.0295	0.0312	0.0351	0.0415	0.0458	0.0446	0.0603
$\delta Dss_{(syst)}$	0.0148	0.0107	0.0106	0.0058	0.0054	0.0056	0.0117
Dll	0.4518	0.2040	0.0367	0.0041	-0.1765	-0.4722	-0.6811
$\delta Dll_{(stat)}$	0.0617	0.0605	0.0643	0.0597	0.0600	0.0538	0.0795
$\delta Dll_{(syst)}$	0.0339	0.0266	0.0160	0.0163	0.0110	0.0085	0.0126
Dls	0.8197	0.9497	0.6354	0.5301	0.4833	0.3947	0.2757
$\delta Dls_{(stat)}$	0.0286	0.0327	0.0393	0.0406	0.0458	0.0448	0.0704
$\delta Dls_{(syst)}$	0.0072	0.0092	0.0094	0.0063	0.0054	0.0064	0.0114
Dsl	-0.8911	-1.0636	-0.6955	-0.4198	-0.5735	-0.4007	-0.4747
$\delta Dsl_{(stat)}$	0.0617	0.0566	0.0576	0.0608	0.0599	0.0536	0.0682
$\delta Dsl_{(syst)}$	0.0348	0.0299	0.0165	0.0143	0.0110	0.0079	0.0102

Table 11. Transformation of spin observables T_p=290 MeV

$\theta(°)$	20	30	40	50	70	80
$\bar{\theta}(°)$	10.530	15.020	19.360	23.130	28.420	29.700
$\theta_c(°)$	31.740	47.130	61.960	76.080	101.670	112.950
χ	15.870	23.565	30.980	38.040	50.835	56.475
χ'	-5.340	-8.545	-11.620	-14.910	-22.415	-26.775
a	0.9577	0.9064	0.8398	0.7611	0.5838	0.4931
b	-0.0254	-0.0594	-0.1037	-0.1586	-0.2956	-0.3755
c	0.2723	0.3954	0.5042	0.5955	0.7168	0.7443
d	-0.0895	-0.1362	-0.1727	-0.2026	-0.2408	-0.2488
Dss	0.0641	0.0402	0.1242	0.1605	-0.1968	-0.2584
$\delta Dss_{(stat)}$	0.0685	0.0277	0.0339	0.0375	0.0718	0.0880
$\delta Dss_{(syst)}$	0.0190	0.0122	0.0080	0.0088	0.0134	0.0140
Dll	0.1708	-0.0147	0.0900	0.0579	-0.3288	-0.0225
$\delta Dll_{(stat)}$	0.0650	0.0373	0.0444	0.0494	0.0794	0.1020
$\delta Dll_{(syst)}$	0.0336	0.0152	0.0155	0.0165	0.0177	0.0129
Dls	0.5696	0.8972	0.8471	0.6399	0.2579	-0.0177
$\delta Dls_{(stat)}$	0.0407	0.0250	0.0325	0.0385	0.0693	0.0928
$\delta Dls_{(syst)}$	0.0156	0.0113	0.0089	0.0083	0.0123	0.0194
Dsl	-0.6576	-0.9322	-0.8510	-0.5722	-0.3274	-0.0006
$\delta Dsl_{(stat)}$	0.1077	0.0393	0.0458	0.0482	0.0823	0.0967
$\delta Dsl_{(syst)}$	0.0413	0.0224	0.0150	0.0158	0.0189	0.0107

Table 12. Calculation:400 MeV, off-shell, Single+Double

$-t(\frac{GeV}{c})^2$	$\frac{d\sigma}{d\Omega}(\frac{mb}{sr})$	A_N	P_N	D_{NN}	D_{SS}	D_{LL}	D_{SL}	D_{LS}
.000	.2100E+02	.0000	.0000	.9996	.9996	.9996	.9996	.9996
.039	.6066E+01	.7553	.7553	.9996	.5444	.5441	.0486	-.0486
.078	.2487E+01	.6538	.6538	.9989	.4458	.4448	-.2190	.2190
.116	.1306E+01	.4206	.4206	.9982	.5462	.5446	-.3520	.3520
.155	.8155E+00	.1747	.1747	.9977	.6906	.6886	-.3450	.3450
.194	.5021E+00	.0249	.0249	.9973	.7811	.7790	-.2440	.2440
.233	.3230E+00	-.1353	-.1353	.9962	.8361	.8332	-.1033	.1033
.272	.2004E+00	-.2598	-.2597	.9949	.8270	.8232	.0273	-.0272
.310	.1283E+00	-.3749	-.3749	.9925	.7615	.7559	.1451	-.1449
.349	.8803E-01	-.4709	-.4708	.9912	.6641	.6578	.2184	-.2184
.388	.5979E-01	-.5346	-.5346	.9894	.5619	.5541	.1911	-.1908
.427	.4516E-01	-.5413	-.5412	.9870	.4396	.4301	.1396	-.1394
.466	.3674E-01	-.5091	-.5085	.9859	.3495	.3394	.0678	-.0673
.505	.3165E-01	-.4431	-.4428	.9854	.3010	.2913	-.0387	.0392
.543	.2849E-01	-.3699	-.3696	.9863	.2976	.2885	-.1183	.1186
.582	.2453E-01	-.3517	-.3517	.9860	.3292	.3202	-.1369	.1371
.621	.2441E-01	-.2771	-.2768	.9860	.3224	.3141	-.2064	.2069
.660	.2058E-01	-.2930	-.2934	.9846	.3623	.3538	-.1988	.1985
.699	.1911E-01	-.2844	-.2841	.9851	.3861	.3785	-.2085	.2087
.737	.1745E-01	-.2708	-.2710	.9854	.3943	.3873	-.2150	.2154
.776	.1654E-01	-.2846	-.2849	.9851	.3883	.3815	-.2175	.2171
.815	.1497E-01	-.2824	-.2821	.9834	.3830	.3766	-.2268	.2275
.854	.1338E-01	-.3170	-.3174	.9821	.3789	.3735	-.2427	.2431
.893	.1363E-01	-.2720	-.2726	.9797	.3300	.3236	-.2654	.2658
.931	.1064E-01	-.3500	-.3505	.9814	.3381	.3348	-.2809	.2812
.970	.1022E-01	-.3211	-.3223	.9752	.2976	.2950	-.3183	.3179
1.009	.9231E-02	-.3209	-.3217	.9712	.2548	.2548	-.3528	.3528

Table 13. Calculation:400 MeV, off-shell, Single

-t $(\frac{GeV}{c})^2$	$\frac{d\sigma}{d\Omega}(\frac{mb}{sr})$	A_N	P_N	D_{NN}	D_{SS}	D_{LL}	D_{SL}	D_{LS}
.000	.2267E+02	.0000	.0000	1.0000	1.0000	1.0000	1.0000	1.0000
.039	.6911E+01	.7509	.7509	1.0000	.5480	.5481	.0456	-.0456
.078	.3150E+01	.6705	.6705	.9999	.4367	.4368	-.2046	.2046
.116	.1779E+01	.4877	.4877	.9998	.5032	.5034	-.3395	.3395
.155	.1143E+01	.2992	.2992	.9997	.6192	.6195	-.3695	.3695
.194	.7204E+00	.1928	.1928	.9996	.7068	.7072	-.3169	.3168
.233	.4819E+00	.0916	.0916	.9994	.7789	.7796	-.2417	.2417
.272	.3143E+00	.0299	.0299	.9992	.8150	.8159	-.1643	.1643
.310	.2071E+00	-.0234	-.0234	.9989	.8347	.8358	-.0898	.0898
.349	.1411E+00	-.0808	-.0808	.9986	.8453	.8468	-.0148	.0148
.388	.9417E-01	-.1167	-.1167	.9982	.8360	.8378	.0357	-.0357
.427	.6485E-01	-.1584	-.1584	.9978	.8224	.8247	.0816	-.0816
.466	.4615E-01	-.2060	-.2060	.9973	.8054	.8081	.1238	-.1238
.505	.3383E-01	-.2448	-.2448	.9968	.7838	.7870	.1472	-.1473
.543	.2564E-01	-.2819	-.2819	.9962	.7620	.7658	.1593	-.1594
.582	.2013E-01	-.3211	-.3211	.9956	.7420	.7464	.1658	-.1659
.621	.1634E-01	-.3613	-.3613	.9950	.7246	.7296	.1676	-.1676
.660	.1373E-01	-.3876	-.3876	.9943	.7125	.7182	.1461	-.1462
.699	.1184E-01	-.4125	-.4125	.9936	.7049	.7113	.1189	-.1190
.737	.1041E-01	-.4356	-.4356	.9928	.7012	.7084	.0864	-.0865
.776	.9305E-02	-.4569	-.4569	.9920	.7007	.7087	.0498	-.0499
.815	.8421E-02	-.4696	-.4696	.9910	.7016	.7106	-.0043	.0042
.854	.7675E-02	-.4781	-.4781	.9899	.7017	.7118	-.0697	.0696
.893	.7025E-02	-.4847	-.4847	.9887	.6988	.7102	-.1427	.1426
.931	.6455E-02	-.4894	-.4894	.9873	.6903	.7030	-.2228	.2227
.970	.5938E-02	-.4920	-.4920	.9860	.6721	.6861	-.3112	.3111
1.009	.5524E-02	-.4859	-.4859	.9845	.6405	.6560	-.4131	.4130

Table 14. Calculation:400 MeV, on-shell, Single+Double

$-t(\frac{GeV}{c})^2$	$\frac{d\sigma}{d\Omega}(\frac{mb}{sr})$	A_N	P_N	D_{NN}	D_{SS}	D_{LL}	D_{SL}	D_{LS}
.000	.2609E+02	.0000	.0000	.9998	.9998	.9998	.9998	.9998
.039	.6874E+01	.7251	.7251	.9996	.5358	.5354	.3039	-.3040
.078	.2496E+01	.7575	.7575	.9990	.2993	.2984	.1101	-.1103
.116	.1137E+01	.6142	.6143	.9978	.2614	.2598	-.0961	.0956
.155	.5611E+00	.3263	.3265	.9948	.3628	.3590	-.2625	.2612
.194	.3165E+00	.1014	.1017	.9938	.4376	.4335	-.2693	.2675
.233	.1771E+00	-.2431	-.2427	.9885	.5335	.5260	-.2068	.2035
.272	.1137E+00	-.4384	-.4379	.9862	.5213	.5130	-.1275	.1230
.310	.7486E-01	-.6412	-.6405	.9799	.4666	.4553	-.0480	.0406
.349	.5556E-01	-.7963	-.7957	.9748	.3900	.3767	.0672	-.0766
.388	.4351E-01	-.8576	-.8570	.9664	.2614	.2454	.0699	-.0831
.427	.3709E-01	-.8480	-.8478	.9648	.1598	.1446	.0869	-.1012
.466	.3226E-01	-.8273	-.8274	.9670	.0818	.0697	.1072	-.1209
.505	.2902E-01	-.7920	-.7924	.9643	-.0292	-.0402	.0905	-.1056
.543	.2712E-01	-.7388	-.7414	.9592	-.1073	-.1177	.0433	-.0604
.582	.2486E-01	-.6692	-.6708	.9602	-.2030	-.2103	.1079	-.1245
.621	.2431E-01	-.6004	-.6033	.9594	-.2451	-.2500	.1556	-.1720
.660	.2466E-01	-.4788	-.4826	.9601	-.2745	-.2760	.2544	-.2697
.699	.3018E-01	-.3421	-.3465	.9595	-.1742	-.1757	.3567	-.3726
.737	.3029E-01	-.2649	-.2683	.9625	-.1797	-.1769	.4783	-.4920
.776	.3163E-01	-.1857	-.1889	.9655	-.1677	-.1628	.5812	-.5927
.815	.3291E-01	-.1535	-.1566	.9695	-.1479	-.1418	.6727	-.6826
.854	.3444E-01	-.1348	-.1372	.9648	-.1174	-.1079	.6939	-.7050
.893	.4092E-01	-.1548	-.1578	.9592	-.0180	-.0052	.6661	-.6777
.931	.3815E-01	-.1258	-.1284	.9692	-.0759	-.0661	.7452	-.7532
.970	.3344E-01	-.1314	-.1329	.9620	-.1150	-.1005	.7586	-.7671
1.009	.3248E-01	-.1176	-.1190	.9569	-.1112	-.0923	.7502	-.7583

Table 15. Calculation:400 MeV, on-shell, Single

$-t$ $(\frac{GeV}{c})^2$	$\frac{d\sigma}{d\Omega}(\frac{mb}{sr})$	A_N	P_N	D_{NN}	D_{SS}	D_{LL}	D_{SL}	D_{LS}
.000	.2650E+02	.0000	.0000	1.0000	1.0000	1.0000	1.0000	1.0000
.039	.7329E+01	.7299	.7299	1.0000	.5245	.5245	.2906	-.2906
.078	.2854E+01	.7543	.7543	1.0000	.2851	.2852	.0966	-.0966
.116	.1398E+01	.6189	.6189	.9999	.2399	.2400	-.1034	.1034
.155	.7968E+00	.4087	.4087	.9999	.3038	.3040	-.2469	.2469
.194	.4648E+00	.2613	.2613	.9998	.3617	.3620	-.2603	.2603
.233	.2912E+00	.0978	.0978	.9997	.4239	.4242	-.2429	.2429
.272	.1840E+00	-.0179	-.0179	.9997	.4336	.4340	-.1917	.1917
.310	.1200E+00	-.1247	-.1247	.9996	.4186	.4190	-.1327	.1327
.349	.8299E-01	-.2386	-.2386	.9996	.4028	.4033	-.0688	.0688
.388	.5871E-01	-.3065	-.3065	.9996	.3362	.3366	-.0194	.0194
.427	.4339E-01	-.3746	-.3746	.9996	.2614	.2618	.0250	-.0250
.466	.3332E-01	-.4414	-.4414	.9996	.1792	.1795	.0634	-.0634
.505	.2605E-01	-.4791	-.4791	.9997	.0379	.0382	.0988	-.0988
.543	.2100E-01	-.4993	-.4993	.9998	-.1349	-.1347	.1364	-.1364
.582	.1773E-01	-.4871	-.4871	.9999	-.3293	-.3292	.2182	-.2182

BIBLIOGRAPHY

[1] J. Arvieux and J. M. Cameron, *Advances in Nuclear Physics* (J. W. Negele and Eric Vogt, Ed.), Plenum, New York, Vol. 18, 151, (1987)

[2] G. H. Berthold, A. Stadler, and H. Zankel, *Phys. Rev. Lett.* Vol. 61, 1077, (1988)

[3] W. Tornow, J. Herdtweck, W. Arnold, and G. Mertens, *Phys. Lett.* Vol. B203, 341, (1988)

[4] Sun Tsu-hsum, *et al. Phys. Rev.* Vol. C31, 515, (1985)

[5] Theoretical calculations for comparison with data of TRIUMF experiment E482, Bradley B. Keister, Carnegie Mellon Univ.

[6] J. G. Rogers *et al.*, *Phys. Rev.* Vol. C22, 22, (1980) and references therein.

[7] P. Doleschall *Nucl. Phys.* Vol. A201, 264, (1973)

[8] R. J. Glauber, in *Lectures in Theoretical Physics* (E. Brittin, Ed.), Interscience, New York, (1959)

[9] R. J. Glauber, in *High Energy Physics and Nuclear Structure* (S. Devons, Ed.), Plenum Press, New York, London, 207, (1970)

[10] W. Czyż, *Adv. Nucl. Phys.* Vol. 4, 61, (1971)

[11] M. Bleszynski *et al.*, *Phys. Lett.* Vol. 106B, 42, (1981)

[12] M. Bleszynski *et al.*, *Phys. Lett.* Vol. 56B, 427, (1975)

[13] K. Gottfried *Ann. Phys* Vol. 66 868, (1971)

[14] G.Alberi, M. Bleszynski and T. Jaroszewicz, *Ann. Phys.* Vol. 142, 299 (1982)

[15] G. Alberi, M. Bleszynski and S. Sntos, *Phys. Lett.* Vol. 92B, 41 (1980)

[16] S. J. Wallace, *Adv. Nucl. Phys.* Vol. 12, 135 (1981), and references therein.

[17] S. A. Gurvitz, Y. Alexander and A. S. Rinat, *Ann. Phys.* Vol. 93, 142 (1975); *Ann. Phys.* Vol. 98, 346 (1976); S. A. Gurvitz, *Phys. Rev.* Vol. C22, 725 (1980)

[18] Z. J. Cao and B. D. Keister, *Phys. Rev.* Vol. C42, 2295, (1990)

[19] A. Rahber *et al.*, *Phys. Lett.* Vol. B194, 338, (1987)

[20] R. Machleidt *Adv. Nucl. Phys.* Vol. 19, (1988)

[21] R. Machleidt, K. Holinde, and C. Elster, *Phys. Reports* Vol. 149, 1, (1987)

[22] M. Betz, T.-S. H. Lee, *Phys. Rev.* Vol. C23, 375, (1981)

[23] T.-S. H. Lee, *Phys. Rev. Lett.* Vol. 50, 1571, (1983)

[24] T.-S. H. Lee, *Phys. Rev.* Vol. C29, 195, (1984), and the citations therein.

[25] Rubin Landau, *Quantum Machanics II – A second Course in Quantum Mechanics*, John Wiley & Sons, Inc., (1990)

[26] Marvin L. Goldberger and Kenneth M. Watson, *Collision Theory*, Wiley New York, (1964)

[27] L. D. Faddeév *Soviet Physics Jetp* Vol. 12, 1014, (1961)

[28] L. D. Faddeév *Mathematical Aspects of the Three-Body Problem in the Quantum Scattering Theory*, (1965)

[29] L. Wolfenstein, *Ann. Rev. Nucl. Sci.*, Vol. 6, 43-76, (1956)

[30] TRIUMF *Medium Resolution Spectrometer (MRS) Manual*, Revision 2.0, 12, (1988)

[31] R. Abegg *et al.*, *Nuclear Instruments and Method* Vol. A273, 43-47, (1988)

[32] R. S. Henderson, *Large Area Horizontal Drift Chambers for A Focal Plane Polarimeter at the TRIUMF Medium Resolution Spectrometer*, TRIUMF

[33] J. D. Seagrave *et al.*, *Charged Particle Cross Sections*, available from the Office of Technical Services, U.S. Dept. of Commerce, Washington, D. C.,

Los Alamos, N.M, (1956)

[34] O. Häusser *et al.*, *Phys. Rev.* Vol. C43, 230, (1991).

[35] L. Wolfenstein and J. Ashkin, *Phys. Rev.* Second Series, Vol. 85, No. 6, 947, (1952)

[36] E. Aprile-Giboni *et al.*, *Nuclear Instruments and Methods* Vol. 215, 147-157, (1983)

[37] Private communications with TRIUMF scientists.

[38] Private communications with Dr. Bradley Keister at Carnegie Mellon Univ.

[39] D. H. Hasell *et al.*, *Phys. Rev.* Vol. C34, 236, (1986), and references therein.

[40] O. Häusser *et al.*, *Nuclear Instruments and Methods* Vol. A254, 67-74, (1987)

Appendix A

Formalism

A.1 Spin Observables Coupled Equations

From the Equation 3.34 in Chapter 3[10] and the polarization precession relation Equation 5.49 in Chapter 5 the following relations can be derived,

$$(1 + P_N A_N)P_{S''} = D_{SS'}P_S + D_{LS'}P_L \quad \text{(A.1)}$$

$$(1 + P_N A_N)P_{N''} = cos(\chi)(D_{NN'}P_N + P_{N'}(\theta)) + sin\chi(D_{SL'}P_S + D_{LS'}P_L) \quad \text{(A.2)}$$

$$(1 + P_N A_N)P_{L''} = -sin(\chi)(D_{NN'}P_N + P_{N'}(\theta)) + cos\chi(D_{SL'}P_S + D_{LS'}P_L). \quad \text{(A.3)}$$

Assume beam polarization1 of two opposite polarities are equal in magnitude,

$$P^{\uparrow}_{S,N,L} = -P^{\downarrow}_{S,N,L} = P_{S,N,L}, \quad \text{(A.4)}$$

then spin observables are solved from Equations A.2, A.3 and A.4,

$$P_{N'}(\theta) = \frac{1}{2\cos(\chi)}[(1 + P_N A_N)P^{\uparrow}_{N''} + (1 - P_N A_N)P^{\downarrow}_{N''}]$$

[10]Note the representation (X, Y, Z) is equivalent to (S, N, L).

$$
\begin{aligned}
D_{SS'} &= \frac{1}{2P_S}[(1+P_NA_N)P^{\uparrow}_{S''}-(1-P_NA_N)P^{\downarrow}_{S''}-2D_{LS'}P_L] \\
D_{SL'} &= \frac{1}{2P_S\sin(\chi)}[(1+P_NA_N)P^{\uparrow}_{N''}-(1-P_NA_N)P^{\downarrow}_{N''})- \\
&\quad 2P_ND_{NN'}\cos(\chi)-2P_LD_{LL'}\sin(\chi)] \\
D_{NN'} &= \frac{1}{2P_N\cos(\chi)}[(1+P_NA_N)P^{\uparrow}_{N''}-(1-P_NA_N)P^{\downarrow}_{N''})- \\
&\quad 2P_SD_{SL'}\cos(\chi)-2P_LD_{LL'}\sin(\chi)] \qquad \text{(A.5)} \\
D_{LL'} &= \frac{1}{2P_L\sin(\chi)}[(1+P_NA_N)P^{\uparrow}_{N''}-(1-P_NA_N)P^{\downarrow}_{N''})- \\
&\quad 2P_ND_{NN'}\cos(\chi)-2P_SD_{SL'}\sin(\chi)] \\
D_{LS'} &= \frac{1}{2P_L}[(1+P_NA_N)P^{\uparrow}_{S''}-(1-P_NA_N)P^{\downarrow}_{S''}-2D_{SS'}P_S] \\
C_{SS} &= (1+P_NA_N)P^{\uparrow}_{S''}+(1-P_NA_N)P^{\downarrow}_{S''}.
\end{aligned}
$$

Then, the spin observables can be calculated in an iterative manner with the order indicated in Table 16, where D_{ij_0} is the first order iteration of D_{ij}.

A.2 Error calculation

For a multi-variable function $y = f(x_1, x_2, \cdots, x_n)$, the experimental errors in x_i $(i = 1, 2, \cdots, n)$, δx_i contributes to the error of y, δy in the following way,

$$
\delta y = \sqrt{\sum_{i=1}^{n}(\frac{\partial f}{\partial x_i}\delta x_i)^2}. \qquad \text{(A.6)}
$$

In the error analysis for the p-d spin observables, the statistical errors were evaluated separately from non-statistical ones. The statistical errors of the beam polarizations and that of the p-d event counts were the main sources that contributed to the statistical errors in the p-d analyzing powers. The non-statistical errors in the analyzing powers were mainly from the uncertainties in the determinations of the p-d event counts. The systematic errors associated with the beam polarizations were omitted.

Table 16. Spin observables determination procedure

Order	polar.	D_{ij}	using	ignore	because
1	L	D_{LS_0}		D_{SS}	$P_S \ll P_L$
2	S	D_{SS}	D_{LS_0}		
3	L	D_{LS}	D_{SS}		
4	S	D_{SL_0}		D_{SS},D_{LL}	P_N,$P_L \ll P_S$
5	N	D_{NN_0}	D_{SL_0}	D_{LL}	$P_L \ll P_N$
6	L	D_{LL}	D_{NN_0},D_{LS_0}		
7	S	D_{SL}	D_{NN_0},D_{LL}		
8	N	D_{NN}	D_{SL},D_{LL}		

The sources of the non-statistical errors of the scattered proton polarizations at the focal plane were mainly the non-statistical errors of the background polarizations and the uncertainties in the p-d event counts. (Section 5.6). The statistical errors were calculated with the definition 5.35.

The sources of errors (statistical and non-statistical) for the spin transfer coefficients and the induced polarizations were mainly the errors associated with the beam polarizations, the p-d analyzing powers, the focal plane polarizations of the scattered protons of the p-d elastic scatterings and other spin transfer coefficients because of their coupled relations A.5.

Appendix B

Carbon Analyzing Power Fit

The p-C analyzing power (A_c) used for the data analysis is a numerical fit from part of some existing analyzing power data [36] which are sets of A_c data of 11 proton energies from 95 to 386 MeV with 5 to 19° polar scattering angle range of 1° interval. The proton energies and the corresponding carbon scatterer thickness are listed in Table 17. The mathematical form for the parameterization is the following empirical formula (fit 1):

$$\begin{aligned} A_c(E_p,\theta_c) &= D(E_p,\theta_c)\alpha(E_p) \\ &\quad \times[\frac{sin(\theta_c)}{1+\beta(E_p)sin^2(\theta_c)+\gamma(E_p)sin^4(\theta_c)} \\ &\quad +\delta(E_p)sin(\theta_c)], \end{aligned} \tag{B.1}$$

where E_p and θ_c are the proton energy and scattering angle respectively.

$D(E_p,\theta_c)$ is an empirical factor for reproducing the sharp drop of A_c toward small angles induced by multiple Coulomb scattering at low energies which has little effect in the proton scattering angular range ($\sim 10° - 20°$) used in the data analysis for this experiment (See Figure 67, 68), and therefore was omitted.

Table 17. Carbon scatterer thickness

T_p (MeV)	95	144	151	179	194	215
t_c (cm)	3	3	7	7	3	7
T_p (MeV)	238	281	311	347	386	
t_c (cm)	3	3	3	3	3	

α, β, γ and δ are energy dependent polynomials of the form:

$$\alpha(E_p) = \alpha_0 + \alpha_1 X + \alpha_2 X^2 + \alpha_3 X^3 + \alpha_4 X^4, \tag{B.2}$$

where $X = (E_p - E_{p_{\text{central}}})/E_{p_{\text{range}}}$ is a dimensionless variable depending on the energy region where the fit is applied.

The A_c fit parameters for fit 1 are listed in Table 18. As a reference, another set of parameters [37] (not used in data analysis) is given as fit 2 in Table 18, which has a mathematical form as,

$$A_c(P_p, \theta_c) = \frac{\alpha'(P_p) P sin(\theta_c)}{1 + \beta'(P_p) P_p sin^2(\theta_c) + \gamma'(P_p) P_p sin^4(\theta_c)} \tag{B.3}$$

α', β' and γ' is proton momentum dependent polynomials:

$$\alpha(P_p)' = \alpha'_0 + \alpha'_1 R + \alpha'_2 R^2 + \alpha'_3 R^3 + \alpha'_4 R^4, \tag{B.4}$$

where P_p is the proton momentum (in $(\text{GeV/c})^2$), and $R = P_p - 0.7$ for proton energy < 400 MeV. Figure 67 and 68 present the two independent fit parameterizations compared with the A_c data.

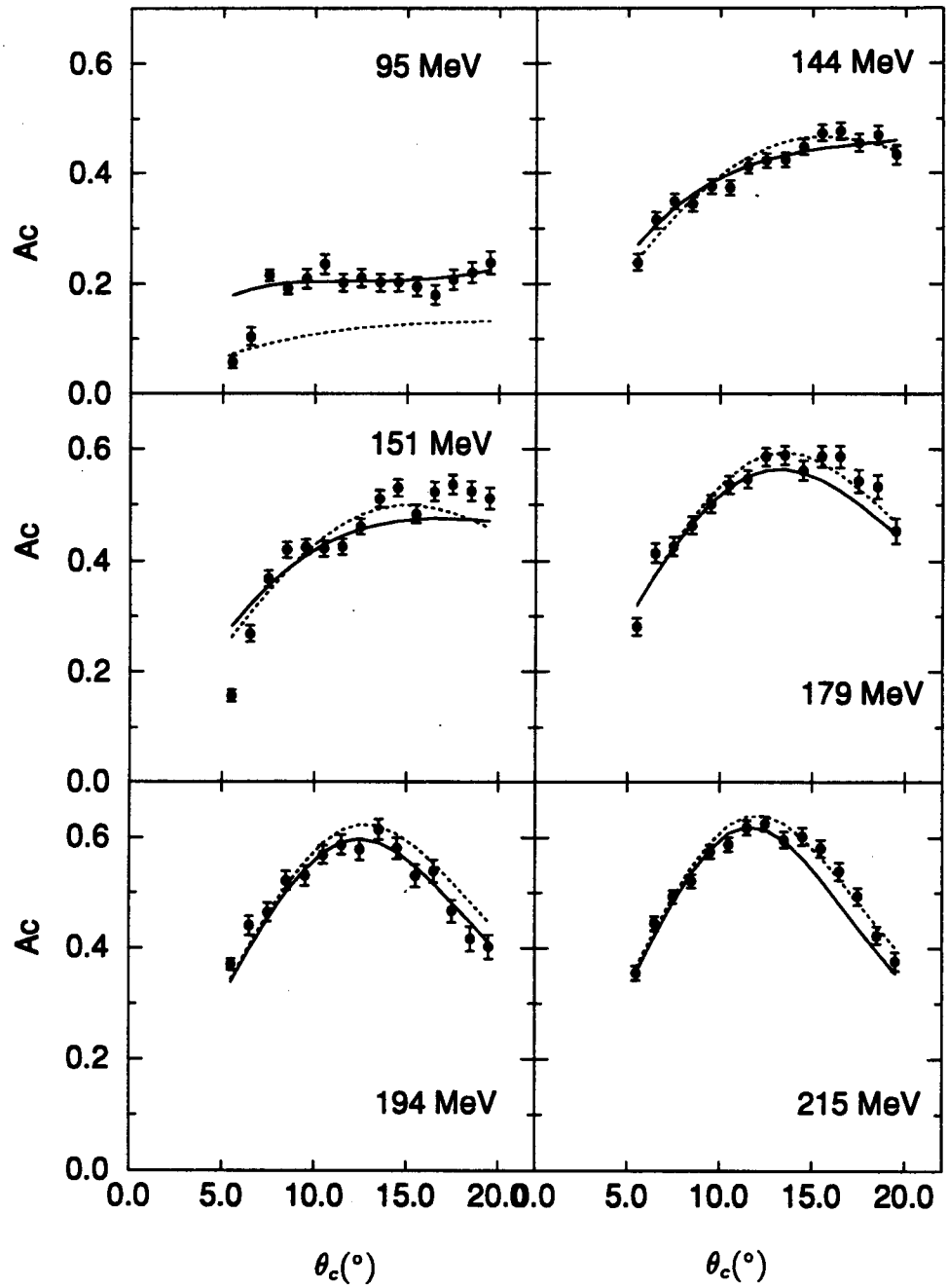

Figure 67. A_c data and parameterizations. The solid dots are the A_c data, the solid lines fit 1, and the dotted lines fit 2., The horizontal axis ($\theta_c(°)$) is the proton scattering angle.

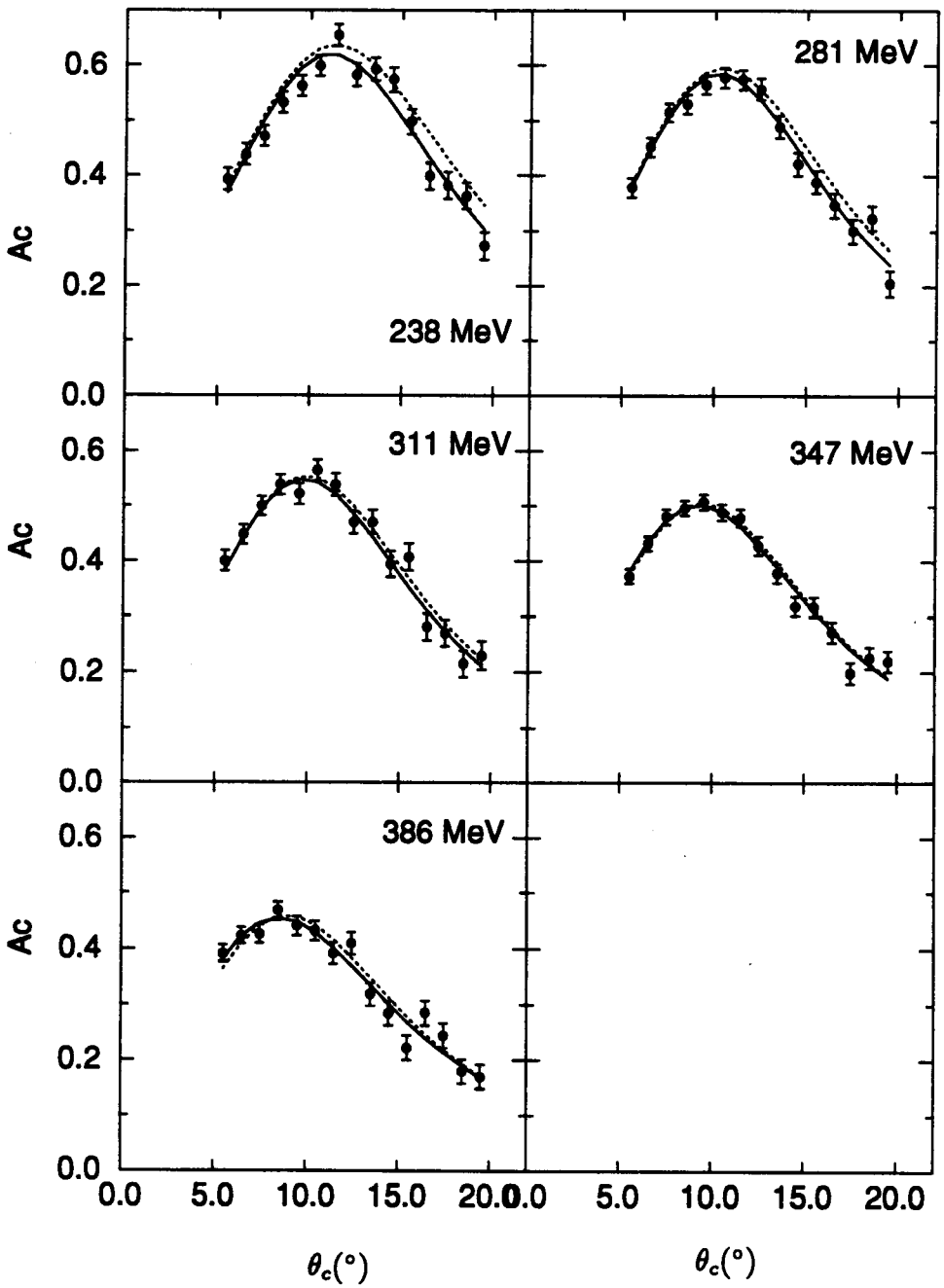

Figure 68. A_c data and parameterizations. (Explanation is the same as in previous Figure.)

Table 18. A_c fit parameters: fit 1 (unprimed), fit 2 (primed)

parameter	i=0	1	2	3	4
α_i	3.6991	.26957	-.0012157	.17072	
β_i	-8.7225	-3.7161	12.869	-2.6088	1.6024
γ_i	351.97	271.44	-113.71	-10.407	20.331
δ_i	0.0	0.0	0.0		
α'_i	5.4771	-4.2906	-25.379	121.15,	-108.37
β'_i	-10.475	-40.17	525.84	-899.29,	1616.6
γ'_i	1052.3	628.51	-13215.	19083.,	-5485.5

Appendix C

Beam and Scattered Proton Polarizations

Some intermediate results of the data analysis are presented in this Appendix. Table 19 and 20 list the 400 and 290 MeV beam polarizations for all three polarization directions for 20 through 80° scattering angles; Table 21 through 33 list the focal plane polarizations of the scattered protons for 400 and 290 MeV incident proton energies and 20 through 80° scattering angles. In the beam polarization representations, P_x ($x = S, N, L$, i.e. sideways, normal, longitudinal) is the x component of the beam polarization; The representation $P^{y}_{x''_z}$ under "Mode" M (=Sideways, Normal, Longitudinal beam polarization mode) is the x ($x = N, S$) component of the focal plane polarization of the type z scattered protons [$z = t$(p-d events and backgrounds), b(backgrounds only), e(p-d events only)] from the beam with M polarization mode and y polarity [$y =$↑(spin up),↓(down),0(off)]; The foot indices (1) and (2) in the error representations stand for "statistic" and "non-statistic", respectively.

Table 19. 400 MeV beam polarizations.

Polar.	P_N	$\delta P_{N(1)}$	$\delta P_{N(2)}$	P_S	$\delta P_{S(1)}$	$\delta P_{S(2)}$	P_L	$\delta P_{L(1)}$	$\delta P_{L(2)}$
20°N	0.717	0.001	0.003	-0.004	0.002	0.002	0.000	0.010	0.010
// S	0.008	0.002	0.004	0.720	0.002	0.015	0.000	0.010	0.010
// L	0.023	0.001	0.007	0.082	0.001	0.003	0.733	0.004	0.005
30°N	0.716	0.001	0.004	0.002	0.001	0.005	0.000	0.010	0.010
// S	-0.013	0.002	0.002	0.719	0.002	0.001	0.000	0.010	0.010
// L	-0.004	0.001	0.002	0.065	0.001	0.006	0.733	0.004	0.005
40°N	0.718	0.001	0.003	0.003	0.001	0.001	0.000	0.010	0.010
// S	-0.001	0.001	0.003	0.717	0.001	0.008	0.000	0.010	0.010
// L	0.000	0.001	0.000	0.029	0.001	0.000	0.733	0.004	0.005
50°N	0.717	0.001	0.000	0.008	0.001	0.001	0.000	0.010	0.010
// S	-0.010	0.001	0.006	0.719	0.001	0.000	0.000	0.010	0.010
// L	-0.025	0.000	0.005	0.051	0.000	0.001	0.733	0.004	0.005
60°N	0.716	0.001	0.001	0.009	0.001	0.001	0.000	0.010	0.010
// S	-0.014	0.001	0.001	0.713	0.001	0.001	0.000	0.010	0.010
// L	-0.009	0.000	0.002	0.030	0.000	0.002	0.733	0.004	0.005
70°N	0.719	0.001	0.001	0.019	0.001	0.003	0.000	0.010	0.010
// S	-0.015	0.001	0.000	0.711	0.001	0.002	0.000	0.010	0.010
// L	-0.025	0.001	0.007	0.044	0.001	0.001	0.733	0.004	0.005
80°N	0.706	0.000	0.001	0.006	0.000	0.000	0.000	0.010	0.010
// S	-0.007	0.000	0.000	0.710	0.000	0.003	0.000	0.010	0.010
// L	-0.025	0.000	0.000	0.045	0.000	0.001	0.733	0.004	0.005

Table 20. 290 MeV beam polarizations.

Polar.	P_N	$\delta P_{N(1)}$	$\delta P_{N(2)}$	P_S	$\delta P_{S(1)}$	$\delta P_{S(2)}$	P_L	$\delta P_{L(1)}$	$\delta P_{L(2)}$
20°N	0.754	0.005	0.006	0.031	0.005	0.000	0.000	0.010	0.010
// S	-0.010	0.005	0.012	0.722	0.005	0.047	0.000	0.010	0.010
// L	-0.003	0.007	0.012	0.001	0.007	0.037	0.729	0.001	0.011
30°N	0.781	0.002	0.004	0.040	0.002	0.004	0.000	0.010	0.010
// S	-0.016	0.003	0.007	0.770	0.003	0.011	0.000	0.010	0.010
// L	-0.006	0.003	0.003	0.005	0.003	0.004	0.729	0.001	0.011
40°N	0.809	0.002	0.002	0.033	0.002	0.009	0.000	0.010	0.010
// S	-0.009	0.002	0.004	0.783	0.002	0.002	0.000	0.010	0.010
// L	-0.001	0.002	0.003	0.005	0.002	0.002	0.729	0.001	0.011
50°N	0.808	0.002	0.005	0.026	0.002	0.002	0.000	0.010	0.010
// S	-0.024	0.001	0.007	0.775	0.001	0.009	0.000	0.010	0.010
// L	-0.007	0.002	0.005	0.006	0.002	0.004	0.729	0.001	0.011
70°N	0.729	0.001	0.002	0.023	0.001	0.001	0.000	0.010	0.010
// S	-0.018	0.001	0.001	0.775	0.001	0.012	0.000	0.010	0.010
// L	-0.003	0.001	0.001	-0.016	0.001	0.002	0.729	0.001	0.011
80°N	0.731	0.001	0.001	0.025	0.001	0.002	0.000	0.010	0.010
// S	-0.026	0.000	0.001	0.757	0.000	0.015	0.000	0.010	0.010
// L	-0.003	0.000	0.000	-0.015	0.000	0.001	0.729	0.001	0.011

Table 21. 400 MeV 20° focal plane polarizations.

Mode	Normal			Sideways			Longitudinal		
Polar.	P	$\delta P_{(1)}$	$\delta P_{(2)}$	P	$\delta P_{(1)}$	$\delta P_{(2)}$	P	$\delta P_{(1)}$	$\delta P_{(2)}$
$P^{\uparrow}_{N''_t}$	-0.883	0.032		-0.603	0.029		-0.183	0.028	
$P^{\uparrow}_{N''_b}$	-0.712	0.176		-0.650	0.156		-0.476	0.181	
$P^{\uparrow}_{N''_e}$	-0.887	0.033	0.000	-0.602	0.030	0.000	-0.180	0.028	0.001
$P^{\uparrow}_{S''_t}$	0.051	0.032		0.470	0.029		0.486	0.028	
$P^{\uparrow}_{S''_b}$	0.014	0.176		0.326	0.156		0.286	0.181	
$P^{\uparrow}_{S''_e}$	0.052	0.033	0.000	0.472	0.030	0.000	0.488	0.028	0.001
$P^{\downarrow}_{N''_t}$	0.336	0.040		-0.149	0.026		-0.590	0.029	
$P^{\downarrow}_{N''_b}$	0.309	0.239		-0.090	0.135		-0.446	0.197	
$P^{\downarrow}_{N''_e}$	0.337	0.041	0.000	-0.150	0.027	0.000	-0.591	0.030	0.000
$P^{\downarrow}_{S''_t}$	-0.074	0.040		-0.406	0.026		-0.524	0.029	
$P^{\downarrow}_{S''_b}$	0.094	0.239		-0.420	0.135		-0.172	0.197	
$P^{\downarrow}_{S''_e}$	-0.077	0.041	0.000	-0.406	0.027	0.000	-0.528	0.030	0.001
$P^{0}_{N''_t}$	-0.469	0.058		-0.374	0.051		-0.431	0.051	
$P^{0}_{N''_b}$	-0.677	0.310		-0.749	0.313		0.058	0.374	
$P^{0}_{N''_e}$	-0.466	0.059	0.001	-0.370	0.052	0.001	-0.436	0.051	0.001
$P^{0}_{S''_t}$	-0.038	0.058		0.073	0.051		0.043	0.051	
$P^{0}_{S''_b}$	-0.219	0.310		0.152	0.313		0.123	0.374	
$P^{0}_{S''_e}$	-0.035	0.059	0.001	0.073	0.052	0.000	0.043	0.051	0.000

Table 22. 400 MeV 30° focal plane polarizations.

Mode	Normal			Sideways			Longitudinal		
Polar.	P	$\delta P_{(1)}$	$\delta P_{(2)}$	P	$\delta P_{(1)}$	$\delta P_{(2)}$	P	$\delta P_{(1)}$	$\delta P_{(2)}$
$P^{\uparrow}_{N''_t}$	-0.579	0.033		-0.222	0.028		0.293	0.031	
$P^{\uparrow}_{N''_b}$	-0.611	0.121		-0.090	0.128		0.279	0.143	
$P^{\uparrow}_{N''_e}$	-0.578	0.034	0.000	-0.226	0.029	0.001	0.294	0.033	0.000
$P^{\uparrow}_{S''_t}$	-0.035	0.033		0.532	0.028		0.531	0.031	
$P^{\uparrow}_{S''_b}$	-0.151	0.121		0.443	0.128		0.192	0.143	
$P^{\uparrow}_{S''_e}$	-0.030	0.034	0.001	0.535	0.029	0.001	0.545	0.033	0.004
$P^{\downarrow}_{N''_t}$	0.611	0.032		0.317	0.027		-0.219	0.031	
$P^{\downarrow}_{N''_b}$	0.379	0.120		0.002	0.126		-0.446	0.144	
$P^{\downarrow}_{N''_e}$	0.620	0.033	0.002	0.327	0.028	0.003	-0.210	0.032	0.003
$P^{\downarrow}_{S''_t}$	0.030	0.032		-0.512	0.027		-0.529	0.031	
$P^{\downarrow}_{S''_b}$	0.027	0.120		-0.391	0.126		-0.541	0.144	
$P^{\downarrow}_{S''_e}$	0.030	0.033	0.000	-0.516	0.028	0.001	-0.529	0.032	0.000
$P^{0}_{N''_t}$	-0.012	0.054		0.045	0.052		0.097	0.053	
$P^{0}_{N''_b}$	0.560	0.213		0.220	0.242		-0.255	0.261	
$P^{0}_{N''_e}$	-0.034	0.057	0.004	0.041	0.054	0.001	0.111	0.056	0.005
$P^{0}_{S''_t}$	-0.005	0.054		0.077	0.052		-0.028	0.053	
$P^{0}_{S''_b}$	-0.004	0.213		0.235	0.242		0.128	0.261	
$P^{0}_{S''_e}$	-0.005	0.057	0.000	0.073	0.054	0.001	-0.034	0.056	0.002

Table 23. 400 MeV 40° focal plane polarizations.

Mode	Normal			Sideways			Longitudinal		
Polar.	P	$\delta P_{(1)}$	$\delta P_{(2)}$	P	$\delta P_{(1)}$	$\delta P_{(2)}$	P	$\delta P_{(1)}$	$\delta P_{(2)}$
$P^{\uparrow}_{N''_t}$	-0.139	0.038		0.170	0.028		0.513	0.036	
$P^{\uparrow}_{N''_b}$	-0.133	0.089		-0.014	0.075		0.360	0.092	
$P^{\uparrow}_{N''_e}$	-0.140	0.043	0.000	0.185	0.031	0.004	0.533	0.042	0.007
$P^{\uparrow}_{S''_t}$	-0.014	0.038		0.514	0.028		0.233	0.036	
$P^{\uparrow}_{S''_b}$	-0.074	0.089		0.306	0.075		0.179	0.092	
$P^{\uparrow}_{S''_e}$	-0.008	0.043	0.002	0.531	0.031	0.005	0.240	0.042	0.003
$P^{\downarrow}_{N''_t}$	0.646	0.029		0.519	0.029		0.154	0.035	
$P^{\downarrow}_{N''_b}$	0.712	0.086		0.281	0.081		0.113	0.091	
$P^{\downarrow}_{N''_e}$	0.642	0.032	0.001	0.536	0.032	0.005	0.159	0.041	0.002
$P^{\downarrow}_{S''_t}$	0.014	0.029		-0.523	0.029		-0.213	0.035	
$P^{\downarrow}_{S''_b}$	0.039	0.086		-0.159	0.081		-0.443	0.091	
$P^{\downarrow}_{S''_e}$	0.012	0.032	0.000	-0.550	0.032	0.008	-0.183	0.041	0.011
$P^{0}_{N''_t}$	0.426	0.056		0.364	0.051		0.435	0.043	
$P^{0}_{N''_b}$	0.163	0.146		0.295	0.144		0.121	0.109	
$P^{0}_{N''_e}$	0.445	0.061	0.004	0.370	0.056	0.002	0.473	0.050	0.012
$P^{0}_{S''_t}$	0.143	0.056		-0.026	0.051		0.031	0.043	
$P^{0}_{S''_b}$	-0.132	0.146		0.048	0.144		0.216	0.109	
$P^{0}_{S''_e}$	0.163	0.061	0.004	-0.031	0.056	0.002	0.008	0.050	0.007

Table 24. 400 MeV 50° focal plane polarizations.

Mode	Normal			Sideways			Longitudinal		
Polar.	P	$\delta P_{(1)}$	$\delta P_{(2)}$	P	$\delta P_{(1)}$	$\delta P_{(2)}$	P	$\delta P_{(1)}$	$\delta P_{(2)}$
$P^{\uparrow}_{N''_t}$	-0.140	0.054		0.234	0.037		0.412	0.032	
$P^{\uparrow}_{N''_b}$	-0.171	0.101		0.182	0.087		0.099	0.069	
$P^{\uparrow}_{N''_e}$	-0.135	0.066	0.001	0.239	0.042	0.001	0.465	0.039	0.016
$P^{\uparrow}_{S''_t}$	0.082	0.054		0.335	0.037		0.174	0.032	
$P^{\uparrow}_{S''_b}$	0.093	0.101		0.208	0.087		0.052	0.069	
$P^{\uparrow}_{S''_e}$	0.080	0.066	0.000	0.348	0.042	0.003	0.195	0.039	0.006
$P^{\downarrow}_{N''_t}$	0.643	0.041		0.389	0.036		0.117	0.033	
$P^{\downarrow}_{N''_b}$	0.378	0.102		0.300	0.083		0.004	0.071	
$P^{\downarrow}_{N''_e}$	0.668	0.045	0.004	0.400	0.042	0.002	0.135	0.039	0.005
$P^{\downarrow}_{S''_t}$	0.067	0.041		-0.431	0.036		-0.161	0.033	
$P^{\downarrow}_{S''_b}$	0.312	0.102		-0.286	0.083		-0.101	0.071	
$P^{\downarrow}_{S''_e}$	0.044	0.045	0.004	-0.449	0.042	0.004	-0.170	0.039	0.003
$P^{0}_{N''_t}$	0.205	0.078		0.325	0.069		0.316	0.049	
$P^{0}_{N''_b}$	0.135	0.166		0.107	0.163		0.078	0.107	
$P^{0}_{N''_e}$	0.213	0.088	0.002	0.348	0.078	0.005	0.356	0.060	0.011
$P^{0}_{S''_t}$	-0.021	0.078		-0.046	0.069		-0.043	0.049	
$P^{0}_{S''_b}$	0.147	0.166		-0.145	0.163		-0.019	0.107	
$P^{0}_{S''_e}$	-0.039	0.088	0.004	-0.036	0.078	0.002	-0.047	0.060	0.001

Table 25. 400 MeV 60° focal plane polarizations.

Mode	Normal			Sideways			Longitudinal		
Polar.	P	$\delta P_{(1)}$	$\delta P_{(2)}$	P	$\delta P_{(1)}$	$\delta P_{(2)}$	P	$\delta P_{(1)}$	$\delta P_{(2)}$
$P^{\uparrow}_{N''_t}$	-0.199	0.049		0.006	0.042		0.389	0.038	
$P^{\uparrow}_{N''_b}$	-0.210	0.096		-0.178	0.145		0.120	0.114	
$P^{\uparrow}_{N''_e}$	-0.197	0.061	0.001	0.018	0.046	0.004	0.416	0.043	0.008
$P^{\uparrow}_{S''_t}$	0.000	0.049		0.328	0.042		0.225	0.038	
$P^{\uparrow}_{S''_b}$	-0.098	0.096		0.176	0.145		0.326	0.114	
$P^{\uparrow}_{S''_e}$	0.019	0.061	0.009	0.339	0.046	0.004	0.215	0.043	0.003
$P^{\downarrow}_{N''_t}$	0.442	0.039		0.407	0.042		0.007	0.037	
$P^{\downarrow}_{N''_b}$	0.324	0.090		0.161	0.143		0.041	0.102	
$P^{\downarrow}_{N''_e}$	0.457	0.046	0.006	0.425	0.047	0.006	0.004	0.042	0.001
$P^{\downarrow}_{S''_t}$	-0.002	0.039		-0.250	0.042		-0.255	0.037	
$P^{\downarrow}_{S''_b}$	-0.018	0.090		-0.186	0.143		-0.138	0.102	
$P^{\downarrow}_{S''_e}$	0.000	0.046	0.001	-0.255	0.047	0.002	-0.267	0.042	0.003
$P^{0}_{N''_t}$	0.212	0.082		0.147	0.068		0.283	0.063	
$P^{0}_{N''_b}$	-0.036	0.197		0.377	0.228		0.162	0.166	
$P^{0}_{N''_e}$	0.243	0.096	0.011	0.129	0.075	0.007	0.297	0.073	0.004
$P^{0}_{S''_t}$	0.102	0.082		0.013	0.068		0.130	0.063	
$P^{0}_{S''_b}$	0.245	0.197		0.336	0.228		-0.072	0.166	
$P^{0}_{S''_e}$	0.084	0.096	0.007	-0.012	0.075	0.009	0.154	0.073	0.006

Table 26. 400 MeV 70° focal plane polarizations.

Mode	Normal			Sideways			Longitudinal		
Polar.	P	$\delta P_{(1)}$	$\delta P_{(2)}$	P	$\delta P_{(1)}$	$\delta P_{(2)}$	P	$\delta P_{(1)}$	$\delta P_{(2)}$
$P^{\uparrow}_{N''_t}$	-0.262	0.048		-0.163	0.039		0.198	0.038	
$P^{\uparrow}_{N''_b}$	-0.307	0.149		-0.379	0.118		0.287	0.098	
$P^{\uparrow}_{N''_e}$	-0.258	0.053	0.001	-0.146	0.043	0.004	0.189	0.043	0.003
$P^{\uparrow}_{S''_t}$	-0.029	0.048		0.242	0.039		0.387	0.038	
$P^{\uparrow}_{S''_b}$	-0.121	0.149		0.259	0.118		0.340	0.098	
$P^{\uparrow}_{S''_e}$	-0.022	0.053	0.002	0.241	0.043	0.000	0.392	0.043	0.002
$P^{\downarrow}_{N''_t}$	0.456	0.043		0.416	0.039		-0.051	0.038	
$P^{\downarrow}_{N''_b}$	0.308	0.150		0.263	0.116		0.018	0.096	
$P^{\downarrow}_{N''_e}$	0.467	0.047	0.003	0.429	0.043	0.003	-0.059	0.044	0.002
$P^{\downarrow}_{S''_t}$	0.013	0.043		-0.199	0.039		-0.367	0.038	
$P^{\downarrow}_{S''_b}$	-0.179	0.150		-0.264	0.116		-0.402	0.096	
$P^{\downarrow}_{S''_e}$	0.027	0.047	0.004	-0.193	0.043	0.001	-0.362	0.044	0.001
$P^{0}_{N''_t}$	0.137	0.085		0.153	0.067		0.170	0.063	
$P^{0}_{N''_b}$	0.365	0.307		-0.006	0.213		0.160	0.166	
$P^{0}_{N''_e}$	0.122	0.093	0.010	0.167	0.075	0.004	0.171	0.073	0.001
$P^{0}_{S''_t}$	-0.095	0.085		0.150	0.067		0.100	0.063	
$P^{0}_{S''_b}$	0.056	0.307		0.118	0.213		-0.215	0.166	
$P^{0}_{S''_e}$	-0.105	0.093	0.006	0.153	0.075	0.001	0.138	0.073	0.016

Table 27. 400 MeV 80° focal plane polarizations.

Mode	Normal			Sideways			Longitudinal		
Polar.	P	$\delta P_{(1)}$	$\delta P_{(2)}$	P	$\delta P_{(1)}$	$\delta P_{(2)}$	P	$\delta P_{(1)}$	$\delta P_{(2)}$
$P^{\uparrow}_{N''_t}$	-0.345	0.039		-0.399	0.055		0.124	0.043	
$P^{\uparrow}_{N''_b}$	-0.111	0.129		-0.287	0.158		0.177	0.119	
$P^{\uparrow}_{N''_e}$	-0.371	0.046	0.010	-0.419	0.071	0.005	0.116	0.051	0.002
$P^{\uparrow}_{S''_t}$	0.107	0.039		0.419	0.055		0.358	0.043	
$P^{\uparrow}_{S''_b}$	0.276	0.129		0.304	0.158		0.279	0.119	
$P^{\uparrow}_{S''_e}$	0.088	0.046	0.007	0.439	0.071	0.005	0.369	0.051	0.004
$P^{\downarrow}_{N''_t}$	0.355	0.042		0.390	0.056		-0.203	0.042	
$P^{\downarrow}_{N''_b}$	0.108	0.129		0.194	0.150		-0.334	0.108	
$P^{\downarrow}_{N''_e}$	0.382	0.048	0.010	0.433	0.076	0.012	-0.185	0.050	0.007
$P^{\downarrow}_{S''_t}$	0.120	0.042		-0.035	0.056		-0.317	0.042	
$P^{\downarrow}_{S''_b}$	0.232	0.129		0.105	0.150		0.050	0.108	
$P^{\downarrow}_{S''_e}$	0.108	0.048	0.004	-0.065	0.076	0.008	-0.366	0.050	0.019
$P^{0}_{N''_t}$	-0.039	0.072		-0.034	0.099		0.033	0.072	
$P^{0}_{N''_b}$	-0.043	0.239		-0.102	0.293		-0.196	0.185	
$P^{0}_{N''_e}$	-0.039	0.090	0.000	-0.020	0.134	0.005	0.068	0.088	0.020
$P^{0}_{S''_t}$	-0.024	0.072		-0.071	0.099		-0.034	0.072	
$P^{0}_{S''_b}$	0.227	0.239		0.412	0.293		-0.243	0.185	
$P^{0}_{S''_e}$	-0.060	0.090	0.016	-0.171	0.134	0.036	-0.001	0.088	0.019

Table 28. 290 MeV 20° focal plane polarizations.

Mode	Normal			Sideways			Longitudinal		
Polar.	P	$\delta P_{(1)}$	$\delta P_{(2)}$	P	$\delta P_{(1)}$	$\delta P_{(2)}$	P	$\delta P_{(1)}$	$\delta P_{(2)}$
$P^{\uparrow}_{N''_t}$	-0.668	0.026		-0.653	0.051		-0.277	0.030	
$P^{\uparrow}_{N''_b}$	-0.677	0.056		-0.783	0.106		-0.137	0.065	
$P^{\uparrow}_{N''_e}$	-0.666	0.033	0.000	-0.625	0.066	0.006	-0.304	0.038	0.006
$P^{\uparrow}_{S''_t}$	0.005	0.026		0.152	0.051		0.415	0.030	
$P^{\uparrow}_{S''_b}$	0.000	0.056		0.269	0.106		0.420	0.065	
$P^{\uparrow}_{S''_e}$	0.007	0.033	0.000	0.128	0.066	0.006	0.414	0.038	0.000
$P^{\downarrow}_{N''_t}$	0.288	0.037		-0.148	0.061		-0.650	0.031	
$P^{\downarrow}_{N''_b}$	0.282	0.077		-0.265	0.122		-0.572	0.066	
$P^{\downarrow}_{N''_e}$	0.289	0.050	0.000	-0.125	0.077	0.005	-0.665	0.039	0.003
$P^{\downarrow}_{S''_t}$	0.015	0.037		-0.276	0.061		-0.315	0.031	
$P^{\downarrow}_{S''_b}$	0.092	0.077		-0.338	0.122		-0.338	0.066	
$P^{\downarrow}_{S''_e}$	-0.004	0.050	0.004	-0.263	0.077	0.002	-0.311	0.039	0.001
$P^{0}_{N''_t}$	-0.510	0.042		-0.481	0.094		-0.488	0.055	
$P^{0}_{N''_b}$	-0.311	0.087		-0.450	0.207		-0.470	0.120	
$P^{0}_{N''_e}$	-0.550	0.054	0.008	-0.487	0.117	0.002	-0.492	0.069	0.001
$P^{0}_{S''_t}$	-0.027	0.042		-0.086	0.094		-0.024	0.055	
$P^{0}_{S''_b}$	0.046	0.087		-0.081	0.207		-0.152	0.120	
$P^{0}_{S''_e}$	-0.042	0.054	0.003	-0.086	0.117	0.000	-0.001	0.069	0.006

Table 29. 290 MeV 30° focal plane polarizations.

Mode	Normal			Sideways			Longitudinal		
Polar.	P	$\delta P_{(1)}$	$\delta P_{(2)}$	P	$\delta P_{(1)}$	$\delta P_{(2)}$	P	$\delta P_{(1)}$	$\delta P_{(2)}$
$P^{\uparrow}_{N''_t}$	-0.586	0.029		-0.482	0.028		0.185	0.024	
$P^{\uparrow}_{N''_b}$	-0.763	0.167		-0.273	0.156		0.390	0.128	
$P^{\uparrow}_{N''_e}$	-0.581	0.030	0.002	-0.491	0.029	0.002	0.179	0.025	0.002
$P^{\uparrow}_{S''_t}$	-0.037	0.029		0.380	0.028		0.595	0.024	
$P^{\uparrow}_{S''_b}$	0.303	0.167		0.413	0.156		0.506	0.128	
$P^{\uparrow}_{S''_e}$	-0.046	0.030	0.003	0.378	0.029	0.000	0.598	0.025	0.001
$P^{\downarrow}_{N''_t}$	0.554	0.031		0.296	0.026		-0.285	0.024	
$P^{\downarrow}_{N''_b}$	0.506	0.172		0.267	0.152		-0.322	0.131	
$P^{\downarrow}_{N''_e}$	0.555	0.032	0.001	0.297	0.028	0.000	-0.284	0.025	0.000
$P^{\downarrow}_{S''_t}$	0.029	0.031		-0.424	0.026		-0.495	0.024	
$P^{\downarrow}_{S''_b}$	-0.093	0.172		-0.492	0.152		-0.592	0.131	
$P^{\downarrow}_{S''_e}$	0.032	0.032	0.001	-0.421	0.028	0.001	-0.492	0.025	0.001
$P^{0}_{N''_t}$	-0.041	0.048		-0.044	0.050		-0.042	0.055	
$P^{0}_{N''_b}$	-0.405	0.274		-0.237	0.293		0.469	0.330	
$P^{0}_{N''_e}$	-0.032	0.049	0.004	-0.036	0.053	0.002	-0.065	0.060	0.006
$P^{0}_{S''_t}$	-0.085	0.048		-0.043	0.050		-0.073	0.055	
$P^{0}_{S''_b}$	0.443	0.274		-0.559	0.293		0.485	0.330	
$P^{0}_{S''_e}$	-0.098	0.049	0.005	-0.021	0.053	0.006	-0.098	0.060	0.006

Table 30. 290 MeV 40° focal plane polarizations.

Mode	Normal			Sideways			Longitudinal		
Polar.	P	$\delta P_{(1)}$	$\delta P_{(2)}$	P	$\delta P_{(1)}$	$\delta P_{(2)}$	P	$\delta P_{(1)}$	$\delta P_{(2)}$
$P^{\uparrow}_{N''_t}$	-0.306	0.034		-0.067	0.032		0.545	0.030	
$P^{\uparrow}_{N''_b}$	-0.402	0.124		-0.195	0.103		0.238	0.096	
$P^{\uparrow}_{N''_e}$	-0.302	0.036	0.001	-0.054	0.037	0.005	0.563	0.033	0.005
$P^{\uparrow}_{S''_t}$	0.002	0.034		0.556	0.032		0.411	0.030	
$P^{\uparrow}_{S''_b}$	-0.184	0.124		0.556	0.103		0.070	0.096	
$P^{\uparrow}_{S''_e}$	0.012	0.036	0.003	0.556	0.037	0.000	0.431	0.033	0.006
$P^{\downarrow}_{N''_t}$	0.626	0.029		0.546	0.033		-0.100	0.030	
$P^{\downarrow}_{N''_b}$	0.230	0.126		0.423	0.103		-0.228	0.098	
$P^{\downarrow}_{N''_e}$	0.641	0.030	0.004	0.556	0.036	0.003	-0.092	0.033	0.002
$P^{\downarrow}_{S''_t}$	-0.036	0.029		-0.490	0.033		-0.368	0.030	
$P^{\downarrow}_{S''_b}$	-0.188	0.126		-0.462	0.103		-0.336	0.098	
$P^{\downarrow}_{S''_e}$	-0.030	0.030	0.002	-0.492	0.036	0.001	-0.370	0.033	0.001
$P^{0}_{N''_t}$	0.212	0.057		0.269	0.056		0.215	0.055	
$P^{0}_{N''_b}$	-0.396	0.220		-0.005	0.181		0.331	0.175	
$P^{0}_{N''_e}$	0.239	0.060	0.013	0.288	0.061	0.006	0.208	0.059	0.002
$P^{0}_{S''_t}$	0.003	0.057		-0.010	0.056		0.053	0.055	
$P^{0}_{S''_b}$	0.214	0.220		-0.065	0.181		0.098	0.175	
$P^{0}_{S''_e}$	-0.006	0.060	0.004	-0.006	0.061	0.001	0.050	0.059	0.001

Table 31. 290 MeV 50° focal plane polarizations.

Mode	Normal			Sideways			Longitudinal		
Polar.	P	$\delta P_{(1)}$	$\delta P_{(2)}$	P	$\delta P_{(1)}$	$\delta P_{(2)}$	P	$\delta P_{(1)}$	$\delta P_{(2)}$
$P^{\uparrow}_{N''_t}$	-0.087	0.055		0.208	0.034		0.605	0.037	
$P^{\uparrow}_{N''_b}$	-0.164	0.145		0.055	0.082		0.235	0.085	
$P^{\uparrow}_{N''_e}$	-0.080	0.061	0.002	0.228	0.040	0.007	0.643	0.041	0.015
$P^{\uparrow}_{S''_t}$	0.181	0.055		0.467	0.034		0.204	0.037	
$P^{\uparrow}_{S''_b}$	0.107	0.145		0.370	0.082		0.102	0.085	
$P^{\uparrow}_{S''_e}$	0.187	0.061	0.002	0.480	0.040	0.005	0.214	0.041	0.004
$P^{\downarrow}_{N''_t}$	0.547	0.034		0.484	0.032		0.090	0.035	
$P^{\downarrow}_{N''_b}$	0.418	0.108		0.197	0.075		-0.099	0.081	
$P^{\downarrow}_{N''_e}$	0.554	0.036	0.001	0.522	0.037	0.012	0.108	0.040	0.007
$P^{\downarrow}_{S''_t}$	-0.051	0.034		-0.454	0.032		-0.209	0.035	
$P^{\downarrow}_{S''_b}$	-0.029	0.108		-0.360	0.075		-0.138	0.081	
$P^{\downarrow}_{S''_e}$	-0.052	0.036	0.000	-0.467	0.037	0.004	-0.216	0.040	0.003
$P^{0}_{N''_t}$	0.373	0.068		0.379	0.056		0.411	0.067	
$P^{0}_{N''_b}$	0.328	0.202		0.028	0.127		0.120	0.166	
$P^{0}_{N''_e}$	0.376	0.074	0.001	0.421	0.064	0.021	0.439	0.076	0.009
$P^{0}_{S''_t}$	0.109	0.068		-0.017	0.056		-0.053	0.067	
$P^{0}_{S''_b}$	0.182	0.202		0.049	0.127		0.304	0.166	
$P^{0}_{S''_e}$	0.104	0.074	0.001	-0.024	0.064	0.004	-0.087	0.076	0.011

Table 32. 290 MeV 70° focal plane polarizations.

Mode	Normal			Sideways			Longitudinal		
Polar.	P	$\delta P_{(1)}$	$\delta P_{(2)}$	P	$\delta P_{(1)}$	$\delta P_{(2)}$	P	$\delta P_{(1)}$	$\delta P_{(2)}$
$P^{\uparrow}_{N''_t}$	-0.241	0.057		-0.078	0.049		0.271	0.056	
$P^{\uparrow}_{N''_b}$	-0.261	0.124		-0.081	0.101		0.265	0.107	
$P^{\uparrow}_{N''_e}$	-0.236	0.079	0.003	-0.078	0.064	0.000	0.273	0.077	0.000
$P^{\uparrow}_{S''_t}$	-0.095	0.057		0.204	0.049		0.182	0.056	
$P^{\uparrow}_{S''_b}$	-0.124	0.124		0.125	0.101		0.169	0.107	
$P^{\uparrow}_{S''_e}$	-0.088	0.079	0.004	0.222	0.064	0.007	0.186	0.077	0.001
$P^{\downarrow}_{N''_t}$	0.174	0.049		0.383	0.050		-0.008	0.057	
$P^{\downarrow}_{N''_b}$	0.010	0.121		0.247	0.097		-0.278	0.105	
$P^{\downarrow}_{N''_e}$	0.202	0.061	0.014	0.424	0.072	0.019	0.064	0.078	0.026
$P^{\downarrow}_{S''_t}$	-0.126	0.049		-0.141	0.050		-0.153	0.057	
$P^{\downarrow}_{S''_b}$	-0.113	0.121		-0.080	0.097		0.048	0.105	
$P^{\downarrow}_{S''_e}$	-0.128	0.061	0.001	-0.160	0.072	0.008	-0.207	0.078	0.020
$P^{0}_{N''_t}$	0.091	0.093		0.084	0.087		0.017	0.097	
$P^{0}_{N''_b}$	0.265	0.213		0.257	0.166		0.097	0.177	
$P^{0}_{N''_e}$	0.041	0.134	0.029	0.029	0.125	0.030	-0.006	0.134	0.014
$P^{0}_{S''_t}$	-0.240	0.093		0.029	0.087		0.062	0.097	
$P^{0}_{S''_b}$	-0.045	0.213		-0.319	0.166		-0.248	0.177	
$P^{0}_{S''_e}$	-0.295	0.134	0.033	0.138	0.125	0.060	0.149	0.134	0.052

Table 33. 290 MeV 80° focal plane polarizations.

Mode	Normal			Sideways			Longitudinal		
Polar.	P	$\delta P_{(1)}$	$\delta P_{(2)}$	P	$\delta P_{(1)}$	$\delta P_{(2)}$	P	$\delta P_{(1)}$	$\delta P_{(2)}$
$P^{\uparrow}_{N''_t}$	-0.305	0.081		-0.035	0.065		0.012	0.063	
$P^{\uparrow}_{N''_b}$	-0.160	0.176		-0.070	0.145		0.181	0.134	
$P^{\uparrow}_{N''_e}$	-0.340	0.109	0.012	-0.024	0.099	0.004	-0.024	0.082	0.011
$P^{\uparrow}_{S''_t}$	-0.198	0.081		0.053	0.065		0.195	0.063	
$P^{\uparrow}_{S''_b}$	-0.128	0.176		0.382	0.145		0.074	0.134	
$P^{\uparrow}_{S''_e}$	-0.215	0.109	0.006	-0.056	0.099	0.037	0.221	0.082	0.008
$P^{\downarrow}_{N''_t}$	0.220	0.079		0.112	0.067		-0.132	0.064	
$P^{\downarrow}_{N''_b}$	0.055	0.173		0.241	0.150		-0.137	0.132	
$P^{\downarrow}_{N''_e}$	0.257	0.105	0.013	0.070	0.101	0.013	-0.131	0.086	0.000
$P^{\downarrow}_{S''_t}$	0.099	0.079		0.133	0.067		-0.082	0.064	
$P^{\downarrow}_{S''_b}$	0.133	0.173		0.096	0.150		-0.173	0.132	
$P^{\downarrow}_{S''_e}$	0.091	0.105	0.003	0.145	0.101	0.004	-0.060	0.086	0.007
$P^{0}_{N''_t}$	0.052	0.146		0.037	0.118		0.069	0.110	
$P^{0}_{N''_b}$	-0.192	0.317		-0.247	0.260		-0.357	0.223	
$P^{0}_{N''_e}$	0.117	0.204	0.036	0.133	0.180	0.035	0.193	0.156	0.052
$P^{0}_{S''_t}$	0.336	0.146		-0.098	0.118		0.083	0.110	
$P^{0}_{S''_b}$	-0.086	0.317		-0.132	0.260		0.003	0.223	
$P^{0}_{S''_e}$	0.449	0.204	0.063	-0.087	0.180	0.004	0.106	0.156	0.010